

# Mediterranean intense desert dust outbreaks and their vertical structure based on remote sensing data

A. Gkikas<sup>1</sup>, S. Basart<sup>1</sup>, N. Hatzianastassiou<sup>2</sup>, E. Marinou<sup>3,9</sup>, V. Amiridis<sup>3</sup>, S. Kazadzis<sup>4,5</sup>, J. Pey<sup>6</sup>, X. Querol<sup>7</sup>, O. Jorba<sup>1</sup>, S. Gassó<sup>8</sup> and J.M. Baldasano<sup>1,8</sup>

<sup>1</sup>Earth Sciences Department, Barcelona Supercomputing Center, Barcelona, Spain

<sup>2</sup>Laboratory of Meteorology, Department of Physics, University of Ioannina, Ioannina, Greece

<sup>3</sup>Institute for Astronomy, Astrophysics, Space Applications and Remote Sensing, National Observatory of Athens, Athens, 15236, Greece

<sup>4</sup>Physikalisch-Meteorologisches Observatorium Davos, World Radiation Center, Switzerland

<sup>5</sup>Institute of Environmental Research and Sustainable Development, National Observatory of Athens, Athens, Greece

<sup>6</sup>Spanish Geological Survey. Zaragoza IGME Unit, Zaragoza, Spain

<sup>7</sup>Institute of Environmental Assessment and Water Research, IDÆA-CSIC C/Jordi Girona, 18–26, 08034 Barcelona, Spain

<sup>8</sup>Environmental Modelling Laboratory, Technical University of Catalonia, Barcelona, Spain

<sup>9</sup>Laboratory of Atmospheric Physics, Department of Physics, Aristotle University of Thessaloniki, Thessaloniki, Greece

Corresponding author: Antonis Gkikas ([antonis.gkikas@bsc.es](mailto:antonis.gkikas@bsc.es))

## Abstract

The main aim of the present study is to describe the vertical structure of the intense Mediterranean dust outbreaks, based on the use of satellite and surface-based retrievals/measurements. Strong and extreme desert dust (DD) episodes are identified at  $1^\circ \times 1^\circ$  spatial resolution, over the period Mar. 2000 – Feb. 2013, through the implementation of an updated objective and dynamic algorithm. According to the algorithm, strong DD episodes occurring at a specific place correspond to cases in which the daily aerosol optical depth at 550nm ( $AOD_{550nm}$ ) exceeds or equals the long-term mean  $AOD_{550nm}$  (Mean) plus two standard deviations (Std) value being smaller than  $Mean+4*Std$ . Extreme DD episodes correspond to cases in which the daily  $AOD_{550nm}$  value equals or exceeds  $Mean+4*Std$ . For the identification of DD episodes additional optical properties (Ångström exponent, fine fraction, effective radius and Aerosol Index) derived by the MODIS-Terra & Aqua (also AOD retrievals), OMI-Aura and EP-TOMS databases are used as inputs. According to the algorithm using MODIS-Terra data, over the period Mar. 2000 – Feb. 2013, strong DD episodes occur more frequently (up to 9.9 episodes  $yr^{-1}$ ) over

34 the western Mediterranean while the corresponding frequencies for the extreme ones are smaller (up to  
35 3.3 episodes yr<sup>-1</sup>, central Mediterranean Sea). In contrast to their frequency, dust episodes are more  
36 intense (AODs up to 4.1), over the central and eastern Mediterranean Sea, off the northern African  
37 coasts. Slightly lower frequencies and higher intensities are found when the satellite algorithm operates  
38 based on MODIS-Aqua retrievals, for the period 2003–2012. The consistence of the algorithm is  
39 successfully tested through the application of an alternative methodology for the determination of DD  
40 episodes, which produced similar features of the episodes' frequency and intensity, with just slightly  
41 higher frequencies and lower intensities. The performance of the satellite algorithm is assessed against  
42 surface-based daily data from 109 sun-photometric (AERONET) and 22 PM<sub>10</sub> stations. The agreement  
43 between AERONET and MODIS *AOD* is satisfactory ( $R=0.505-0.750$ ) improving considerably when  
44 MODIS level 3 retrievals with higher sub-grid spatial representativeness and homogeneity are  
45 considered. The CALIOP vertical profiles of pure and polluted dust observations and the associated  
46 total backscatter coefficient at 532 nm ( $\beta_{532nm}$ ), indicate that dust particles are mainly detected between  
47 0.5 and 6 km, though they can reach 8 km between the parallels 32° N and 38° N in warm seasons,  
48 while an increased number of CALIOP dust records at higher altitudes is observed with increased  
49 latitude, northwards to 40° N, revealing an ascending mode of the dust transport. However, the overall  
50 intensity of DD episodes is maximum (up to 0.006 km<sup>-1</sup> sr<sup>-1</sup>) below 2 km and at the southern parts of  
51 the study region (30° N - 34° N). Additionally, the average thickness of dust layers gradually decreases  
52 from 4 to 2 km moving from south to north. In spring, dust layers of moderate-to-high  $\beta_{532nm}$  values (~  
53 0.004 km<sup>-1</sup> sr<sup>-1</sup>) are detected over the Mediterranean (35° N - 42° N), extending from 2 to 4 km. Over  
54 the western Mediterranean, dust layers are observed between 2 and 6 km, while their base height is  
55 decreased down to 0.5 km for increasing longitudes underlying the role of topography and thermal  
56 convection. The vertical profiles of CALIOP  $\beta_{532nm}$  confirm the multilayered structure of the  
57 Mediterranean desert dust outbreaks on both annual and seasonal basis, with several dust layers of  
58 variable geometrical characteristics and intensities. A detailed analysis of the vertical structure of  
59 specific DD episodes using CALIOP profiles reveals that consideration of the dust vertical structure is  
60 necessary when attempting comparisons between columnar MODIS AOD retrievals and ground PM<sub>10</sub>  
61 concentrations.

## 62 1. Introduction

63 The Mediterranean basin, due to its proximity to the major dust source arid areas of Northern  
64 Africa and Middle East (Middleton and Goudie, 2001; Prospero et al., 2002; Ginoux et al., 2012) is  
65 frequently affected by transported high dust loads referred to as episodes or events. The suspension and

66 accumulation of mineral particles into the atmosphere over the Saharan and Arabian Peninsula's  
67 deserts are determined by various factors such as the enhanced turbulence, soil conditions (reduced  
68 vegetation cover and soil moisture), reduced precipitation amounts, latitudinal shift of the Intertropical  
69 Convergence Zone (ITCZ) as well as by small scale meteorological processes (e.g. haboobs). However,  
70 dust particles can be transported far away from their sources, mainly towards the Atlantic Ocean (e.g.  
71 Prospero and Lamb, 2003; Ben-Ami et al., 2010; Huang et al., 2010) and Europe (e.g. Mona et al.,  
72 2006; Mona et al., 2012; Papayannis et al., 2008; Basart et al., 2012; Bègue et al., 2012; Pey et al.,  
73 2013), favored by the prevailing atmospheric circulation patterns, from planetary to synoptic scales.  
74 Due to their frequent transport in the Mediterranean, mineral dust particles, constitute the predominant  
75 aerosol type there (Barnaba and Gobbi, 2004; Basart et al., 2012), as shown by the good agreement, in  
76 spatial terms, between the geographical distributions of dust episodes' *AOD* (Gkikas et al., 2013) and  
77 average *AOD* conditions (Papadimas et al., 2008).

78 Dust particles play an important role for the shortwave (SW) and longwave (LW) radiation budget  
79 (e.g. Kaufman et al., 2002; Tegen et al., 2003; Heinold et al., 2008) and climate (IPCC, 2013). They  
80 affect atmospheric heating/cooling rates (e.g. Mallet et al., 2009) while they can also result in a  
81 modification of atmospheric dynamics and large atmospheric circulations like monsoons (e.g. Lau et  
82 al., 2006; Bollasina et al., 2011), cloud properties and precipitation (e.g. Huang et al., 2006; Solmon et  
83 al., 2008). Moreover, it has been shown that the consideration of their radiative impacts in numerical  
84 simulations can improve the forecasting accuracy of weather models (Pérez et al., 2006). Dust particles  
85 also affect air quality in urban areas (Basart et al., 2012) causing adverse health effects (Díaz et al.,  
86 2012; Karanasiou et al., 2012; Pérez García-Pando et al., 2014). All these consequences of dust aerosol  
87 are relevant and maximize under maximum dust loads, namely dust episodes, highlighting thus the  
88 significance of analyzing the spatial and temporal characteristics of such events. To this aim, many  
89 studies have been carried out using either surface (e.g. Cachorro et al., 2006) or satellite (e.g. Moulin et  
90 al., 1998) observations, as well as modelling techniques (e.g. Heinold et al., 2007) focusing on the  
91 broader Mediterranean area. These studies have been done either for specific cases (e.g. Kubilay et al.,  
92 2003; Balis et al., 2006) or for extended periods at specific locations (e.g. Meloni et al., 2007; Toledano  
93 et al., 2007a; Gobbi et al., 2013; Mona et al., 2014). Recently, Gkikas et al. (2013) developed an  
94 objective and dynamic algorithm relying on satellite retrievals, which enabled an overall view of dust  
95 episodes over the entire Mediterranean and the characterization of their regime.

96 Extensive research has been also carried out on the mechanisms of Mediterranean dust outbreaks.  
97 Therefore, several mechanisms and processes of transport, apart from dust emissions in source areas,

98 have been proposed as controlling factors. Moulin et al. (1997) showed that the exported dust loads  
99 from Northern Africa towards the Atlantic Ocean and the Mediterranean are controlled by the phase of  
100 the North Atlantic Oscillation (NAO). Other studies, focused on the description of atmospheric  
101 circulation characteristics favoring the occurrence of desert dust outbreaks over the central (Barkan et  
102 al., 2005; Meloni et al., 2008) or western (Querol et al., 1998; Rodriguez et al., 2001; Salvador et al.,  
103 2014) Mediterranean, but on a synoptic scale. An objective classification, based on multivariate  
104 statistical methods, of the atmospheric circulation patterns related to dust intrusions over the  
105 Mediterranean, has been presented by Gkikas et al. (2015) and Varga et al. (2014).

106 The concentration of dust aerosols in the Mediterranean is characterized by strong spatial and  
107 temporal variability, associated with the seasonal variability of cyclones dominating or affecting the  
108 broader Mediterranean basin (Trigo et al., 2002). According to Moulin et al. (1998), dust AOD levels  
109 are higher in spring and summer compared to the wet seasons of the year. Moreover, dust intrusions are  
110 mainly recorded over the southeastern Mediterranean in spring and winter, over the western parts in  
111 summer and over the central ones in autumn (Gkikas et al., 2013).

112 Dust transport over the Mediterranean is characterized by a multi-layered structure (Hamonou et  
113 al., 1999; Papayannis et al., 2008) in contrast to the Atlantic Ocean, which is well confined to the  
114 Saharan Air Layer (SAL, Karyampudi et al., 1999). The vertical distribution of dust load into the  
115 troposphere as well as the profile of dust aerosols' optical properties at different altitudes, control the  
116 impacts on atmospheric dynamics induced by the mineral particles (Zhang et al., 2013). In order to  
117 describe the geometrical features of dust transport, many researchers have used ground lidar  
118 measurements, model simulations (Alpert et al., 2004; Kishcha et al. 2005) or they have relied on a  
119 synergistic use of satellite observations and ground lidar profiles (Berthier et al., 2006). The vertical  
120 extension of the Saharan dust intrusions over Europe, during the period 2000-2002, was the subject of a  
121 comprehensive study by Papayannis et al. (2008), who used lidar measurements from the EARLINET  
122 (European Aerosol Research Lidar Network, Bösenberg et al., 2003). Over the Mediterranean stations,  
123 the mean base, top and thickness of dust layers was found to vary from 1356 to 2980 m, 3600 to 5900  
124 m and 726 to 3340 m, respectively. According to the obtained results, tracers of dust particles can be  
125 detected up to 10 km, as also reported by Gobbi et al. (2000), who studied a Saharan dust event in  
126 Crete (south Greece) during spring of 1999.

127 Several similar studies have been also performed for specific Mediterranean locations based on  
128 EARLINET lidar measurements. For example, Mona et al. (2006) analyzed the vertical structure of 112

129 Saharan intrusions that occurred over Potenza (Italy), from May 2000 to April 2003. The authors found  
130 that these outbreaks are confined between 1.8 and 9 km while their mass center is located at 3.5 km  
131 above sea level (a.s.l.). A similar analysis for Athens and Thessaloniki over the period 2000-2002, was  
132 conducted by Papayannis et al. (2005) who demonstrated that dust layers are recorded mainly between  
133 2 and 5 km while their thicknesses vary from 0.2 to 3 km. The geometrical characteristics of dust layers  
134 over Athens, during the period 2004 – 2006, have been also presented by Papayannis et al. (2009), who  
135 pointed out that the center of mass of dust layers is located at 2.9 km being in a very good agreement  
136 with Kalivitis et al. (2007) findings (around 3 km) for the eastern Mediterranean. Additionally, the  
137 authors reported that the dust layers mainly extend from 1.6 to 5.8 km while mineral particles can be  
138 detected, at very low concentrations, up to 8 km a.s.l.. Gobbi et al. (2013) found that dust plumes, over  
139 Rome, mainly extend from 0 to 6 km while their center of mass is located at around 3 km. In the  
140 southern parts of Italy (Potenza), dust layers' base is found between 2 and 3 km, their geometrical  
141 height extends from 2.5 to 4 km while tracers of dust particles can be detected up to 10 km, based on a  
142 dataset of 310 dust events analyzed by Mona et al. (2014). Finally, Pisani et al. (2011) stated that the  
143 mean base and top of dust layers is found at 1.5 km and 4.6 km a.s.l., respectively, while their mean  
144 thickness is equal to 3.1 km, based on a statistical analysis of 45 desert dust episodes observed over  
145 Naples (Italy), from May 2000 to August 2003.

146 Surface-based lidar measurements like those used in the aforementioned studies provide useful  
147 information about the geometrical and optical properties of dust layers, but they are representative only  
148 for specific locations. Yet, a more complete knowledge about the vertical structure of dust outbreaks is  
149 necessary in order to adequately understand and determine their possible effects. The limitation  
150 imposed by the use of surface-based lidar observations can be overcome by utilizing accurate satellite  
151 retrievals, as a complementary tool, which provide extended spatial coverage. Since 2006, vertical  
152 resolved observations of aerosols and clouds from space were made possible thanks to the CALIOP  
153 (Cloud-Aerosol Lidar with Orthogonal Polarization) lidar flying onboard the CALIPSO (Cloud-  
154 Aerosol Lidar and Infrared Pathfinder Satellite Observations) satellite (Winker et al., 2009). Based on  
155 CALIOP observations, Liu et al. (2008) analyzed the global vertical distribution of aerosols for one  
156 year, while other studies focused on the vertical structure of dust outflows towards the Atlantic Ocean  
157 (e.g. Ben-Ami et al., 2009; Adams et al., 2012; Tsamalis et al., 2013) and the Pacific Ocean (e.g.  
158 Eguchi et al., 2009; Hara et al., 2009). On the contrary, over the broader Mediterranean area, only a  
159 small number of studies has been made aiming at describing the vertical distribution of dust aerosols  
160 (Amiridis et al., 2013) or specifying the vertical structure of dust events (Amiridis et al., 2009).

161 Nevertheless, they only dealt with a single dust event (18-23 May 2008, Amiridis et al., 2009) and thus  
162 cannot satisfy the need to know the general vertical structure of Mediterranean dust episodes.

163 The main target of the present study is to describe the Mediterranean desert dust outbreaks' vertical  
164 structure. For this purpose, satellite retrievals derived by the MODIS-Terra/Aqua, Earth Probe-TOMS,  
165 OMI-Aura and CALIOP-CALIPSO databases (Section 2) are used in a synergistic way. The dust  
166 outbreaks are identified with an objective and dynamic algorithm, which uses appropriate aerosol  
167 optical properties representative of suspended particles' load, size and nature (Section 3). Based on its  
168 outputs, the primary characteristics of the intense Mediterranean desert dust (DD) episodes, namely  
169 their frequency and intensity, are described in Section 4.1. Just in order to assess the consistency of the  
170 algorithm' concept, an alternative methodology for the determination of DD episodes is also applied  
171 and the obtained results are inter-compared with the basic methodology. The outputs of the default  
172 version of the satellite algorithm are compared versus surface measurements provided by AERONET  
173 or PM<sub>10</sub> stations, located within the study region (Section 4.2). Additionally, useful information about  
174 various optical and physical properties under intense dust episodes conditions is also derived from the  
175 aforementioned analysis. For the identified DD episodes, collocated CALIOP-CALIPSO vertical  
176 feature mask and total backscatter coefficient at 532 nm retrievals are used in order to describe the  
177 annual and seasonal variability of dust outbreaks' vertical extension over the Mediterranean (Section  
178 4.3). Moreover, in Section 4.4, a thorough analysis of few specific Mediterranean DD episodes is  
179 made, in order to examine how the vertical distribution of desert dust outbreaks can affect the  
180 agreement between MODIS AOD and PM<sub>10</sub> data. Finally, the summary and conclusions are drawn in  
181 Section 5.

182

## 183 **2. Satellite and surface-based data**

184 The different types of satellite retrievals that have been used as inputs to the objective and dynamic  
185 satellite algorithm are described below, namely the MODIS (Section 2.1.1), EP-TOMS and OMI-Aura  
186 (Section 2.1.2) databases. Also, CALIOP-CALIPSO vertically resolved satellite data, coincident with  
187 the identified desert dust outbreaks by the satellite algorithm, are described in Section 2.1.3. Finally,  
188 surface-based sun-photometric AERONET retrievals and PM<sub>10</sub> concentrations, both used for the  
189 comparison against the satellite algorithm's outputs, are described in Sections 2.2.1 and 2.2.2,  
190 respectively.

191

## 192 2.1 Satellite data

### 193 2.1.1 MODIS

194

195 MODERate resolution Imaging Spectroradiometer (MODIS) onboard the Terra and Aqua satellites –  
196 with daytime local equator crossing time at 10:30 and 13:30 UTC, respectively, and 2330 km viewing  
197 swath – acquires measurements at 36 spectral bands between 0.415 and 14.235  $\mu\text{m}$  with varying spatial  
198 resolution of 250, 500 and 1000 m. Observations from Terra and Aqua are made continuously since  
199 February 2000 and July 2002, respectively, and are available from the LAADS website  
200 (<ftp://ladsweb.nascom.nasa.gov/>). Aerosol optical properties are retrieved through the Dark Target  
201 (DT) algorithm (see e.g. Kaufman et al., 1997, 2001; Tanré et al., 1997; Levy et al., 2003; Remer et al.,  
202 2005) where different assumptions are considered depending on the underlying surface type (land or  
203 ocean). Several evaluation studies (e.g. Remer et al., 2008; Papadimas et al., 2009; Levy et al., 2010;  
204 Nabat et al., 2013) have shown that aerosol optical depth (*AOD*) can be retrieved satisfactorily by  
205 MODIS, nevertheless its performance is better over sea (uncertainty equal to  $\pm 0.03 \pm 0.05 \times AOD$ ,  
206 Remer et al., 2002) than over land ( $\pm 0.05 \pm 0.15 \times AOD$ , Levy et al., 2010).

207 The following daily MODIS-Terra and MODIS-Aqua Collection 051 (C051) level 3 satellite data  
208 (MOD08\_D3 and MYD08\_D3 files) provided at  $1^\circ \times 1^\circ$  latitude-longitude spatial resolution are used:  
209 (i)  $AOD_{550nm}$ , (ii) Ångström exponent over land ( $\alpha_{470-660nm}$ ), (iii) Ångström exponent over ocean  
210 ( $\alpha_{550-865nm}$ ), (iv) fine-mode fraction (*FF*) of *AOD* over land and ocean and (v) Effective radius over  
211 ocean ( $r_{eff}$ ). It must be mentioned that the size parameters ( $\alpha$ , *FF*) over land are less reliable compared  
212 to the corresponding ones over sea, since they are highly sensitive to spectral dependent factors such as  
213 errors in the surface model or sensor calibration changes. Over sea, the accuracy of size parameters is  
214 strongly dependent on wind conditions. Similar data have been used by Gkikas et al. (2013), however,  
215 in the present study we have improved data quality by using the quality assurance-weighted (QA) level  
216 3 data ([http://modis-atmos.gsfc.nasa.gov/docs/QA\\_Plan\\_2007\\_04\\_12.pdf](http://modis-atmos.gsfc.nasa.gov/docs/QA_Plan_2007_04_12.pdf)) derived from the level 2  
217 retrievals (10 km x 10 km spatial resolution). Each level 2 retrieval, is flagged with a bit value (from 0  
218 to 3) corresponding to confidence levels (No confidence: 0, Marginal: 1, Good: 2 and Very Good: 3).  
219 Based on this, the level 3 QA-weighted spatial means are obtained by the corresponding level 2  
220 retrievals considering as weight their confidence level (bit value). In addition, the day cloud fraction as  
221 well as the number of level 2 counts, which are both relevant to the performance of the satellite

222 algorithm, are also used in this study. The time series of daily MODIS aerosol data cover the 13-yr  
223 period March 2000-February 2013 (Terra) and the 10-yr period January 2003-December 2012 (Aqua).

#### 224 2.1.2 EP/TOMS and OMI-Aura

225 The selected retrievals from MODIS provide information about particles' load (*AOD*) and size ( $\alpha$ ,  
226  $FF$ ,  $r_{eff}$ ), which are both necessary to identify dust episodes. However, since dust is not the only coarse  
227 aerosol, for example sea-salt can be so as well, another optical property indicative of particle  
228 absorption efficiency is also required by the algorithm. To address this issue, the Absorption Aerosol  
229 Index (*AI*) daily data were also used, derived from measurements taken by the Total Ozone Mapping  
230 Spectrometer (TOMS) instrument onboard the NASA's Earth-Probe satellite (2000-2004) and the  
231 Ozone Monitoring Instrument (OMI) onboard the NASA's Aura satellite (2005-2013). *AI* is the  
232 primary TOMS aerosol product (Herman et al., 1997) based on a spectral contrast method in a UV  
233 region (331-360 nm) where ozone absorption is very small and can be used for the distinction between  
234 scattering (e.g. sea-salt) and absorbing (e.g. desert dust, smoke) aerosols. The retrieval algorithm (fully  
235 described by Torres et al., 1998; 2002; 2005) takes advantage of the low surface albedo in the UV  
236 spectrum range, even in arid and semi-arid areas, making thus possible the estimation of the *AOD* over  
237 highly reflecting desert surfaces, where the major dust sources are located. Since the late 70's, the  
238 TOMS sensor onboard Nimbus-7 (1978 – 1993) and Earth Probe (1996 – 2005) has been providing  
239 global aerosol measurements. With the deployment of the EOS-Aura OMI (Ozone Monitoring  
240 Instrument) in mid-2004 (Torres et al., 2007) the near UV aerosol record continues to be extended into  
241 the foreseeable future. OMI is a hyperspectral sensor, covering the 270-500 nm range, launched  
242 onboard the EOS-Aura satellite on July 15, 2004 (1:38 pm equator crossing time, ascending mode)  
243 providing almost daily global coverage thanks to its wide viewing swath (2600 km with 13 km x 24 km  
244 nadir resolution). Apart from *AI* measurements, OMI aerosol products include also the total and  
245 absorption *AOD* and the single scattering albedo at 388 and 500 nm (Torres et al., 2007). Both EP-  
246 TOMS and OMI-Aura retrievals are available via the Mirador ftp server (<http://mirador.gsfc.nasa.gov/>)  
247 of the Goddard Earth Sciences Data and Information Services Center (GES DISC). OMI-Aura data, as  
248 MODIS, are provided at 1° x 1° spatial resolution while the EP-TOMS retrievals have been regridded  
249 from their raw spatial resolution (1° x 1.25°) in order to match with the other two datasets (OMI,  
250 MODIS).

251

### 252 2.1.3 CALIOP-CALIPSO

253

254 The Cloud-Aerosol Lidar with Orthogonal Polarization (CALIOP) onboard the NASA's satellite  
255 CALIPSO (Cloud-Aerosol Lidar and Infrared Pathfinder Satellite Observations), launched in April  
256 2006, provides vertical resolved aerosol and cloud observations (Winker et al., 2009) since June 2006.  
257 CALIPSO is flying in the A-Train constellation (Stephens et al., 2002; <http://atrain.nasa.gov/>) in a sun-  
258 synchronous polar orbit at 705 km over the surface, with a 16-day repeat cycle, crossing the equatorial  
259 plane at about 13:30 local solar time (Winker et al., 2009). CALIOP is an active sensor measuring the  
260 backscatter signal at 532 nm and 1064 nm as well as the polarization at 532 nm (Winker et al., 2009).  
261 These level 1 retrievals are further processed (calibration and range corrections) passing to Level 2 in  
262 order to retrieve the backscatter and extinction coefficients, at 532 nm and 1064 nm, for aerosol and  
263 cloud layers. The identification of cloud and aerosol layers within the atmosphere (Vaughan et al.,  
264 2009) is made through the cloud aerosol discrimination (CAD) algorithm (Liu et al., 2009), which is  
265 based on the probability distribution functions (PDFs) of altitude-and-latitude-dependent parameters  
266 (integrated color ratio, layer-integrated volume depolarization ratio, mean attenuated backscatter  
267 coefficient). CAD scores vary mainly from -100 to 100 indicating the presence of aerosols and clouds  
268 when are negative and positive, respectively, while bins of confidence levels, both for aerosols and  
269 clouds, are defined based on their absolute values  
270 ([https://eosweb.larc.nasa.gov/sites/default/files/project/calipso/quality\\_summaries/CALIOP\\_L2VFMPr  
272 oducts\\_3.01.pdf](https://eosweb.larc.nasa.gov/sites/default/files/project/calipso/quality_summaries/CALIOP_L2VFMPr<br/>271 oducts_3.01.pdf)). More specifically, the performance of the classification scheme in the VFM  
273 algorithm, either for aerosols or clouds, is more reliable for increasing CAD scores in absolute terms.  
274 Aerosols are categorized in 6 primary types namely: (i) clean marine, (ii) dust, (iii) polluted  
275 continental, (iv) clean continental, (v) polluted dust and (vi) smoke (Omar et al., 2009).

275 In the present analysis, we use the Version 3 (3.01 and 3.02) of the Level 2 Vertical Feature Mask  
276 (VFM) and Aerosol Profile Products (APro) files, available from June 2006 to February 2013, both  
277 derived from the NASA's Earth Observing System Data and Information System  
278 (<http://reverb.echo.nasa.gov/>). The aerosol profile products are generated at a uniform horizontal  
279 resolution of 5 km ([http://www-calipso.larc.nasa.gov/products/CALIPSO\\_DPC\\_Rev3x6.pdf](http://www-calipso.larc.nasa.gov/products/CALIPSO_DPC_Rev3x6.pdf)), while the  
280 vertical resolution varies from 60 to 180 m depending on the altitude range and the parameter. The  
281 scientific data sets which have been analyzed are the following: (i) aerosol subtype, (ii) CAD score and

282 (iii) Total Backscatter Coefficient at 532 nm ( $\beta_{532nm}$ ), reported at several tropospheric and stratospheric  
283 levels above mean sea level (Hunt et al., 2009).

284

## 285 2.2 Surface-based data

286

### 287 2.2.1 AERONET

288 The AErosol RObotic NETwork (AERONET, Holben et al., 1998) is a worldwide network of  
289 installed CIMEL sun-sky radiometers obtaining sun-photometric observations in more than 1000  
290 locations of the planet (<http://aeronet.gsfc.nasa.gov>). The solar irradiances received by the photometer  
291 are inverted to columnar aerosol optical and microphysical properties through the implementation of  
292 retrieval algorithms (e.g. Dubovik and King, 2000; O' Neill et al., 2003). The followed standardized  
293 methods concerning instrument maintenance, calibration, cloud screening and data processing allow  
294 aerosol monitoring and comparison between different study periods and areas (Smirnov et al., 2000).  
295 From the global AERONET stations, 109 are located within the geographical limits of our study  
296 region. For each station, the daily averages of cloud-screened and quality assured data (Level 2.0) of  
297 direct sun and almucantar retrievals are used for: (i) *AOD* at 7 wavelengths from 340 to 1020 nm, (ii)  
298 size distribution retrieved for 22 logarithmically equidistant discrete points ( $r_i$ ) in the range of sizes  
299  $0.05 \mu\text{m} \leq r \leq 15 \mu\text{m}$ , (iii) Ångström exponent between 440 and 870 nm ( $\alpha_{440-870nm}$ ), (iv) total effective  
300 radius ( $r_{eff}$ ), and (v) single scattering albedo (*SSA*) and asymmetry parameter ( $g_{aer}$ ) both retrieved at 440  
301 nm, 675 nm, 870 nm and 1020 nm. The uncertainty in the estimation of *AOD* depends on technical  
302 (e.g. calibration method) factors and inversion assumptions, both described in detail in Holben et al.  
303 (1998). Moreover, the accuracy of the retrieved *AOD* by the CIMEL radiometer is spectrally  
304 dependent, being higher ( $<\pm 0.01$ ) for wavelengths longer than 440 nm and lower ( $<\pm 0.02$ ) for the UV  
305 wavelengths (Eck et al., 1999). It should be also noted that the AERONET Level 2.0 inversion products  
306 (e.g. *SSA*) are provided when *AOD* at 440 nm is higher than 0.4 ensuring the minimization of the  
307 inversion uncertainties, which are also determined by other factors (e.g. scattering angle, particles'  
308 sphericity) as stated in detail by Dubovik et al. (2000).

309

### 310 2.2.2 $PM_{10}$

311 Daily total and dust surface  $PM_{10}$  concentrations, over the period 2001-2011 from 22 regional  
312 background and suburban background sites were used in this study. The monitoring sites are distributed

313 as follows: 10 in Spain; 2 in southern France; 5 in Italy; 3 in Greece; 1 in southern Bulgaria and 1 in  
314 Cyprus. PM<sub>10</sub> concentrations were obtained in most cases from gravimetric determinations on filters,  
315 whereas in few cases they were determined by real time instruments (Querol et al., 2009b; Pey et al.,  
316 2013) but corrected against gravimetric measurements carried out in annual field campaigns. The  
317 disaggregation of the dust component to the total amount is made based on a statistical approach which  
318 has been applied in several past studies (e.g. Rodríguez et al., 2001; Escudero et al., 2007; Querol et al.,  
319 2009b; Pey et al., 2013). A full description of the methodology which is followed for the calculation of  
320 dust particles' contribution to the total PM<sub>10</sub> is presented in Escudero et al. (2007). Briefly, the net dust  
321 PM<sub>10</sub> amount is calculated through the subtraction of the regional background PM<sub>10</sub>, which is obtained  
322 by applying a monthly moving 30<sup>th</sup> percentile to the PM<sub>10</sub> timeseries excluding days of dust transport,  
323 from the corresponding values of the total PM<sub>10</sub> concentrations. Most of the derived data were obtained  
324 from the AirBase (<http://acm.eionet.europa.eu/databases/airbase/>) database, while for the stations  
325 Finokalia (Crete) and Montseny (NE Spain) the relevant measurements have been acquired from the  
326 EUSAAR (<http://www.eusaar.net/>) database.

327

### 328 **3. Identification of desert dust episodes**

329

330 Following the methodology proposed by Gkikas et al. (2013), desert dust (DD) episodes are  
331 identified based on an objective and dynamic algorithm, which is depicted in the flowchart of Figure 1.  
332 The algorithm operates in three steps and is applied in each individual 1° x 1° geographical cell within  
333 the geographical limits of the study domain (29° N - 47° N and 11° W - 39° E). First (Fig. 1, yellow  
334 box), the mean (*Mean*) and the associated standard deviation (*Std*) from the available *AOD*<sub>550nm</sub>  
335 retrievals are calculated for the whole study period. These primary statistics are used for the definition  
336 of two threshold levels, which are equal to  $Mean+2*Std$  and  $Mean+4*Std$ . At the next step, the  
337 algorithm analyzes the daily *AOD*<sub>550nm</sub> timeseries and classifies an episode as a strong one when *AOD*  
338 is between the two defined thresholds ( $Mean+2*Std \leq AOD_{550nm} < Mean+4*Std$ ) and as an extreme  
339 one when *AOD* is higher/equal than  $Mean+4*Std$  (cyan boxes). The same approach was undertaken by  
340 Gkikas et al. (2009) who classified the Mediterranean aerosol episodes over the period 2000-2007  
341 according to their strength and described their frequency and intensity. It must be clarified that  
342 according to our methodology in areas frequently affected by dust episodes, both mean and standard  
343 deviation values are expected to be high resulting to high thresholds which means that cases with  
344 moderate-to-high *AOD*s, also possibly relevant to radiative and health effects, are masked out from the

345 dataset. In order to investigate the possible impact of this, “unbiased” mean, standard deviation and  
346 thresholds of AOD are also computed based on another methodology and the results are discussed  
347 comparatively to those of the primary methodology in a separate paragraph. Moreover, it must be  
348 mentioned that the satellite algorithm identifies only intense desert dust episodes since their *AOD* must  
349 be higher than  $Mean+2*Std$  which is considered as a high threshold level.

350 It should be noted that the representativeness of the calculated mean levels is possibly affected by  
351 the availability of the AOD retrievals and particularly by the way these data are distributed at different  
352 temporal scales. To this aim, we have calculated the percentage availability of AOD retrievals on a  
353 monthly, seasonal and year by year basis, over the period 2000-2013 (results not shown here). Seasonal  
354 differences of AOD availability are mainly encountered in the northern parts of the study region, with  
355 lower values (20 to 40 %) from December to February against 50-85% for the rest of the year. This is  
356 attributed to the enhanced cloud coverage prohibiting the satellite observations. Nevertheless, this does  
357 not essentially affect the algorithm outputs since these regions, being far away from the dust sources,  
358 are not so frequently affected by dust outbreaks, especially given the significant wet removal of  
359 aerosols during this most rainy season of the year. On a year by year basis, the differences of the AOD  
360 data’s availability are almost negligible.

361 In a further step of the methodology, the strong and extreme DD episodes are identified separately  
362 over land and sea surfaces of the study region. This is achieved through the usage of specific aerosol  
363 optical properties, namely the Ångström exponent, effective radius, fine fraction and aerosol index,  
364 which provide information about particles’ size and nature (black box, Figure 1). For each optical  
365 property, appropriate upper or lower thresholds have been set up (green boxes, Figure 1) which must be  
366 valid concurrently in order to certify the presence of dust particles in the atmosphere. These cut-off  
367 levels have been selected according to the literature findings, availability of raw data and several  
368 sensitivity tests (more details are provided in Gkikas et al., 2013). The validity of these thresholds is  
369 further evaluated against AERONET measurements and the corresponding results are discussed in  
370 Section 4.2.1.4.

371 In order to address the issue of possible overestimation of the defined threshold levels, particularly  
372 in the most dust affected areas as it has been mentioned above, we have also applied the satellite  
373 algorithm using an alternative methodology (METHOD-B) in which dust-affected grid cells were  
374 excluded. In this case, from the raw AOD retrievals we have masked out the “pure” desert dust grid  
375 cells, which were identified based on the concurrent fulfillment of the defined criteria for dust  
376 occurrence in the algorithm (for Ångström exponent, fine fraction, aerosol index and effective radius,

377 green boxes of Figure 1). Then, from the remaining data (non-dust AOD retrievals), the mean, the  
378 associated standard deviation as well as the defined thresholds of AOD are computed for the whole  
379 study period, for each pixel, as also done in the primary methodology. Finally, also similarly to the way  
380 done in the primary methodology, the DD episodes were classified into strong and extreme ones. The  
381 frequency of occurrence and intensity of DD episodes determined with METHOD-B are provided in  
382 the supplementary material (Figures S1 and S2) while their differences with regards to the primary  
383 methodology are discussed in Section 4.1.

384 As explained, a similar methodology and data were used in the study by Gkikas et al. (2013).  
385 Nevertheless, the present one is a significant extension mainly for five reasons: (i) DD episodes are  
386 identified here over an extended period of study and for both MODIS platforms, i.e. Mar. 2000 – Feb.  
387 2013 for MODIS-Terra and 2003-2012 for MODIS-Aqua, (ii) a second methodology (METHOD-B)  
388 for the identification of DD episodes is tested, (iii) the quality of the input data is improved by using  
389 QA-weighted level-3 data produced by weighting level-2 data based on their confidence flag instead of  
390 regular ones ( $QA \geq 1$ ), (iv) emphasis is given to the vertical structure of the intense DD episodes and (v)  
391 the role of the detailed dust outbreaks' vertical structure for the level of agreement between columnar  
392 MODIS AOD and ground  $PM_{10}$  concentrations is investigated. Moreover, an improvement of the  
393 methodology consists in the application of our satellite algorithm also using only *AODs* associated with  
394 cloud fractions (*CF*) lower/equal than 0.8, in order to investigate possible modifications of our results  
395 due to the cloud contamination effects on MODIS *AODs*. The critical value of 0.8 for *CF* has been  
396 defined according to Zhang et al. (2005) and Remer et al. (2008), who stated that under extended cloud  
397 coverage conditions *AOD* levels can be increased substantially.

398

399

#### 400 **4. Results**

401 Before dealing with the vertical structure of dust outbreaks (sub-sections 4.3 and 4.4), it is very  
402 important to describe their horizontal patterns (sub-section 4.1) and also to compare the algorithm's  
403 outputs against quality AERONET and  $PM_{10}$  observations (sub-section 4.2) in order to ensure an  
404 accurate three-dimensional view of the intense Mediterranean DD episodes. It must be clarified, that  
405 the comparison of the satellite algorithm's outputs versus AERONET/ $PM_{10}$  is made only for its default  
406 version and not for the METHOD-B, since between the two methodologies are not found remarkable  
407 differences, as it will be presented in Section 4.1. Accordingly, the synergistic implementation of the  
408 CALIOP-CALIPSO lidar profiles is done only when the DD episodes are identified based on the

409 primary methodology. The present section has been organized accordingly and the results are given  
410 below.

411

#### 412 4.1 2D geographical distributions of desert dust episodes' frequency and intensity

413 The mean geographical distributions of strong and extreme DD episodes' frequency of occurrence  
414 (episodes  $\text{yr}^{-1}$ ) are presented in Figure 2. Results are given separately as obtained from MODIS-Terra  
415 and Aqua for the periods Mar. 2000 – Feb. 2013 and 2003 – 2012, corresponding to local late morning-  
416 to-noon (Terra) and afternoon (Aqua) conditions, respectively. It is evident a gradual reduction of  
417 frequencies from south to north, while for the strong DD episodes also appears a west to east  
418 decreasing gradient. The decreasing south-to-north gradient of intense DD episodes' frequency, which  
419 is also in agreement with previous studies based on ground PM measurements (Querol et al., 2009b;  
420 Pey et al., 2013), model simulations (Papayannis et al., 2008; 2014) and AERONET AOD retrievals  
421 (Basart et al., 2009), can be attributed to the increasing distance from the major dust sources and to the  
422 higher precipitation amounts at the northern parts of the basin (e.g. Marriotti et al., 2002; Mehta and  
423 Yang, 2008).

424 The maximum frequencies (9.9 episodes  $\text{yr}^{-1}$ ) of strong DD episodes are observed in the western  
425 parts of the study region, for both periods and datasets, while the corresponding values for the extreme  
426 ones (3.3 episodes  $\text{yr}^{-1}$ ) are observed over the central Mediterranean Sea for MODIS-Terra (Mar. 2000  
427 – Feb. 2013). In general, there is similar spatial variability between Terra and Aqua, though slightly  
428 lower maximum frequencies are found for Aqua. Although dust episodes occur rarely across the  
429 northern parts of the study region (<1 and 0.5 episode  $\text{yr}^{-1}$  for strong and extreme episodes), their  
430 occurrence proves that dust particles can be transported far away from their sources, up to the central  
431 (e.g. Klein et al., 2010) or even northern (e.g. Bègue et al., 2012) European areas under favorable  
432 meteorological conditions. A noticeable difference between the two study periods and platforms is that  
433 relatively high frequencies of extreme DD episodes are recorded in more northern latitudes in the  
434 Mediterranean Sea, i.e. up to  $43^\circ$  N, according to MODIS-Terra over Mar. 2000 – Feb. 2013, while  
435 they are restricted south of  $40^\circ$  N parallel for MODIS-Aqua during 2003-2012. In order to investigate  
436 this difference in detail we have also applied the satellite algorithm, over the period 2003–2012, i.e.  
437 that of Aqua, using MODIS-Terra retrievals as inputs. Through this analysis (results not shown here), it  
438 is evident that there is a very good agreement between the satellite algorithm's outputs, for the periods  
439 Mar. 2000 – Feb. 2013 and 2003-2012, revealing a constant dust episodes' regime. Therefore, the

440 discrepancy appeared between MODIS-Terra and MODIS-Aqua spatial distributions, is attributed to  
441 the diurnal variation of factors regulating the emission and transport of dust particles from the sources  
442 areas. Schepanski et al. (2009), analyzed the variation of the Saharan dust source activation throughout  
443 the day, based on MSG-SEVIRI satellite retrievals, reporting that dust mobilization is more intense in  
444 the local early morning hours after sunrise. Note, that desert dust episodes over the period Mar. 2000 –  
445 Feb. 2013 have been identified based on observations retrieved by the Terra satellite, which flies over  
446 the study region around noon in contrast to Aqua which provides aerosol measurements at early  
447 afternoon hours.

448 The analysis has been also repeated (results not shown here) considering as inputs to the satellite  
449 algorithm only *AODs* associated with cloud fractions lower/equal than 0.8, in order to investigate  
450 possible modifications to our results (Figs 2 and 3) due to the cloud contamination effect. As it  
451 concerns the strong DD episodes, the geographical distributions are similar with those of Fig. 2, but the  
452 maximum frequencies (recorded in Morocco) are higher by up to 2 episodes  $\text{yr}^{-1}$  and 0.3 episodes  $\text{yr}^{-1}$   
453 for the MODIS-Terra (Mar. 2000 – Feb. 2013) and MODIS-Aqua (2003-2012) data set, respectively.  
454 On the contrary, in the case of extreme DD episodes the maximum frequencies decrease to 2.5 episodes  
455  $\text{yr}^{-1}$  for the period 2003-2012 and they shift southwards, namely over the northern coasts of Africa,  
456 while over the central parts of the Mediterranean Sea are lower than 1 episode  $\text{yr}^{-1}$ .

457 The maps of intensities (in terms of  $AOD_{550nm}$ ) of DD episodes (Figure 3), show that for both study  
458 periods and satellite platforms, the maximum intensities are over the Gulf of Sidra and the Libyan Sea,  
459 along the northern African coasts. These intensities reach *AODs* up to about 1.5 for strong and 4.1 for  
460 extreme episodes, while the minimum ones (values down to 0.25-0.46) are recorded in the northern and  
461 western Mediterranean parts. Note that dissimilar spatial patterns appear between the geographical  
462 distributions of DD episodes' frequency and intensity, indicating that these two features are determined  
463 by different factors (e.g. tracks or strength of depressions). Finally, when the cloud contamination is  
464 minimized using only *AODs* associated with *CF* lower than 0.8, then the maximum intensities are  
465 shifted southwards, across the northern Africa and eastern coasts of the Mediterranean, being lower  
466 than 1 and 2 for strong and extreme DD episodes, respectively. Through the rejection of possibly  
467 overestimated *AODs* from the dataset, it is found that the threshold levels are decreased (mainly over  
468 the most frequently dust affected areas) since both mean and standard deviation values are lower  
469 (results not shown here). Nevertheless, even though these *AODs* can be overestimated, in the majority  
470 of the cases the collocated AERONET *AODs* are high (but lower than the satellite observations)  
471 indicating the occurrence of desert dust outbreaks as it will be shown in Section 4.2.1.4.

472 The analysis has been also repeated applying the alternative METHOD-B described in Section 3.  
473 Just to ensure a longer temporal coverage, this analysis was done for the period Mar. 2000-Feb. 2013  
474 using MODIS-Terra data. The obtained results for the frequency of occurrence as well as for the  
475 intensity of DD episodes are depicted in Figures S1 and S2, respectively, in the supplementary  
476 material. The geographical patterns for the frequency of occurrence between the two methodologies are  
477 similar; however, the maximum values for the strong and extreme DD episodes can reach up to 13.3  
478 episodes year<sup>-1</sup> (Fig. S1-i) and 8.1 episodes year<sup>-1</sup> (Fig. S1-ii), respectively. As it concerns the intensity,  
479 the geographical patterns, particularly for the strong DD episodes, are dissimilar and less distinct  
480 compared to the corresponding ones obtained with the primary methodology. This difference is  
481 attributed to the inclusion of more dust episodes with variable intensity, which leads to a not so clear  
482 “signal” when all these episodes are averaged. Based on METHOD-B, the maximum intensities (in  
483 terms of  $AOD_{550nm}$ ) of strong DD episodes can reach up to 1 (Fig. S2-i) while for the extreme episodes  
484 (Fig. S2-ii) it can be as large as 3. The main finding, based on the intercomparison of the two  
485 methodologies for the identification of DD episodes, is that the frequency of the episodes is higher for  
486 the METHOD-B with respect to the primary methodology, while the intensity is decreased. Both facts  
487 are expected and can be explained by the lower calculated AOD thresholds with METHOD-B thus  
488 yielding more DD episodes of lower intensity.

489 This introductory analysis was conducted in order to specify the locations where the Mediterranean  
490 dust outbreaks occur more frequently and are more intense. Nevertheless, this paper is orientated to the  
491 description of the intense Mediterranean dust outbreaks’ vertical structure as well as to the detailed  
492 assessment of the applied satellite algorithm for the identification of DD episodes in order to  
493 consolidate our methodology, and not to emphasize on their regime, which has been thoroughly  
494 analyzed in Gkikas et al. (2013).

495

#### 496 4.2 Comparison of the satellite algorithm’s outputs against AERONET and PM<sub>10</sub> measurements

497 The ability of the satellite algorithm to identify satisfactorily DD episodes, is tested against ground  
498 measurements from 109 AERONET (Fig. 4, orange squares) and 22 PM<sub>10</sub> (Fig. 4, green triangles)  
499 stations located in the broader Mediterranean area. This is an extended and thorough comparison which  
500 exceeds largely a similar one done for the outputs of the previous version of satellite algorithm (2000-  
501 2007, Gkikas et al., 2013), but only relying on 9 AERONET stations and using  $AOD$  and volume size  
502 distribution data. Here, the comparison is repeated for the improved algorithm, being extended over a

503 longer time period, for a much larger number of AERONET stations, and an analysis of more optical  
504 properties, namely the Ångström exponent, effective radius, single scattering albedo and asymmetry  
505 parameter is made. The comparison is performed for both study periods and satellite platforms (Mar.  
506 2000 – Feb. 2013 for Terra and 2003-2012 for Aqua) while the issue of possible cloud contamination is  
507 also considered. However, since the obtained results revealed a very similar performance of the  
508 algorithm for both periods and platforms, only the results for the period Mar. 2000 – Feb. 2013 are  
509 given here.

510 In 46 out of 109 AERONET stations, depicted with yellow triangles in Figure 4, we have found at  
511 least one strong or extreme dust episode, for which coincident satellite and ground measurements are  
512 available. For the specific AERONET stations and episode days, the mean values of the selected  
513 AERONET aerosol optical properties have been calculated separately for strong, extreme and all (both  
514 strong and extreme) DD episodes identified by the satellite algorithm. Subsequently, these values were  
515 compared to the corresponding ones calculated from all the available retrievals (climatological  
516 conditions, clim) collected from the 109 Mediterranean AERONET stations, during the period Mar.  
517 2000 – Feb. 2013, aiming at highlighting the effect of episodes on these optical properties.  
518 Additionally, in 7 AERONET stations (cyan circles in Figure 4) the intense DD episodes have been  
519 identified from ground (AERONET) and the corresponding results are compared with the satellite  
520 algorithm outputs (Section 4.2.1.4). Finally, the performance of the algorithm is also tested against  
521 surface  $PM_{10}$  measurements from 22 stations (Section 4.2.2).

522

## 523 4.2.1 AERONET

### 524 4.2.1.1 Aerosol optical depth

525 During the period Mar. 2000 – Feb. 2013, 346 pixel level intense DD episodes have been identified  
526 by the satellite-based algorithm, in which coincident MODIS-Terra and AERONET retrievals are  
527 available. It should be noted that AERONET  $AOD_{550nm}$  values have been calculated from available  
528 AERONET  $AOD_{870nm}$  and Ångström exponent data ( $\alpha_{440-870nm}$ ) by applying the Ångström equation  
529 (Ångström, 1929) to match the MODIS  $AOD_{550nm}$ . For these intense DD episodes, the comparison  
530 between the satellite and ground aerosol optical depths at 550 nm is given in Figure 5. Two similar  
531 scatterplots with matched MODIS-AERONET data pairs are given. The first one (Fig. 5 i-a) is resolved  
532 by the number of level 2 (L2) measurements of 10 km x 10 km spatial resolution from which the

533 compared  $1^\circ \times 1^\circ$  level 3 (L3) *AODs* in the figure are derived. The second scatterplot (Fig. 5 i-b) is  
534 resolved by the spatial standard deviation inside the  $1^\circ \times 1^\circ$  geographical cell (level 3 *AODs*). Both  
535 scatterplots address the issue of level 3 *AOD* sub-grid spatial variability, which is essential when  
536 attempting comparisons against local surface-based *AOD* data like the AERONET.

537 The overall correlation coefficient (*R*) between MODIS and AERONET *AODs* is equal to 0.505,  
538 with the satellite *AODs* being overestimated (bias=0.143). From the overall scatterplots, it is evident  
539 the existence of outliers associated with small number of level 2 retrievals (<20, blue color Fig. 5 i-a)  
540 and/or high standard deviations (>0.5, yellowish-reddish points, Fig. 5 i-b) inside the L3 grid cell. This  
541 finding underlines the role of homogeneity and representativeness of L3 retrievals for the comparison  
542 of MODIS *AODs* against AERONET. This role is better visualized in Fig. 5 ii-a, where are presented  
543 the computed *R* values between MODIS level-3 and AERONET *AODs* depending on the number of L2  
544 retrievals from which the L3 products were derived. In general, it is known that the L2 pixel counts  
545 range from 0 to 121 while in polar regions (typically around  $82^\circ$  latitude) the maximum count numbers  
546 can be even higher due to overlapping orbits and near nadir views intersect (Hubanks et al., 2008). It is  
547 clear from our results that the correlation coefficients are gradually and essentially improved, from 0.49  
548 to 0.75, with increasing representativeness of MODIS *AODs*, i.e. increasing counts of L2 retrievals  
549 attributed. A similar improvement has been reported by Amiridis et al. (2013) who found a better  
550 agreement between MODIS/AERONET and CALIOP aerosol optical depths applying similar spatial  
551 criteria. The agreement between MODIS and AERONET also improves when the former *AOD*  
552 products are more spatially homogeneous, i.e. when they are characterized by smaller *AOD* standard  
553 deviations at the grid-level (from <0.25 down to <0.05, Fig. 5 ii-b). However, our results also indicate  
554 that apart from increasing correlation coefficients (up to 0.7-0.8) with increasing level-2 counts and  
555 decreasing standard deviations, the number of intense DD episodes is decreased dramatically (about  
556 40-50 for more than 50 counts and standard deviation smaller than 0.05).

557 In addition, the spectral variation of the AERONET *AODs* at 7 wavelengths, from 340 to 1020 nm,  
558 in climatological and dust episodes conditions has been investigated (results given in Figure S3,  
559 supplementary material). The *AOD* boxplots produced for all the available daily AERONET  
560 measurements (orange) and for the corresponding retrievals during strong (cyan), extreme (red) and all  
561 DD (green) episodes identified by the satellite algorithm show that the spectral variation of aerosol  
562 optical depth decreases in cases of dust episodes, with respect to the “climatological” conditions. This  
563 is mainly attributed to the further increasing *AOD* levels at wavelengths longer than 500 nm (by about  
564 6 times) than in (or near) the visible.

566 *4.2.1.2 Aerosol volume size distribution*

567 In Figure 6, are presented the mean aerosol volume size distributions (*AVSDs*) calculated from all  
568 available AERONET data (orange curve) as well as under strong (cyan curve), extreme (red curve) and  
569 all (green curve) DD episodes conditions. The results are given for Mar. 2000 – Feb. 2013 using  
570 MODIS-Terra (346 intense DD episodes) retrievals as inputs to the satellite algorithm. In the  
571 climatological curve, two modes are distinct centered at 0.15  $\mu\text{m}$  for the fine mode and 2.24  $\mu\text{m}$  for the  
572 coarse mode. There is an about equal contribution of both modes, indicating the coexistence of fine  
573 (e.g. urban aerosols) and coarse (e.g. dust aerosols) particles over the broader Mediterranean area. This  
574 result is in agreement with previous studies for the Mediterranean (e.g. Fotiadi et al., 2006; Mallet et  
575 al., 2013). However, under dust episode conditions, although the *AVSD* still has two modes, there is a  
576 dramatic increase of the coarse mode, which strongly dominates. More specifically, the peak of the  
577 coarse mode (radius between 1.7 and 2.24  $\mu\text{m}$ ) is increased by factors of about 10, 15 and 11 for the  
578 strong, extreme and all DD episodes. The differences between the strong and extreme *AVSDs* are  
579 statistically significant (confidence level at 95 %) for almost all size bins (18 out of 22) except bin 1  
580 (0.050  $\mu\text{m}$ ), 2 (0.065  $\mu\text{m}$ ), 6 (0.194  $\mu\text{m}$ ) and 7 (0.255  $\mu\text{m}$ ). Moreover, it should be noted that the  
581 increment factors are slightly decreased when the algorithm operates only with *AODs* associated with  
582 cloud fractions less than 0.8 which is reasonable since possible “overestimated” retrievals are masked  
583 out from the analysis. Similar modifications in the shape of *AVSD* during dust outbreaks have been  
584 pointed out by several studies in the past, either for the Mediterranean region (e.g. Kubilay et al., 2003;  
585 Lyamani et al., 2005; Córdoba-Jabonero et al., 2011) or for other dust affected areas of the planet (e.g.  
586 Alam et al., 2014; Cao et al., 2014).

587 *4.2.1.3 Size optical properties, single scattering albedo and asymmetry parameter*

588 The accuracy of the DD episodes identification method was further assessed by also using other  
589 AERONET aerosol optical properties than *AOD*, namely the Ångström exponent ( $\alpha$ ) and the effective  
590 radius ( $r_{\text{eff}}$ ), able to provide information about particles' size. For both aerosol optical properties, the  
591 boxplots for all the available AERONET retrievals as well as for the corresponding data during strong,  
592 extreme and all DD episodes, have been produced and depicted in Figure S4 (supplementary material).

593 Based on our results, the appropriateness of the applied methodology is confirmed by the drastic  
594 reduction of  $\alpha$  and increase of  $r_{\text{eff}}$  values when dust outbreaks occur. When all available AERONET  
595 retrievals are considered (clim), the majority (>75%) of  $\alpha$  values is higher than 1.04 indicating the

596 strong presence of fine particles in the study domain. On the contrary, during intense dust episodes the  
597 majority of the corresponding values for all and strong DD episodes are lower than 0.54 while for the  
598 extreme ones are lower than 0.36. Such low Ångström exponent values, attributed to transported  
599 mineral particles from the northern African deserts (Pace et al., 2006), have been reported also in  
600 previous studies (e.g. Tafuro et al. 2006; Basart et al., 2009). The existence of coarse aerosols is also  
601 confirmed by the increase of  $r_{eff}$  values under intense DD conditions compared to the climatological  
602 levels. For all DD episodes, the 75% of  $r_{eff}$  values is higher than 0.55  $\mu\text{m}$  reaching up to 1.4  $\mu\text{m}$ , while  
603 the mean and the median values are equal to about 0.73, compared to about 0.37 for the climatological  
604 conditions. These values are even higher when extreme DD episodes are concerned.

605 Moreover, the spectral variations of the averaged AERONET single scattering albedo ( $SSA$ ) and the  
606 asymmetry parameter ( $g_{aer}$ ) are also studied. During intense dust outbreaks the shape and magnitude of  
607 spectral  $SSA$  (Figure S5-i) and  $g_{aer}$  (Figure S5-ii) are modified compared to the climatological  
608 conditions. The spectral curves of both parameters become less and more flattened during dust episodes  
609 for  $SSA$  and  $g_{aer}$ , respectively. For  $SSA$ , the steepening results from decreasing values in the visible and  
610 increasing values in the near-infrared (by up to 0.04, reaching 0.97 at 1020 nm). The flattening for  $g_{aer}$   
611 arises from smaller and larger increments in visible and near-infrared values, by up to 0.04 and 0.07,  
612 respectively. The differences between strong and extreme DD episodes  $SSA$  spectral curves are  
613 statistically significant at 95 % confidence level only at 870 and 1020 nm. On the contrary, the  
614 corresponding differences for the  $g_{aer}$  are statistically significant in all wavelengths. Our results are in  
615 agreement with those presented for  $SSA$  by Mallet et al. (2013) in the Mediterranean and for  $g_{aer}$  by  
616 Alados-Arboledas et al. (2008) during a dust episode over the southeastern parts of Spain.

617

#### 618 *4.2.1.4 Intercomparison of surface-based and satellite algorithms used for the identification of the* 619 *desert dust episodes*

620 Despite their great usefulness, satellite aerosol retrievals still suffer from uncertainties, and  
621 generally are considered as inferior to surface-based similar products, which are taken as the reference.  
622 In order to examine this degree of uncertainty and to verify the successful performance of the  
623 algorithm, we also tested using it along with AERONET retrievals. This has been made for 7  
624 Mediterranean AERONET stations, depicted with cyan circles in Figure 4, during the periods for which  
625 ground retrievals are available (Table 1). The selection of the AERONET stations was based on: (i)  
626 data availability (see last column of Table 1), (ii) their location (i.e. near to the Northern African and

627 Middle East deserts) and (iii) the inclusion of sites where the aerosols' regime is complex (e.g. El  
628 Arenosillo, FORTH Crete). The intense DD episodes were identified following the methodology  
629 described in section 3, but using only  $AOD$  at 870 nm,  $\alpha_{440-870nm}$  (lower/equal than 0.7) and  $r_{eff}$  (higher  
630 than 0.6) as criteria, based upon their availability from AERONET. Subsequently, the algorithm was  
631 also operated again using satellite (MODIS-Terra, OMI-Aura, EP-TOMS) input data for the days with  
632 available retrievals in each of the 7 AERONET stations.

633 In Figure 7, we present the overall scatterplots between satellite and ground  $AODs$  when intense  
634 DD episodes have been identified based on the ground (left column) and the satellite (right column)  
635 algorithm. Colors in Figs. 7 i-a, 7 ii-a, 7 iii-a represent the associated MODIS-Terra Ångström  
636 exponent, effective radius and day cloud fraction (CFD) retrievals, respectively. In Figs. 7 i-b and 7 ii-b  
637 colors represent the AERONET Ångström exponent and effective radius, respectively, while in Figure  
638 7 iii-b represent the day cloud fraction observations derived by MODIS-Terra. Through this approach it  
639 is feasible to assess furthermore the performance of the satellite algorithm, specify its drawbacks and  
640 check the validity of the defined thresholds (green boxes in Figure 1).

641 It is apparent that the agreement between MODIS-Terra and AERONET  $AODs$  is better when DD  
642 episodes are identified from the ground, as shown by the increased correlation coefficients (from 0.521  
643 to 0.704), increased slopes (from 0.6 to 0.9-1.0) and decreased biases (from 0.16 to -0.03). In  
644 particular, when DD episodes are identified from space, the MODIS-Terra  $AOD$  retrievals are  
645 overestimated (bias=0.163) with regards to AERONET, particularly at low  $AOD$  values (<0.5). In both  
646 algorithms, the highest overestimations are associated with cloud fractions higher than 0.7 due to the  
647 possible contamination of the satellite  $AODs$  by clouds (Figure 7 iii-a, iii-b). Given that DD episodes'  
648 identification based on AERONET retrievals is more efficient, we have used these results in order to  
649 check the validity of the defined thresholds for  $\alpha$ ,  $AI$ ,  $FF$  and  $r_{eff}$  (green boxes in Figure 1) used in the  
650 satellite algorithm. For each aerosol optical property, it has been calculated the percentage of intense  
651 DD episodes for which the corresponding satellite observations are below or above the defined  
652 thresholds, depending on the parameter. The results given in Table 2 are satisfactory, since the  
653 percentages range from 87 to 99%, and confirm the validity of the defined thresholds.

654 The scatterplots in Figs. 7 i-b and ii-b also reveal some weaknesses of the satellite-based algorithm.  
655 More specifically, it is found that for few DD episodes identified by the satellite algorithm the  
656 corresponding AERONET Ångström exponent and effective radius values are higher than 1 and  
657 smaller than 0.4, respectively. These values indicate a predominance of fine particles instead of coarse

658 ones as it would be expected for desert dust aerosols. In order to quantify the number of misclassified  
659 pixel level intense DD episodes by the satellite algorithm, we have computed the percentage of cases  
660 for which the AERONET  $\alpha$  values are higher than 1 (15%) and  $r_{eff}$  values are lower than 0.4 (17.7%).  
661 Also, we have repeated these calculations for all DD episodes (Section 4.2.1.1) and the corresponding  
662 percentages were found to be equal to 11.8% and 14.5%, respectively. These misclassifications of the  
663 satellite algorithm occur in AERONET stations (e.g. Thessaloniki, Rome, Avignon) with a strong  
664 presence of anthropogenic aerosols (Kazadzis et al., 2007; Gobbi et al., 2007; Querol et al., 2009a;  
665 Yoon et al., 2012). Some misclassifications also occur in AERONET stations (e.g. Evora, El  
666 Arenosillo, FORTH CRETE) with mixed (natural plus anthropogenic) aerosol loads (Fotiadi et al.,  
667 2006; Toledano et al., 2007b; Hatzianastassiou et al., 2009; Pereira et al., 2011). Over these areas, there  
668 are converging air masses carrying particles of different origin, as shown by performed back-  
669 trajectories analyses (results are not shown here) using the HYSPLIT (HYbrid Single-Particle  
670 Lagrangian Integrated Trajectory) model (Draxler and Rolph, 2015). Nevertheless, it must be  
671 mentioned that DD episodes' misclassifications can be attributed to the lower accuracy of MODIS  
672 aerosol size retrievals over land (Section 2.1.1).

673

#### 674 4.2.2 PM<sub>10</sub> and dust contribution

675 The satellite algorithm's outputs, apart from AERONET retrievals, have been also compared  
676 against ground PM<sub>10</sub> concentrations ( $\mu\text{g m}^{-3}$ ) measured in 22 Mediterranean stations (green triangles in  
677 Figure 4).

678 First, for each station, the number of intense DD episodes was calculated, for which coincident  
679 satellite and ground measurements (total PM<sub>10</sub>) are available (Figure 8-i). The number of concurrent  
680 DD episodes varies from 3 to 53, being in general decreasing from southern to northern stations. For 14  
681 out of 22 stations, where at least 10 intense DD episodes were identified by the satellite-based  
682 algorithm, we have computed the correlation coefficients between satellite *AODs* and surface total  
683 PM<sub>10</sub> concentrations (Fig. 8-ii). The highest R values (up to 0.8) are recorded in the central and eastern  
684 parts of the Mediterranean while the lowest ones are found in the western stations. It must be noted that  
685 the correlation coefficients are affected by outliers, because of the limited number of DD episodes in  
686 each station, highlighting the sensitiveness of the intercomparison. Such outliers can be expected when  
687 satellite-based columnar *AODs* and surface-based PM<sub>10</sub> data are compared, since satellite *AODs* are  
688 representative for the whole atmospheric column in contrast to in-situ PM measurements which are

689 more representative for the lowest part of the planetary boundary layer affected also by local factors.  
690 Therefore, the vertical distribution of desert dust load, as it will be presented in the next sections, can  
691 determine the level of agreement between satellite *AODs* and surface PM concentrations. Another  
692 influencing factor can be cloud contamination of MODIS *AOD*.

693 The identification method by the satellite algorithm can be considered as correct when dust PM<sub>10</sub>  
694 concentrations are higher than zero (i.e. dust has been recorded at the station). According to this, the  
695 ratio between the number of non-zero dust PM observations and the number of DD episodes  
696 (coincident satellite-derived DD episodes and total PM<sub>10</sub> measurements) for each station is defined as  
697 success score. The calculated success scores (Figure 8-iii) vary from 68% (Monagrega, northeastern  
698 Spain, 28 episodes) to 97% (Boccadifalco, Sicily, 33 episodes) confirming the appropriateness of the  
699 DD episodes' identification. In the majority of stations, the contribution of dust particles to the total  
700 burden (Figure 8-iv) is above 50%, ranging from 44% (Zarra, Spain) to 86.8% (Ayia Marina, Cyprus).  
701 In order to complete our analysis we have also calculated the mean (Figure 8-v) and the median (Figure  
702 8-vi) dust PM<sub>10</sub> concentrations for the identified intense DD episodes in each station. The mean PM<sub>10</sub>  
703 concentrations mainly vary between 20 and 50  $\mu\text{g m}^{-3}$ , being higher in the southern stations, as  
704 expected. The minimum mean value (17  $\mu\text{g m}^{-3}$ ) was recorded in Censt (Sardinia) and the maximum  
705 one (223  $\mu\text{g m}^{-3}$ ) in Ayia Marina (Cyprus). Our values are much higher than the corresponding ones in  
706 Querol et al. (2009b), who obtained that the mean levels of mineral matter in PM<sub>10</sub> during dusty days  
707 range from 8 to 23  $\mu\text{g m}^{-3}$  based on ground concentrations derived by 21 Mediterranean stations. These  
708 differences are reasonable since here only intense desert dust outbreaks associated with high aerosol  
709 optical depths are considered. Finally, the median PM<sub>10</sub> concentrations are lower compared to the  
710 average ones, indicating that outliers (cases with extremely high *AOD* or PM<sub>10</sub>) can alter the results,  
711 attributed to the fact that both parameters' (*AOD* and PM<sub>10</sub>) distributions are not Gaussians. For this  
712 reason the highest differences are found in Finokalia (Crete) and Agia Marina (Cyprus), where the  
713 maximum daily PM<sub>10</sub> concentrations, equal to 690 and 1291  $\mu\text{g m}^{-3}$ , respectively, were recorded during  
714 an intense dust outbreak affected the eastern Mediterranean on 24 and 25 February 2006.

715

#### 716 4.3 Vertical structure of the Mediterranean desert dust outbreaks

717 The ability of the developed satellite algorithm to detect intense dust episodes has been proved  
718 adequate through the comparison analysis against AERONET retrievals and PM<sub>10</sub> concentrations.  
719 Nevertheless, its main limitation is that it uses columnar satellite retrievals and not vertical resolved

720 data prohibiting thus the description of the vertical structure of these dust outbreaks. In order to address  
721 this issue, the CALIOP-CALIPSO retrievals are used as a complementary tool to the satellite  
722 algorithm's outputs. First, for the identified dust episodes by the satellite algorithm, the spatially and  
723 temporally collocated vertically resolved CALIOP lidar observations are selected. For these cases and  
724 for each  $1^\circ \times 1^\circ$  grid cell, we have divided the lower troposphere, up to 8 km, in 16 layers of 500  
725 meters height. In this way, 14400 boxes of  $1^\circ \times 1^\circ$  surface area and 500 meters height have been  
726 produced. Then, for each one of them, we have calculated the overall number of dust and polluted dust  
727 observations (hereafter named as dust) according to the aerosol subtyping scheme of the CALIOP  
728 Vertical Feature Mask (VFM). Note that dust and polluted dust were chosen because in previous  
729 studies (Mielonen et al., 2009) they were shown to be the best two defined aerosol types among the  
730 other ones classified by the CALIOP VFM. Nevertheless, in case of polluted dust, Burton et al. (2013)  
731 reported that dust particles can be mixed with marine aerosols instead of smoke or pollution as assumed  
732 by the VFM retrieval algorithm. In our study, more than 95% of the aerosol type records were pure  
733 dust, for the collocated cases between the satellite algorithm and CALIPSO observations. In addition,  
734 in the majority of the defined boxes, the percentage of dust from the overall observations is higher than  
735 70%, confirming furthermore the validity of the algorithm DD episodes' identification procedure. This  
736 is an excellent proof of the successful identification of DD episodes by the satellite algorithm, since  
737 CALIOP-CALIPSO is an independent and vertically resolved platform and database. Thereby,  
738 CALIOP vertical observations were subsequently used to examine the vertical structure of dust  
739 outbreaks.

740 In order to analyze the intensity of desert dust outbreaks at different altitudes in the troposphere, the  
741 CALIOP data of the total backscatter coefficient at 532 nm ( $\beta_{532nm}$ ) have been also acquired. For each  
742 box, the average  $\beta_{532nm}$  values have been calculated from all the available CALIOP measurements (day  
743 and night), for the identified intense dust episodes by the satellite algorithm. More specifically, the  
744 average  $\beta_{532nm}$  values were calculated for the dust observations based on the CALIOP VFM associated  
745 with CAD scores ranging from -100 to -20, as it has been proposed by Winker et al. (2013) for  
746 discriminating aerosol from clouds. The selection of  $\beta_{532nm}$  values instead of extinction coefficients  
747 ensures that incorrect lidar ratio assumptions in the CALIOP retrieval algorithm do not affect our  
748 results. In the literature, it has been documented that the CALIOP lidar ratio is underestimated over the  
749 northern African deserts and the surrounding areas affected by Saharan dust particles, leading to an  
750 underestimation of the columnar *AOD* compared to MODIS and AERONET retrievals (Redemann et  
751 al., 2012; Schuster et al., 2012). Amiridis et al. (2013) stated that an increase of the lidar ratio from 40

752 to 58 sr, along with a series of post-corrections in the CALIOP retrievals and the implementation of  
753 several criteria concerning the cloud coverage and the spatial representativeness, can improve  
754 substantially the agreement between MODIS-Aqua/AERONET and CALIOP observations.

755 It should be noted that in the present work, we have analyzed all the available CALIOP overpasses  
756 (~ 10000) over the study region, during the period Jun. 2006 – Feb. 2013. For brevity reasons,  
757 however, only the obtained results based on MODIS-Terra retrievals are presented here, since similar  
758 findings are drawn for MODIS-Aqua (Jun. 2006 – Dec. 2012). Moreover, the analysis (results are not  
759 shown here) has been made separately for the identified strong and extreme DD episodes without  
760 revealing remarkable differences in the geometrical characteristics of dust outbreaks. Nevertheless, the  
761  $\beta_{532nm}$  values are higher for the extreme DD episodes being consistent with the discrimination of dust  
762 episodes' intensity (in terms of *AOD*) which is applied to the satellite algorithm. In order to facilitate  
763 the visualization of our results, for each column ( $1^\circ \times 1^\circ$  spatial resolution) and latitudinal/longitudinal  
764 zone ( $1^\circ$  degree), we have calculated the overall number of dust observations and the associated  
765 weighted averages of  $\beta_{532nm}$ , depending on the projection plane (latitudinal, longitudinal and columnar),  
766 according to dust observations in each box. For both parameters, the analysis has been made on an  
767 annual and seasonal basis and the corresponding results are discussed in Sections 4.3.1 and 4.3.2,  
768 respectively.

769

#### 770 4.3.1 Annual characteristics

771 In Figure 9, are presented the three dimensional structures of the CALIOP overall dust observations  
772 (Fig. 9-i) and the associated total backscatter coefficients at 532 nm (Fig. 9-ii), during intense dust  
773 episodes conditions, over the broader Mediterranean area, for the period Jun. 2006 – Feb. 2013. From  
774 the latitudinal projection in Fig. 9-i, it is evident that dust particles are mainly detected between 0.5 and  
775 6 km, and more rarely up to 8 km, between the parallels  $32^\circ$  N and  $38^\circ$  N. The number of dust  
776 observations is increased at higher altitudes with increasing latitudes, up to  $40^\circ$  N, while the altitude  
777 range (thickness) where these records are detected is gradually reduced from 4 to 2 km. At northern  
778 latitudes, the CALIPSO dust records are drastically reduced and are mainly observed between 1 and 4  
779 km. The ascending mode of the transported mineral particles over the Mediterranean is attributed to the  
780 prevailing low pressure systems, which mobilize and uplift dust particles from the source areas across  
781 the Sahara Desert and the Arabian Peninsula. Dust aerosols are transported over the planetary boundary  
782 layer (Hamonou et al., 1999) due to the upward movement of dry and turbid air masses (Dulac et al.,

783 1992), while the prevailing synoptic conditions determine also the spatial and temporal characteristics  
784 of desert dust outbreaks over the Mediterranean (Gkikas et al., 2014).

785 In general, our results are in agreement with previous studies, based on lidar profiles, which have  
786 been made in several Mediterranean sites. More specifically, Papayannis et al. (2008) found that dust  
787 layers, over the EARLINET Mediterranean stations, extend from 0.5 to 10 km above mean sea level,  
788 their center of mass is located between 2.5 and 3.5 km and their thickness ranges from 2.1 to 3.3 km.  
789 Hamonou et al. (1999) reported that dust layers are mainly detected between 1.5 and 5 km based on  
790 lidar measurements in the northwestern and northeastern Mediterranean. According to di Sarra et al.  
791 (2001), who studied the Saharan dust intrusions in Lampedusa (central Mediterranean) for the period  
792 May-June 1999, dust particles can be detected up to 7-8 km, which is in line with our findings for the  
793 corresponding latitudinal zones ( $35^{\circ}$  N -  $36^{\circ}$  N). Balis (2012), analyzed 33 Raman/lidar profiles of  
794 Saharan dust intrusions over Thessaloniki (northern Greece), and found that the mean base and top of  
795 dust layers were equal to  $2.5 \pm 0.9$  and  $4.2 \pm 1.5$  km, respectively.

796 As to the variation of vertical extension with longitude (Fig. 9-i), it is revealed that the base height  
797 of dust layers is decreased towards the eastern parts of the study region. In the western Mediterranean,  
798 the mineral particles are mainly detected between 2 and 6 km while over the central and eastern  
799 Mediterranean the corresponding altitudes are equal to 0.5 and 6 km, respectively. It is well known,  
800 that dust is transported over the western Mediterranean mainly in summer (e.g. Moulin et al., 1998)  
801 favored by low pressure systems located over the northwestern Africa (Gkikas et al., 2014) and the  
802 enhanced thermal convection, uplifting effectively dust aerosols at high altitudes in the troposphere.  
803 Moreover, air masses carrying dust particles are “convected” towards higher altitudes due to the  
804 existence of the Atlas Mountains Range. Therefore, the combination of strong convective processes  
805 over North Africa along with topography can explain the identification of dust aerosols at higher  
806 tropospheric levels over the western Mediterranean. It is the presence of mineral particles at high  
807 altitudes in western Mediterranean that can explain the poor-to-moderate agreement between  $PM_{10}$   
808 concentrations and MODIS *AODs* found in the Iberian Peninsula (Fig. 8-ii). In order to give a better  
809 insight to how the dust outbreaks’ vertical extension can affect the level of agreement between  
810 columnar AOD satellite retrievals and ground  $PM_{10}$  concentrations, emphasis is given at specific dust  
811 events and the relevant findings will be discussed in section 4.4. In the central and eastern parts of the  
812 Mediterranean basin, air masses carrying African dust aerosols travel at lower altitudes over Africa  
813 because of absence of significant topographical objects on their route, as suggested by Pey et al.  
814 (2013).

815 Previous studies have shown that dust layers over the Mediterranean are characterized by a  
816 multilayered structure (e.g. Hamonou et al., 1999; Mona et al., 2006; Papayannis et al., 2008). This is  
817 also depicted in the longitudinal projection of Figure 9-i, where several dust layers of different base/top  
818 altitudes and geometrical thicknesses are detected. In general, the base heights vary from 0.5 to 2 km,  
819 the top heights from 4 to 6 km and the thicknesses from 1 to 4 km. The majority of common  
820 observations between the CALIOP profiles and the identified intense DD episodes by the satellite  
821 algorithm are recorded over the maritime parts of the study region (bottom map of Fig. 9-i). The  
822 maximum number of CALIOP dust observations (~ 19000) is recorded along the Atlantic coasts of  
823 Morocco, but high numbers (about 10000 – 15000) are also found across the northern African coasts.

824 Apart from the CALIOP dust observations, we have also analyzed the associated  $\beta_{532nm}$  values at  
825 the defined altitude ranges in order to describe the variation of intensity of the desert dust episodes with  
826 height over the Mediterranean (Fig. 9-ii). The maximum backscatter coefficients (up to  $0.006 \text{ km}^{-1} \text{ sr}^{-1}$ )  
827 are observed below 2 km, being increased towards the southern edges ( $30^\circ \text{ N} - 34^\circ \text{ N}$ ) of the study  
828 region, where their source areas are found. This is explained by the fact that dust particles due to their  
829 coarse size and large mass, are efficiently deposited and for this reason they are recorded at higher  
830 concentrations near to the source areas and at low altitudes. Nevertheless, the decreasing intensity with  
831 height towards the north is not so evident. Thus, high  $\beta_{532nm}$  values ( $\sim 0.004 \text{ km}^{-1} \text{ sr}^{-1}$ ) are observed  
832 between 2 and 4 km in the latitudinal zone extending from  $35^\circ \text{ N}$  to  $42^\circ \text{ N}$ . Though, the uppermost  
833 altitudes where relatively high  $\beta_{532nm}$  values gradually decrease from 6 to 4 km, moving from south to  
834 north. Any differences in the latitudinal patterns of dust observations and backscatter values (Figs 9-i  
835 and 9-ii) can be explained by the fact that  $\beta_{532nm}$  values take into account only the dust records and not  
836 the overall observations (all aerosol types).

837 The decrease of backscatter values at higher altitudes has been pointed out in previous studies  
838 where lidar profiles have been analyzed over specific Mediterranean locations (e.g. Mona et al., 2006;  
839 Papayannis et al., 2008). Nevertheless, it must be considered that in the aforementioned studies the  
840 lidar measurements are valid above the retrieved planetary boundary layer (Matthias et al., 2004) which  
841 varies depending on the location and the season (McGrath-Spangler et al., 2013). Despite the good  
842 agreement, as it concerns the vertical shape of the  $\beta_{532nm}$  curves, between our findings and the  
843 corresponding ones based on ground retrievals, in the present analysis the calculated backscatter  
844 coefficients are in general higher, which is reasonable since are considered only cases of intense desert  
845 dust outbreaks.

846 The longitudinal pattern of  $\beta_{532nm}$  profiles (Fig. 9-ii) is less distinct compared to the corresponding  
847 one resulted from the latitudinal projection. Relatively high  $\beta_{532nm}$  values ( $\sim 0.004 \text{ km}^{-1} \text{ sr}^{-1}$ ) are found  
848 between 1 and 5 km over the western Mediterranean, while over the central and eastern parts of the  
849 study region the desert dust outbreaks' intensity ( $\sim 0.006 \text{ km}^{-1} \text{ sr}^{-1}$ ) is higher below 1.5 km. Among the  
850 sub-regions, the backscatter coefficients are higher in the central and eastern Mediterranean, which is  
851 also depicted in the bottom map of Fig. 9-ii. It is reminded that higher intensities of dust episodes over  
852 the central and eastern Mediterranean have also been noticed based on MODIS retrievals (Figure 3).  
853 From the obtained longitudinal projection, it is evident a patchy structure of the total backscatter  
854 coefficient profiles, especially in the central and eastern parts, indicating the existence of several dust  
855 layers of varying intensities at different altitudes into the atmosphere.

856 The three dimensional plots of Figures 9-i and 9-ii, have been also reproduced considering all the  
857 available dust and polluted dust CALIOP-CALIPSO records, without taking into account the satellite  
858 algorithm's outputs (for intense dust outbreaks). The obtained results for the number of observations  
859 and  $\beta_{532nm}$  are presented in Figures S6-i and S6-ii, respectively. Note, that for each studied parameter  
860 the colorbar scales in Figure 9 and S6 are not identical because the number of observations for dust  
861 average conditions (Fig. 6-i) is extremely larger than the corresponding one during intense dust  
862 outbreaks (Fig. 9-i) while the opposite is found for the  $\beta_{532nm}$  values (Fig. 9-ii and Fig. 6-i). It is  
863 apparent that the latitudinal projections calculated for the intense dust outbreaks (Fig. 9-i) and for all  
864 the available CALIOP dust records (Fig. S6-i) reveal different patterns. More specifically, when all  
865 available CALIOP dust records are considered, it is found that dust aerosols are mainly confined  
866 between 1 and 3 km in the southernmost parts of the study region while the number of observations  
867 gradually decreases at higher altitudes and towards northern latitudes (Fig. S6-i). On the contrary,  
868 during dust outbreaks, mineral particles are transported over the Mediterranean following an ascending  
869 path, as it is depicted in the latitudinal projection of Figure 9-i. Nevertheless, it must be mentioned that  
870 over the desert areas there is a full coverage (see bottom map in Fig. S6-i) when all dust CALIOP  
871 records are considered in contrast to intense dust outbreaks (see bottom map in Fig. 9-i) attributed to  
872 the absence of DT retrievals, used as inputs to the satellite algorithm, over bright surfaces. The  
873 comparison between the longitudinal projections during intense dust outbreaks (Figure 9-i) and during  
874 average dust conditions (Fig. S6-i) reveals less remarkable differences than for the latitudinal  
875 projections. According to the longitudinal projection of Figure S6-i, in the western Mediterranean, dust  
876 layers are confined between 1 and 6 km, while their base and top altitude both decrease down to 0.5  
877 and 4.5 km, respectively, for increasing longitudes. In the easternmost part of the study region, dust

878 layers are mainly confined between 1 and 3 km, while its top height can reach up to 5 km. The intensity  
879 of dust loads (in terms of  $\beta_{532nm}$ ) is lower than  $0.003 \text{ km}^{-1} \text{ sr}^{-1}$  regardless the projection plane for  
880 average dust conditions based on CALIOP-CALIPSO lidar profiles (Fig. S6-ii). Moreover, the intensity  
881 of dust loads decreases gradually with height as well as from south to north revealing a distinct pattern  
882 in all projection planes in contrast to the corresponding ones found during desert dust outbreaks (Fig. 9-  
883 ii).

884

#### 885 *4.3.2 Seasonal characteristics*

886 The vertical structure of the Mediterranean desert dust outbreaks has also been analyzed separately  
887 for winter (DJF), spring (MAM), summer (JJA) and autumn (SON). The seasonal three dimensional  
888 representations of the CALIOP overall dust observations and the associated total backscatter  
889 coefficients are depicted in the left and right column of Figure 10, respectively. It must be noted, that  
890 for  $\beta_{532nm}$  the colorbars' ranges are common, depending on the projection plane. More specifically, the  
891 maximum limits have been set to  $0.012 \text{ km}^{-1} \text{ sr}^{-1}$ ,  $0.014 \text{ km}^{-1} \text{ sr}^{-1}$  and  $0.021 \text{ km}^{-1} \text{ sr}^{-1}$  for the latitudinal,  
892 longitudinal and bottom map projections, respectively. It should be mentioned that  $\beta_{532nm}$  values can  
893 reach up to  $0.045 \text{ km}^{-1} \text{ sr}^{-1}$ , but are associated with a very small number of dust observations.

894 The majority (85%) of dust observations is recorded in spring and summer, attributed to the  
895 enhanced production rates of mineral particles and the prevailing atmospheric circulation over the  
896 source areas and the Mediterranean. According to the latitudinal projections, it is evident a seasonal  
897 variability of the intense Mediterranean desert dust outbreaks' geometrical characteristics. Dust  
898 particles are detected at higher altitudes (6-7 km) during warm seasons of the year while in winter are  
899 mainly detected below 3 km and in autumn are recorded between 2 and 5 km. Nevertheless, it should  
900 be mentioned that during these seasons only a small number of pixels (see bottom maps in Figs. 10 i-a,  
901 iv-a) is available considering also that clouds prohibit the satellite observations. Note that in spring,  
902 dust can be found at low tropospheric levels while in summer it is mainly observed above 1 km  
903 highlighting thus the role of topography and the enhanced thermal convection. During the first half of  
904 the year, the maximum dust observations are confined between the parallels  $31^\circ \text{ N}$  and  $37^\circ \text{ N}$  while  
905 during the second one, are shifted northwards in the latitudinal zone extending from  $34^\circ \text{ N}$  to  $40^\circ \text{ N}$ .  
906 Similar latitudinal projections were also presented by Luo et al. (2015), for the same zonal areas of the  
907 study region, who developed a new algorithm to improve CALIOP's ability to detect optically thin dust  
908 layers. From the longitudinal projections as well as from the bottom maps, it is evident that the

909 maximum dust records are found in different Mediterranean sub-regions, depending on the season. The  
910 geometrical characteristics, in longitudinal terms, of intense DD episodes affecting the western, central  
911 and eastern parts of the Mediterranean are similar to those presented in the annual three dimensional  
912 structure (Fig. 9-i) being more frequent in the eastern and central Mediterranean in winter, spring and  
913 autumn and in the western and central Mediterranean in summer.

914 The seasonal patterns of  $\beta_{532nm}$  latitudinal projections are different than those for the dust  
915 observations, while they also differ among the four seasons. The intensity of winter DD episodes is  
916 stronger (up to  $0.012 \text{ km}^{-1} \text{ sr}^{-1}$ ) below 2 km and at the southern parts of the study region. According to  
917 the longitudinal and bottom map projections, these episodes take place over the central and eastern  
918 Mediterranean Sea but the number of grid cells with coincident CALIOP observations and DD episodes  
919 is limited. In spring, the highest  $\beta_{532nm}$  values (up to  $0.006 \text{ km}^{-1} \text{ sr}^{-1}$ ) are recorded between the parallels  
920  $31^\circ \text{ N}$  and  $35^\circ \text{ N}$  and below 2 km, although, relatively high  $\beta_{532nm}$  values (up to  $0.004 \text{ km}^{-1} \text{ sr}^{-1}$ ) are  
921 found up to 6 km (Fig. 10 ii-b). Moving northwards, over the Mediterranean, dust layers are mainly  
922 confined between 2 and 4 km, associated with high  $\beta_{532nm}$  values (up to  $0.004 \text{ km}^{-1} \text{ sr}^{-1}$ ) in the  
923 latitudinal zone extending from  $35^\circ \text{ N}$  to  $43^\circ \text{ N}$ . The existence of these elevated dust layers, has been  
924 also confirmed by model simulations through specific (Papayannis et al., 2008; 2014) or averaged  
925 (Alpert et al., 2004) cross sections of dust concentrations in the central sector of the Mediterranean.  
926 This is in accordance with our longitudinal projection (Fig. 10 ii-b), where  $\beta_{532nm}$  is high varying from  
927  $0.004$  to  $0.008 \text{ km}^{-1} \text{ sr}^{-1}$  at these altitude ranges.

928 In summer, the intensity of dust episodes is smoothly decreased at higher altitudes, where dust  
929 layers of considerable  $\beta_{532nm}$  values are also found. More specifically, the highest backscatter  
930 coefficients (up to  $0.008 \text{ km}^{-1} \text{ sr}^{-1}$ ) are recorded near to the surface but also moderate values (up to  
931  $0.006 \text{ km}^{-1} \text{ sr}^{-1}$ ) are observed between 2 and 5 km, particularly over the southern parts of the study  
932 region (Fig. 10 iii-b). Most of these intense DD episodes occur in the western Mediterranean, where the  
933 highest  $\beta_{532nm}$  values (up to  $0.005 \text{ km}^{-1} \text{ sr}^{-1}$ ) are recorded between 2 and 5 km. Over the central and  
934 eastern Mediterranean, even higher  $\beta_{532nm}$  values are found (up to  $0.014 \text{ km}^{-1} \text{ sr}^{-1}$ ) but at lower altitudes  
935 ( $< 1 \text{ km}$ ). In autumn, the majority of the grid cells of coincident CALIOP profiles and DD episodes  
936 identified by the satellite algorithm are located between the parallels  $33^\circ \text{ N}$  and  $41^\circ \text{ N}$ . In this  
937 latitudinal zone, CALIOP profiles are available over the interior parts of the Iberian Peninsula and over  
938 western and central parts of the Mediterranean Sea, near to the northern African coasts. According to  
939 the latitudinal projection,  $\beta_{532nm}$  values mainly vary from  $0.002$  to  $0.009 \text{ km}^{-1} \text{ sr}^{-1}$ , revealing an  
940 increasing tendency for increasing heights. On the contrary, the total backscatter coefficients do not

941 show a distinct spatial pattern on the longitudinal projection, due to the limited number of grid cells  
942 participating in the calculations. Throughout the year, based on the CALIOP  $\beta_{532nm}$  retrievals, the DD  
943 episodes are more intense (up to  $0.018 \text{ km}^{-1} \text{ sr}^{-1}$ ) in spring, when massive dust loads are transported  
944 from the Sahara desert towards the central and eastern parts of the Mediterranean Sea (bottom map in  
945 Fig. 10 ii-b).

946

#### 947 4.4. Intercomparison of satellite AOD and PM<sub>10</sub> concentrations for specific desert dust outbreaks

948 In Section 4.2.2, it has been shown that the agreement between the satellite algorithm's outputs and  
949 PM<sub>10</sub> concentrations is better in the central and eastern Mediterranean with regards to the western parts  
950 (Figure 8-ii). This discrepancy has been mainly attributed to the higher altitude of dust layers' base  
951 over the western sector of the study domain (Figure 9-i), in relation to the existing areal orography.  
952 Here, aiming at addressing how dust layers' geometrical characteristics influence the agreement  
953 between columnar AOD satellite and ground PM<sub>10</sub> measurements, specific desert dust outbreaks that  
954 took place over the PM<sub>10</sub> stations are analyzed. These outbreaks were selected based on concurrent  
955 fulfillment of the following criteria: (i) a DD episode must be identified by the satellite algorithm at  
956 pixel level (at  $1^\circ \times 1^\circ$  grid cell), (ii) total PM<sub>10</sub> measurement must be available at the station which lies  
957 into the geographical limits of the corresponding grid cell and (iii) CALIPSO flies across the grid cell.  
958 These criteria were met for 13 desert dust outbreaks, which took place over 9 PM<sub>10</sub> stations during the  
959 period 2000-2013. Similarities were found among the identified cases and therefore only the results for  
960 four desert dust outbreaks of different geometrical characteristics are discussed in the present section.  
961 For each case, we have produced the cross sections of the  $\beta_{532nm}$  vertical profiles up to 8 km above sea  
962 level (a.s.l.) along the CALIOP-CALIPSO track when the satellite flies near the PM<sub>10</sub> site (Figures 11-  
963 13). Moreover, the corresponding aerosol subtype profiles, acquired from the CALIOP website  
964 ([http://www-calipso.larc.nasa.gov/products/lidar/browse\\_images/production/](http://www-calipso.larc.nasa.gov/products/lidar/browse_images/production/)), are provided in the  
965 supplementary material (Figures S7-S9). Since the PM<sub>10</sub> concentrations are available only as daily  
966 averages, the optimum solution would be to have the maximum number (2) of CALIOP overpasses  
967 near PM<sub>10</sub> site throughout the day, in order to reduce the temporal inconsistencies between satellite  
968 vertical resolved retrievals and ground data. However, in 8 out of 13 desert dust outbreaks this was not  
969 feasible.

970

971 4.4.1 Case 1: Censt (26<sup>th</sup> May 2008)

972 The first study case refers to a desert dust outbreak that took place on 26<sup>th</sup> May 2008 and affected  
973 the station Censt (Lat: 39.064, Lon: 8.457) located in southern Sardinia. At the ground, the measured  
974 mean daily total PM<sub>10</sub> concentration was 19 µg m<sup>-3</sup> whereas 68% (or 13 µg m<sup>-3</sup>) of the load consisted of  
975 dust particles indicating thus their strong presence in the lowest troposphere. Based on MODIS-Terra  
976 retrievals, representative for the whole atmospheric column and grid cell, the aerosol optical depth at  
977 550 nm was equal to 0.81. In order to investigate the vertical distribution of the dust outbreak, the cross  
978 sections of the  $\beta_{532nm}$  vertical profiles along CALIOP track, near the station, during daytime and  
979 nighttime have been reproduced and depicted in Figures 11-i and 11-ii, respectively. In addition, the  
980 corresponding aerosol subtype profiles are provided in Figures S7-i and S7-ii in the supplementary  
981 material. During night, it is evident the predominance of a well-developed dust layer mixed with  
982 polluted aerosols (Figure S7-i) extending from surface up to 5 km a.s.l. between the parallels 33° N and  
983 38° N, while near the station its top is lowered down to 3 km (left side of Figure 11-i). Moreover, the  
984  $\beta_{532nm}$  values range mainly from 0.002 to 0.003 km<sup>-1</sup> sr<sup>-1</sup> without revealing remarkable variations, thus  
985 indicating a rather compact dust layer. According to the daytime CALIOP overpass (Figure 11-ii), a  
986 pure dust layer (Figure S7-ii) is confined between surface and 4 km, affecting the surrounding area of  
987 the station, while its intensity (in terms of  $\beta_{532nm}$ ) varies slightly from 0.0015 to 0.002 km<sup>-1</sup> sr<sup>-1</sup>.  
988 Nevertheless, due to the background solar illumination, leading thus to a lower signal-to-noise ratio  
989 (Nowottnick et al., 2015), the “borders” of the dust plume during daytime are not so distinct in contrast  
990 to nighttime. According to the obtained results, the ground-based measurements are able to capture  
991 satisfactorily the dust event when its load is equally distributed in the lowest tropospheric levels,  
992 resulting thus to a good agreement between MODIS and PM<sub>10</sub> observations.

993

994 4.4.2 Case 2 and 3: Els Torms (16<sup>th</sup> July 2008) and San Pablo (12<sup>th</sup> September 2007)

995 Two dust events that affected Els Torms (NE Spain, Lat: 41.395, Lon: 0.721) and San Pablo  
996 (central Spain, Lat: 39.525, Lon: -4.353) on 16<sup>th</sup> July 2008 and 12<sup>th</sup> September 2007, respectively, are  
997 studied here. The daily averages of the total PM<sub>10</sub> concentrations were equal to 16 and 30 µg m<sup>-3</sup>,  
998 respectively, whereas the dust particles' contribution (dust PM<sub>10</sub>) to the total amount was zero in Els  
999 Torms and 33 % in San Pablo. On the contrary, the MODIS-Terra level 3 AOD retrievals were high  
1000 and equal to 0.56 (Els Torms) and 0.64 (San Pablo), indicating the existence of dust aerosols according  
1001 to the satellite algorithm's classification method. In order to give a better insight, aiming at describing

1002 the discrepancies between MODIS-Terra AOD and PM<sub>10</sub> concentrations, we have reproduced the cross  
1003 sections of the total backscatter at 532 nm when CALIPSO flies, during daytime, near Els Torms  
1004 (Figure 12-i) and San Pablo (Figure 12-ii). The corresponding profiles of the CALIOP aerosol  
1005 classification scheme are also available in Figures S8-i and S8-ii. In Els Torms, where the dust PM<sub>10</sub>  
1006 concentration was zero, a dust layer (Figure S8-i) with its base at 3.5 km a.s.l. and its top at 5 km a.s.l.,  
1007 is recorded by the CALIOP lidar between the parallels 41° N and 43° N. The intensity of the elevated  
1008 dust layer, in terms of  $\beta_{532nm}$ , varies from 0.002 to 0.004 km<sup>-1</sup> sr<sup>-1</sup> (Figure 12-i). Through CALIOP lidar  
1009 profiles, it is confirmed the existence of a dust layer aloft, which cannot be captured by the PM<sub>10</sub>  
1010 measurements in contrast to the MODIS spectroradiometer. In San Pablo, where the dust particles'  
1011 contribution to the total PM<sub>10</sub> load was equal to 33 %, a dust layer abuts the ground extending up to 5-6  
1012 km ASL, whereas the dust plume covers a wide range, in latitudinal terms, from the sub-Sahel to the  
1013 Celtic Sea, affecting the Iberian Peninsula (Figure S8-ii). Nevertheless, the intensity of the dust layer,  
1014 over the surrounding area of the station, differs with altitude being higher between 2.5 and 5 km a.s.l.  
1015 (0.004 to 0.007 km<sup>-1</sup> sr<sup>-1</sup>) and lower between ground and 2 km a.s.l. (<0.003 km<sup>-1</sup> sr<sup>-1</sup>), as it is depicted  
1016 in the middle of Figure 12-ii. The two studied cases here differ from Case 1 (Section 4.4.1) either with  
1017 regards to the position of the elevated dust layer (Els Torms) or to its vertical distribution (San Pablo),  
1018 which explains the poor agreement between satellite columnar AOD retrievals (MODIS) and ground  
1019 PM<sub>10</sub> concentrations.

1020

#### 1021 4.4.3 Case 4: Agia Marina (25<sup>th</sup> February 2007)

1022

1023 The case studied here, namely the desert dust outbreak recorded in Agia Marina (Cyprus, Lat:  
1024 35.039, Lon: 33.058) on 25<sup>th</sup> February 2007, is the strongest one among the selected cases. More  
1025 specifically, the daily average of the dust PM<sub>10</sub> concentration was equal to 134 µg m<sup>-3</sup> accounting for  
1026 the 92 % of the total PM<sub>10</sub> measured amount at the station, which is indicative of the strong  
1027 predominance of dust particles in the lowest troposphere. The MODIS-Terra level 3 AOD value for the  
1028 grid cell to which the station it is found, is high and equal to 1.04. According to the CALIOP aerosol  
1029 classification scheme, during nighttime, a shallow low-elevated dust layer mixed with polluted or  
1030 marine aerosols is heading towards the station, whereas above the PM<sub>10</sub> site (Agia Marina) extends  
1031 from close to the ground up to 9 km a.s.l., comprising only pure dust aerosols (Figure S9). The main  
1032 part of the dust layer, in the surrounding area of the station, is confined between 2.5 and 4 km a.s.l.

1033 where the maximum  $\beta_{532nm}$  values (up to  $0.006 \text{ km}^{-1} \text{ sr}^{-1}$ ) are observed (Figure 13). Also, similar  $\beta_{532nm}$   
1034 values are recorded below 1 km a.s.l.; however, the dust layer is not well represented in the cross  
1035 section of the CALIOP  $\beta_{532nm}$  vertical profiles due to the total attenuation of the lidar beam by clouds  
1036 (located between 3 and 4 km a.s.l.) superimposed to the low-elevated dust layer.

1037

## 1038 **5. Summary and conclusions**

1039 This study aims at describing the vertical structure of intense desert dust outbreaks affecting the  
1040 broader Mediterranean basin. To achieve this target, an updated version of an objective and dynamic  
1041 algorithm, which has been introduced by Gkikas et al. (2009; 2013), has been applied for the  
1042 identification of strong and extreme desert dust episodes, over the period Mar. 2000 – Feb. 2013. For  
1043 its operation, a group of optical properties, retrieved by satellite sensors (MODIS-Terra/Aqua, EP-  
1044 TOMS and OMI-Aura) on a daily basis, is used, providing information about aerosols' load, size and  
1045 nature. Briefly, the satellite algorithm consists of three parts; at the first one are computed the mean  
1046 *AOD* value (*Mean*) and the associated standard deviation (*Std*) for the whole study period in each grid  
1047 cell of  $1^\circ \times 1^\circ$  spatial resolution, at the second one the identified aerosol episodes are classified based  
1048 on their intensity to strong and extreme ones. Finally, at the third part the identified aerosol episodes  
1049 are categorized as desert dust episodes, separately over land and sea. Through this approach the  
1050 selected dataset consists only of intense desert dust episodes since their intensity (expressed in terms of  
1051  $AOD_{550nm}$ ) is higher/equal than  $Mean + 2*Std$ . The DD episodes have also been determined by  
1052 applying an alternative second methodology (METHOD-B) which excludes dust-affected cases  
1053 identified based on the criteria set concerning the aerosol size related optical properties.

1054 Based on the satellite algorithm's outputs, an overall view about the regime of Mediterranean desert  
1055 dust outbreaks is presented for the periods Mar. 2000 – Feb. 2013 (MODIS-Terra) and 2003-2012  
1056 (MODIS-Aqua). The main findings concerning the intense DD episodes' frequency (in terms of  
1057 episodes  $\text{yr}^{-1}$ ) and intensity (in terms of *AOD* at 550nm) are the following:

1058 ➤ Strong DD episodes occur more frequently (up to  $9.9 \text{ episodes yr}^{-1}$ ) in the western  
1059 Mediterranean while the extreme ones occur more frequently (up to  $3.3 \text{ episodes yr}^{-1}$ ) over the  
1060 central parts of the Mediterranean Sea, when the satellite algorithm operates with MODIS-Terra  
1061 retrievals.

- 1062 ➤ The intensity of strong and extreme DD episodes, in AOD terms, can reach to 1.5 and 3-4,  
1063 respectively, over the central and eastern parts of the Mediterranean Sea, near off the northern  
1064 African coasts.
- 1065 ➤ Slightly lower frequencies and higher intensities are found for the period 2003-2012, when the  
1066 satellite algorithm operates with MODIS-Aqua retrievals.
- 1067 ➤ Through the intercomparison between the two applied methodologies, it is revealed that the  
1068 geographical patterns of frequency of occurrence are similar both for strong and extreme DD  
1069 episodes; however, higher frequencies are found based on METHOD-B.
- 1070 ➤ Based on METHOD-B, the DD episodes' intensities are decreased whereas the geographical  
1071 patterns for the strong DD episodes are not so distinct compared to the corresponding results  
1072 obtained by the default version of the satellite algorithm.
- 1073 ➤ The similarity between the outputs of the algorithm using the two methodologies shows the  
1074 consistency of the algorithm and the validity of its concept.

1075 Through the comparison of the satellite algorithm against surface measurements derived from 109  
1076 AERONET and 22 PM<sub>10</sub> stations, it is found that:

1077 AERONET

- 1078 ➤ The correlation coefficient between MODIS and AERONET AODs is increased from 0.505 to  
1079 0.750 when level 3 grid cells with higher sub-grid spatial representativeness and homogeneity  
1080 are considered.
- 1081 ➤ According to the AERONET volume size distributions, it is evident the predominance of the  
1082 coarse mode with a peak ( $\sim 0.25 \mu\text{m}^3 \mu\text{m}^{-2}$ ) for particles radii between 1.70 and 2.24  $\mu\text{m}$ , in  
1083 case of intense DD episodes.
- 1084 ➤ The appropriateness of DD episodes' identification method applied to the satellite algorithm is  
1085 confirmed since the majority (>75%) of AERONET  $\alpha_{440-870\text{nm}}$  and  $r_{\text{eff}}$  values are lower than 0.54  
1086 and higher than 0.55  $\mu\text{m}$ , respectively.
- 1087 ➤ About 15% of the pixel level intense DD episodes are misclassified by the satellite algorithm  
1088 and these drawbacks are encountered in AERONET stations where the aerosol load is  
1089 dominated either by fine particles or by complex aerosol types.

1090 PM<sub>10</sub> and dust contribution

- 1091 ➤ The agreement between surface and satellite measurements is better over the central and eastern  
 1092 Mediterranean stations.
- 1093 ➤ On a station level, the percentage of the intense DD episodes, for which a dust contribution to  
 1094 PM<sub>10</sub> surface concentration has been recorded, varies from 68% (Monagrega, northeastern  
 1095 Spain) to 97% (Bocadifalco, Sicily).
- 1096 ➤ In the majority of stations, dust particles contribute more than 50% of the total amount reaching  
 1097 up to 86.8% (Ayia Marina, Cyprus).
- 1098 ➤ The mean PM<sub>10</sub> concentration levels mainly vary from 20 to 50 µg m<sup>-3</sup> reaching up to 223 µg m<sup>-3</sup>  
 1099 in Ayia Marina (Cyprus).

1100 In order to describe the vertical structure of the intense Mediterranean dust outbreaks, the CALIOP  
 1101 vertical profiles of aerosol subtyping and total backscatter coefficient at 532 nm, are used as a  
 1102 complementary tool to the identified intense DD episodes by the satellite algorithm. Through this  
 1103 synergistic approach it is found that:

- 1104 ➤ Dust particles are mainly detected between 0.5 and 6 km, following an ascending mode, up to  
 1105 40° N, leaving from the source areas and transported towards the Mediterranean.
- 1106 ➤ Over the western Mediterranean, the dust layers are mainly observed between 2 and 6 km while  
 1107 their base height is decreased down to 0.5 km for increasing longitudes.
- 1108 ➤ During the warm period of the year, dust particles are uplifted at higher altitudes (up to 8 km).
- 1109 ➤ In summer, the transported dust loads over the western Mediterranean are recorded above 1 km  
 1110 and in spring at lower altitudes over the central and eastern parts of the study region. This  
 1111 behavior underlies the role of topography (e.g. Atlas Mountains) and the enhanced thermal  
 1112 convection.
- 1113 ➤ The intensity of dust outbreaks, in terms of  $\beta_{532nm}$ , is maximized (up to 0.006 km<sup>-1</sup> sr<sup>-1</sup>) below 2  
 1114 km and at the southern parts (30° N - 34° N) of the study region.
- 1115 ➤ In spring, considerably high  $\beta_{532nm}$  values (~ 0.004 km<sup>-1</sup> sr<sup>-1</sup>) are observed between 2 and 4 km  
 1116 in the latitudinal zone extending from 35° N to 42° N.
- 1117 ➤ Moderate-to-high  $\beta_{532nm}$  values are observed up to 6 km, near to the source areas, while the top  
 1118 of dust layers is gradually decreased down to 4 km towards northern latitudes.
- 1119 ➤ From the longitudinal projection of  $\beta_{532nm}$ , it is evident that DD episodes are more intense (~  
 1120 0.004 km<sup>-1</sup> sr<sup>-1</sup>) between 1 and 5 km in the western Mediterranean, while over the central and  
 1121 eastern sectors, the maximum intensities (~ 0.006 km<sup>-1</sup> sr<sup>-1</sup>) are recorded below 1.5 km.

1122 ➤ On a seasonal basis, DD episodes are found to be more intense (up to  $0.018 \text{ km}^{-1} \text{ sr}^{-1}$ ) in spring,  
1123 when dust is transported towards the central and eastern parts of the Mediterranean region.

1124 At the last part of the present study, it is investigated how the desert dust outbreaks' vertical  
1125 distribution can affect the level of agreement between columnar satellite AOD retrievals (MODIS) and  
1126 ground  $\text{PM}_{10}$  concentrations. For this purpose four intense Mediterranean desert dust outbreaks of  
1127 different geometrical characteristics that took place across the Mediterranean, namely in Spain  
1128 (western), Sardinia (central) and Cyprus (eastern), are studied when satellite algorithm's outputs,  
1129 ground  $\text{PM}_{10}$  concentrations and CALIOP-CALIPSO lidar profiles are available concurrently. Our  
1130 analysis clearly shows that when a well-developed and compact dust layer is located in the lowest  
1131 tropospheric levels, then the level of agreement between MODIS- $\text{PM}_{10}$  is high. On the contrary, when  
1132 the dust layer is aloft or its load is not equally distributed in vertical terms then a poor agreement  
1133 between MODIS- $\text{PM}_{10}$  is found.

1134 This study attempts to highlight the importance of the synergistic use of satellite observations and  
1135 the usage of surface-based measurements, targeting to the representation of the 3D structure of dust  
1136 outbreaks and the description of their spatial and temporal features. For this reason, the further  
1137 development of the satellite algorithm is an ongoing process by our group, aiming at extending the  
1138 study domain from regional to global scale, considering the latest version of MODIS retrievals  
1139 (Collection 006) as well as the Deep Blue Algorithm retrievals, available over the major dust sources of  
1140 the planet.

1141

## 1142 **Acknowledgements**

1143 The MDRAF project has received funding from the European Union's Seventh Framework  
1144 Programme for research, technological development and demonstration under grant agreement no  
1145 622662. The Collection 051 MODIS-Terra and MODIS-Aqua data were obtained from NASA's Level  
1146 1 and Atmosphere Archive and Distribution System (LAADS) website  
1147 (<ftp://ladsweb.nascom.nasa.gov/>). The Earth Probe (TOMS) and OMI aerosol climatology is available  
1148 from the Mirador ftp server (<http://mirador.gsfc.nasa.gov/>). The CALIPSO retrievals have been derived  
1149 from NASA's Earth Observing System Data and Information System (<http://reverb.echo.nasa.gov/>).  
1150 We would like to thank the principal investigators maintaining the AERONET sites used in the present  
1151 work. We would like to acknowledge the EMEP Programme and the public European databases  
1152 Airbase and ACTRIS, which supplied  $\text{PM}_{10}$  data used in this study. J. Pey benefits from a Ramón y

1153 Cajal Research Grant (RYC-2013-14159) from the Spanish Ministry of Economy and Competitiveness.  
1154 S. Basart, O. Jorba, S. Gassó and J.M. Baldasano acknowledge the CICYT project CGL2013-46736  
1155 and Severo Ochoa (SEV-996 2011-00067) programme of the Spanish Government. The publication  
1156 was supported by the European Union Seventh Framework Programme (FP-7-REGPOT-2012-2013-1),  
1157 in the framework of the project BEYOND, under Grant Agreement No. 316210 (BEYOND – Building  
1158 Capacity for a Centre of Excellence for EO-based monitoring of Natural Disasters. The figures 11, 12  
1159 and 13 have been produced with ccplot (<http://ccplot.org/>). This work is contributing to the Chemistry-  
1160 Aerosol Mediterranean Experiment (ChArMEx) coordinated effort for the long-term Mediterranean  
1161 aerosol characterization using available remote sensing datasets.

1162

## 1163 **References**

1164 Adams, A. M., Prospero, J. M., and Zhang, C.: CALIPSO-derived three-dimensional structure of  
1165 aerosol over the Atlantic Basin and adjacent continents, *J. Climate*, 25, 6862–6879, doi:10.1175/JCLI-  
1166 D-11-00672.1, 2012.

1167 Alados-Arboledas, A., Alcántara, A., Olmo, F. J., Martínez-Lozano, J. A., Estellés, V., Cachorro, V.,  
1168 Silva, A. M., Horvath, H., Gangl, A., Díaz, A., Pujadas, M., Lorente, J., Labajo, A., Sorribas, M., and  
1169 Pavese, G.: Aerosol columnar properties retrieved from Cimel radiometers during VELETA 2002,  
1170 *Atmos. Environ.*, 42, 2630–2642, [doi:10.1016/j.atmosenv.2007.10.006](https://doi.org/10.1016/j.atmosenv.2007.10.006), 2008.

1171 Alam, K., Trautmann, T., Blaschke, T., Subhan, F.: Changes in aerosol optical properties due to dust  
1172 storms in the Middle East and Southwest Asia. *Remote Sens. Environ.* 143, 216–227, 2014.

1173 Alpert, P., Kishcha, P., Shtivelman, A., Krichak, S.O., Joseph, J.H.: Vertical distribution of Saharan  
1174 dust based on 2.5-year model predictions, *Atmos. Res.*, 70, 109-130, 2004.

1175 Amiridis, V., Kafatos, M., Pérez, C., Kazadzis, S., Gerasopoulos, E., Mamouri, R. E., Papayannis, A.,  
1176 Kokkalis, P., Giannakaki, E., Basart, S., Daglis, I., and Zerefos, C.: The potential of the synergistic use  
1177 of passive and active remote sensing measurements for the validation of a regional dust model, *Ann.*  
1178 *Geophys.*, 27, 3155-3164, doi:10.5194/angeo-27-3155-2009, 2009.

1179 Amiridis, V., Wandinger, U., Marinou, E., Giannakaki, E., Tsekeri, A., Basart, S., Kazadzis, S.,  
1180 Gkikas, A., Taylor, M., Baldasano, J. M., and Ansmann, A.: Optimizing CALIPSO Saharan dust  
1181 retrievals, *Atmos. Chem. Phys.*, 13, 12089-12106, doi:10.5194/acp-13-12089-2013, 2013.

1182 Ångström, A.K.: On the atmospheric transmission of sun radiation and on the dust in the air, *Geogr.*  
1183 *Ann.*, 12, 130-159, 1929.

1184 Balis, D., Amiridis, V., Kazadzis, S., Papayannis, A., Tsaknakis, G., Tzortzakis, S., Kalivitis, N.,  
1185 Vrekoussis, M., Kanakidou, M., Mihalopoulos, N., Chourdakis, G., Nickovic, S., Pérez, C.,  
1186 Baldasano, J. M., and Drakakis, M.: Optical characteristics of desert dust over the East Mediterranean  
1187 during summer: a case study, *Ann. Geophys.*, 24, 807-821, doi:10.5194/angeo-24-807-2006, 2006.

1188 Balis, D.: Geometrical characteristics of desert dust layers over Thessaloniki estimated with  
1189 backscatter/Raman lidar and the BSC/DREAM model, *Remote Sensing Letters*, 353-362, doi:  
1190 10.1080/01431161.2011.597793, 2012.

1191 Barkan, J., Alpert, P., Kutiel, H., and Kishcha, P.: Synoptics of dust transportation days from Africa  
1192 toward Italy and central Europe, *J. Geophys. Res.*, 110, D07208, doi:10.1029/2004JD005222, 2005.

1193 Barnaba, F. and Gobbi, G. P.: Aerosol seasonal variability over the Mediterranean region and relative  
1194 impact of maritime, continental and Saharan dust particles over the basin from MODIS data in the year  
1195 2001, *Atmos. Chem. Phys.*, 4, 2367-2391, doi:10.5194/acp-4-2367-2004, 2004.

1196 Basart, S., Pérez, C., Cuevas, E., Baldasano, J. M., and Gobbi, G. P.: Aerosol characterization in  
1197 Northern Africa, Northeastern Atlantic, Mediterranean Basin and Middle East from direct-sun  
1198 AERONET observations, *Atmos. Chem. Phys.*, 9, 8265-8282, doi:10.5194/acp-9-8265-2009, 2009.

1199 Basart, S., Pay, M. T., Jorba, O., Pérez, C., Jiménez-Guerrero, P., Schulz, M., and Baldasano, J. M.:  
1200 Aerosols in the CALIOPE air quality modelling system: evaluation and analysis of PM levels, optical  
1201 depths and chemical composition over Europe, *Atmos. Chem. Phys.*, 12, 3363-3392, doi:10.5194/acp-  
1202 12-3363-2012, 2012.

1203 Ben-Ami, Y., Koren, I., and Altaratz, O.: Patterns of North African dust transport over the Atlantic:  
1204 winter vs. summer, based on CALIPSO first year data, *Atmos. Chem. Phys.*, 9, 7867-7875,  
1205 doi:10.5194/acp-9-7867-2009, 2009.

1206 Ben-Ami, Y., Koren, I., Rudich, Y., Artaxo, P., Martin, S. T., and Andreae, M. O.: Transport of North  
1207 African dust from the Bodélé depression to the Amazon Basin: a case study, *Atmos. Chem. Phys.*, 10,  
1208 7533-7544, doi:10.5194/acp-10-7533-2010, 2010.

1209 Bègue, N., Tulet, P., Chaboureau, J. P., Roberts, G., Gomes, L., and Mallet, M.: Long-range transport  
1210 of Saharan dust over north-western Europe during EUCAARI 2008 campaign: Evolution of dust  
1211 optical properties by scavenging, *J. Geophys. Res.*, 117,D17201, doi:10.1029/2012JD017611, 2012.

1212 Berthier, S., Chazette, P., Couvert, P., Pelon, J., Dulac, F., Thieuleux, F., Moulin, C., and Pain, T.:  
1213 Desert dust aerosol columnar properties over ocean and continental Africa from Lidar in-Space  
1214 Technology Experiment (LITE) and Meteosat synergy. *J. Geophys. Res.*, 111, D21202,  
1215 doi:10.1029/2005JD006999, 2006.

1216 Bollasina, M. A., Ming, Y., and Ramaswamy, V.: Anthropogenic Aerosols and the Weakening of the  
1217 South Asian Summer Monsoon, *Science*, 334, 502–505, 2011.

1218 Bösenberg, J., Matthias, V., Amodeo, A., Amoiridis, V., Ansmann, A., Baldasano, J. M., Balin, I.,  
1219 Balis, D., Böckmann, C., Boselli, A., Carlsson, G., Chaikovskiy, A., Chourdakis, G., Comerón, A., De  
1220 Tomasi, F., Eixmann, R., Freudenthaler, V., Giehl, H., Grigorov, I., Hågård, A., Iarlori, M., Kirsche,  
1221 A., Kolarov, G., Komguem, L., Kreipl, S., Kumpf, W., Larchevêque, G., Linné, H., Matthey, R.,  
1222 Mattis, I., Mekler, A., Mironova, I., Mitev, V., Mona, L., Müller, D., Music, S., Nickovic, S.,  
1223 Pandolfi, M., Papayannis, A., Pappalardo, G., Pelon, J., Pérez, C., Perrone, R. M., Persson, R.,  
1224 Resendes, D. P., Rizi, V., Rocadenbosch, F., Rodrigues, J. A., Sauvage, L., Schneidenbach, L.,  
1225 Schumacher, R., Shcherbakov, V., Simeonov, V., Sobolewski, P., Spinelli, N., Stachlewska, I.,  
1226 Stoyanov, D., Trickl, T., Tsaknakis, G., Vaughan, G., Wandinger, U., Wang, X., Wiegner, M.,  
1227 Zavrtnik, M. and Zerefos, C.: A European aerosol research lidar network to establish an aerosol  
1228 climatology, MPI-Rep. 317, Max-Planck Inst. für Meteorol., Hamburg, Germany, 2003.  
1229 [http://www.mpimet.mpg.de/fileadmin/publikationen/Reports/max\\_scirep\\_348.pdf](http://www.mpimet.mpg.de/fileadmin/publikationen/Reports/max_scirep_348.pdf)  
1230

1231 Burton, S. P., Ferrare, R. A., Vaughan, M. A., Omar, A. H., Rogers, R. R., Hostetler, C. A., and  
1232 Hair, J. W.: Aerosol classification from airborne HSRL and comparisons with the CALIPSO vertical  
1233 feature mask, *Atmos. Meas. Tech.*, 6, 1397-1412, doi:10.5194/amt-6-1397-2013, 2013.

1234

1235 Cachorro, V. E., Vergaz, R., de Frutos, A. M., Vilaplana, J. M., Henriques, D., Laulainen, N., and  
1236 Toledano, C.: Study of desert dust events over the southwestern Iberian Peninsula in year 2000: two  
1237 case studies, *Ann. Geophys.*, 24, 1493-1510, doi:10.5194/angeo-24-1493-2006, 2006.

1238

1239 Cao, C. X., Zheng, S., and Singh, R. P.: Characteristics of aerosol optical properties and meteorological  
1240 parameters during three major dust events (2005–2010) over Beijing, China, *Atmos. Res.*, 150, 129–  
1241 142, [doi:10.1016/j.atmosres.2014.07.022](https://doi.org/10.1016/j.atmosres.2014.07.022), 2014.

1242

1243 Córdoba-Jabonero, C., Sorribas, M., Guerrero-Rascado, J. L., Adame, J. A., Hernández, Y.,  
1244 Lyamani, H., Cachorro, V., Gil, M., Alados-Arboledas, L., Cuevas, E., and de la Morena, B.:  
1245 Synergetic monitoring of Saharan dust plumes and potential impact on surface: a case study of dust  
1246 transport from Canary Islands to Iberian Peninsula, *Atmos. Chem. Phys.*, 11, 3067-3091,  
1247 [doi:10.5194/acp-11-3067-2011](https://doi.org/10.5194/acp-11-3067-2011), 2011.

1248

1249 Di Sarra, A., Di Iorio, T., Cacciani, M., Fiocco, G., and Fuà, D.: Saharan dust profiles measured by  
1250 lidar at Lampedusa, *J. Geophys. Res.*, 106, 10 335–10 348, 2001.

1251

1252 Díaz, J., Tobías A., and Linares, C.: Saharan dust and association between particulate matter and case-  
1253 specific mortality: a case crossover analysis in Madrid (Spain), *Environ. Health*, [doi:10.1186/1476-](https://doi.org/10.1186/1476-069X-11-11)  
1254 [069X-11-11](https://doi.org/10.1186/1476-069X-11-11), 2012.

1255

1256 Draxler, R.R. and Rolph, G.D., 2015. HYSPLIT (HYbrid Single-Particle Lagrangian Integrated  
1257 Trajectory) Model access via NOAA ARL READY Website (<http://ready.arl.noaa.gov/HYSPLIT.php>).  
1258 NOAA Air Resources Laboratory, Silver Spring, MD.

1259

1260 Dubovik, O., Smirnov, A., Holben, B. N., King, M. D., Kaufman, Y. J., and Slutsker, I.: Accuracy  
1261 assessments of aerosol optical properties retrieved from AERONET sun and sky radiance  
1262 measurements, *J. Geophys. Res.*, 105, 9791–9806, 2000.

1263

1264 Dubovik, O. and King, M. D.: A flexible inversion algorithm for retrieval of aerosol optical properties  
1265 from Sun and sky radiance measurements, *J. Geophys. Res.*, 105, 20673-20696, 2000.

1266

1267 Dulac, F., Moulin, C., Lambert, C.E., Guillard, F., Poitou, J., Guelle, W., Quetel, C.R., Schneider, X.,  
1268 Ezat, U., and Buat-Ménard, P.: Dry deposition of mineral aerosol particles in the atmosphere:  
1269 Significance of the large size fraction, in *Precipitation Scavenging and Atmosphere-Surface Exchange*,  
1270 edited by S. E. Schwartz and W.G. N. Slinn, pp. 841-854, Hemisphere. Richland, Wash., 1992.

1271

1272 Eck, T. F., Holben, B. N., Reid, J. S., Dubovik, O., Smirnov, A., O'Neill, N. T., Slutsker, I., and Kinne,  
1273 S.: Wavelength dependence of optical depth of biomass burning, urban and desert dust aerosols, *J.*  
1274 *Geophys. Res.*, 104, 31333–31350, 1999.

1275

1276 Eguchi, K., Uno, I., Yumimoto, K., Takemura, T., Shimizu, A., Sugimoto, N., and Liu, Z.: Trans-  
1277 pacific dust transport: integrated analysis of NASA/CALIPSO and a global aerosol transport model,  
1278 *Atmos. Chem. Phys.*, 9, 3137-3145, doi:10.5194/acp-9-3137-2009, 2009.

1279

1280 Escudero, M., Querol, X., Pey, J., Alastuey, A., Pérez, N., Ferreira, F., Alonso, S., Rodríguez, S., and  
1281 Cuevas, E.: A methodology for the quantification of the net African dust load in air quality monitoring  
1282 networks, *Atmos. Environ.*, 41, 5516–5524, 2007.

1283

1284 Fotiadi, A., Hatzianastassiou, N., Drakakis, E., Matsoukas, C., Pavlakakis, K.G., Hatzidimitriou, D.,  
1285 Gerasopoulos, E., Mihalopoulos, N., and Vardavas, I.: Aerosol physical and optical properties in the  
1286 Eastern Mediterranean Basin, Crete, from Aerosol Robotic Network data, *Atmos. Chem. Phys.*, 6,  
1287 5399–5413, doi:10.5194/acp-6-5399-2006, 2006.

1288

1289 Ginoux, P., Prospero, J. M., Gill, T. E., Hsu, N. C., and Zhao, M.: Global-scale attribution of  
1290 anthropogenic and natural dust sources and their emission rates based on MODIS Deep Blue aerosol  
1291 products, *Rev. Geophys.*, 50, RG3005, doi:10.1029/2012rg000388, 2012.

1292

1293 Gkikas, A., Hatzianastassiou, N., and Mihalopoulos, N.: Aerosol events in the broader Mediterranean  
1294 basin based on 7-year (2000–2007) MODIS C005 data, *Ann. Geophys.*, 27, 3509-3522,  
1295 doi:10.5194/angeo-27-3509-2009, 2009.

1296

1297 Gkikas, A., Hatzianastassiou, N., Mihalopoulos, N., Katsoulis, V., Kazadzis, S., Pey, J., Querol, X.,  
1298 and Torres, O.: The regime of intense desert dust episodes in the Mediterranean based on contemporary  
1299 satellite observations and ground measurements, *Atmos. Chem. Phys.*, 13, 12135-12154,  
1300 doi:10.5194/acp-13-12135-2013, 2013.

1301 Gkikas, A., Houssos, E. E., Lolis, C. J., Bartzokas, A., Mihalopoulos, N. and Hatzianastassiou, N.:  
1302 Atmospheric circulation evolution related to desert-dust episodes over the Mediterranean. *Q.J.R.*  
1303 *Meteorol. Soc.*, 141: 1634–1645. doi: 10.1002/qj.2466, 2015.

1304 Gkikas, A., Houssos, E. E., Lolis, C. J., Bartzokas, A., Mihalopoulos, N. and Hatzianastassiou, N.:  
1305 Atmospheric circulation evolution related to desert-dust episodes over the Mediterranean. *Q.J.R.*  
1306 *Meteorol. Soc.*, doi: 10.1002/qj.2466, 2014.

1307 Gobbi, G.P., Barnaba, F., Giorgi, R., Santacasa, A.: Altitude-resolved properties of a Saharan dust  
1308 event over the Mediterranean, *Atmos. Environ.*, 34, 5119-5127, 2000.

1309 Gobbi, G. P., Kaufman, Y. J., Koren, I., and Eck, T. F.: Classification of aerosol properties derived  
1310 from AERONET direct sun data, *Atmos. Chem. Phys.*, 7, 453-458, doi:10.5194/acp-7-453-2007, 2007.

1311 Gobbi, G. P., Angelini, F., Barnaba, F., Costabile, F., Baldasano, J. M., Basart, S., Sozzi, R., and  
1312 Bolignano, A.: Changes in particulate matter physical properties during Saharan advections over Rome  
1313 (Italy): a four-year study, 2001–2004, *Atmos. Chem. Phys.*, 13, 7395–7404, doi:10.5194/acp-13-7395-  
1314 2013, 2013.

1315 Hamonou, E., Chazette, P., Balis, D., Dulac, F., Schneider, X., Galani, E., Ancellet, G., and  
1316 Papayannis, A.: Characterization of the vertical structure of Saharan dust export to the Mediterranean  
1317 basin, *J. Geophys. Res.*, 104, 22 257–22 270, 1999.

1318 Hara, Y., Yumimoto, K., Uno, I., Shimizu, A., Sugimoto, N., Liu, Z., and Winker, D. M.: Asian dust  
1319 outflow in the PBL and free atmosphere retrieved by NASA CALIPSO and an assimilated dust  
1320 transport model, *Atmos. Chem. Phys.*, 9, 1227-1239, doi:10.5194/acp-9-1227-2009, 2009.

1321 Hatzianastassiou, N., Gkikas, A., Mihalopoulos, N., Torres, O., and Katsoulis, B. D.: Natural versus  
1322 anthropogenic aerosols in the eastern Mediterranean basin derived from multiyear TOMS and MODIS  
1323 satellite data, *J. Geophys. Res.*, 114, D24202, doi:10.1029/2009JD011982, 2009.

1324 Heinold, B., Helmert, J., Hellmuth, O., Wolke, R., Ansmann, A., Marticorena, B., Laurent, B. and  
1325 Tegen, I.: Regional modeling of Saharan dust events using LM-MUSCAT: Model description and case  
1326 studies, *J. Geophys. Res.*, 112, D11204, doi:10.1029/2006JD007443, 2007.

1327 Heinold, B., Tegen, I., Schepanski, K., and Hellmuth, O.: Dust Radiative feedback on Saharan  
1328 boundary layer dynamics and dust mobilization. *Geophys. Res. Lett.*, 35, L20817,  
1329 doi:10.1029/2008GL035319, 2008.

1330 Herman, J. R., Bhartia, P. K., Torres, O., Hsu, N.C., Sefstor, C. J., and Celarier E.: Global distribution of  
1331 UV-absorbing aerosols from Nimbus-7/ TOMS data, *J. Geophys. Res.*, 102, 16911– 16923, 1997.

1332 Holben, B. N., Eck, T. F., Slutsker, I., Tanré, D., Buis, J. P., Setzer, A., Vermote, E., Reagan, J. A.,  
1333 Kaufman, Y. J., Nakajima, T., Lavenu, F., Jankowiak, I., and Smirnov, A.: AERONET – A federated  
1334 instrument network and data archive for aerosol characterization, *Remote Sens. Environ.*, 66, 1–16,  
1335 1998.

1336 Huang, J., Minnis, P., Lin, B., Wang, T., Yi, Y., Hu, Y., Sun-Mack, S. and Ayers, K.: Possible influences  
1337 of Asian dust aerosols on cloud properties and radiative forcing observed from MODIS and CERES,  
1338 *Geophys. Res. Lett.*, 33, L06824, doi:[10.1029/2005GL024724](https://doi.org/10.1029/2005GL024724), 2006.

1339 Huang, J., Zhang, C., and Prospero, J. M.: African dust outbreaks: a satellite perspective of temporal  
1340 and spatial variability over the tropical Atlantic Ocean, *J. Geophys. Res.*, 115, D05202,  
1341 doi:[10.1029/2009JD012516](https://doi.org/10.1029/2009JD012516), 2010.

1342 Hubanks, P. A., King, M. D., Platnick, S. A., and Pincus, R. A.: MODIS Atmosphere L3 Gridded  
1343 Product Algorithm Theoretical Basis Document, MODIS Algorithm Theoretical Basis Document No.  
1344 ATBD-MOD-30 for Level-3 Global Gridded Atmosphere Products (08 D3, 08 E3, 08M3), online:  
1345 [http://modis-atmos.gsfc.nasa.gov/docs/L3 ATBD 2008 12 04.pdf](http://modis-atmos.gsfc.nasa.gov/docs/L3%20ATBD%202008%2012%2004.pdf), 2008.

1346 Hunt, W. H, Winker, D. M., Vaughan, M. A., Powell, K. A., Lucker, P. L., and Weimer, C.: CALIPSO  
1347 Lidar Description and Performance Assessment, *J. Atmos. Oceanic Technol.*, 26, 1214–1228,  
1348 doi:[10.1175/2009JTECHA1223.1](https://doi.org/10.1175/2009JTECHA1223.1), 2009.

1349 IPCC, 2013: Summary for Policymakers. In: *Climate Change 2013: The Physical Science Basis.*  
1350 *Contribution of Working Group I to the Fifth Assessment Report of the Intergovernmental Panel on*  
1351 *Climate Change* [Stocker, T.F., D. Qin, G.-K. Plattner, M. Tignor, S. K. Allen, J. Boschung, A. Nauels,  
1352 Y. Xia, V. Bex and P.M. Midgley (eds.)]. Cambridge University Press, Cambridge, United Kingdom  
1353 and New York, NY, USA.

1354 Kalivitis, N., Gerasopoulos, E., Vrekoussis, M., Kouvarakis, G., Kubilay, N., Hatzianastassiou, N.,  
1355 Vardavas, I., and Mihalopoulos, N.: Dust transport over the eastern Mediterranean derived from  
1356 TOMS, AERONET and surface measurements, *J. Geophys. Res.*, 112, D03202,  
1357 doi:[10.1029/2006JD007510](https://doi.org/10.1029/2006JD007510), 2007.

1358 Karanasiou, A., Moreno, N., Moreno, T., Viana, M., de Leeuw, F., Querol, X.: Health effects from  
1359 Sahara dust episodes in Europe: literature review and research gaps, *Environ. Int.*, 15, 107–  
1360 114,doi:10.1016/j.envint.2012.06.012, 2012.

1361 Karyampudi, V. M., Palm, S. P., Reagen, J. A., Fang, H., Grant, W. B., Hoff, R. M., Moulin, C.,  
1362 Pierce, H. F., Torres, O., Browell, E. V., and Melfi, S. H.: Validation of the Saharan dust plume  
1363 conceptual model using lidar, *Meteosat and ECMWF*, *B. Am. Meteorol. Soc.*, 80, 1045–1075, 1999.

1364 Kaufman, Y. J., Tanré, D., Remer, L. A., Vermote, E. F., Chu, A., and Holben, B. N.: Operational  
1365 remote sensing of tropospheric aerosol over land from EOS Moderate-resolution Imaging  
1366 Spectroradiometer, *J. Geophys. Res.*, 102, 17051–17065, 1997.

1367 Kaufman, Y. J., Smirnov, A., Holben, B. N., and Dubovik, O.: Baseline maritime aerosol: methodology  
1368 to derive the optical thickness and the scattering properties, *Geophys. Res. Lett.*, 28, 3251– 3254, 2001.

1369 Kaufman, Y. J., Tanre, D., Holben, B. N., Mattoo, S., Remer, L. A., Eck, T. F., Vaughan, J., and  
1370 Chatenet, B.: Aerosol radiative impact on spectral solar flux at the surface, derived from principal-  
1371 plane sky measurements, *J. Atmos. Sci.*, 59, 635–646, 2002.

1372 Kazadzis, S., Bais, A., Amiridis, V., Balis, D., Meleti, C., Kouremeti, N., Zerefos, C. S.,  
1373 Rapsomanikis, S., Petrakakis, M., Kelesis, A., Tzoumaka, P., and Kelektoglou, K.: Nine years of UV  
1374 aerosol optical depth measurements at Thessaloniki, Greece, *Atmos. Chem. Phys.*, 7, 2091-2101,  
1375 doi:10.5194/acp-7-2091-2007, 2007.

1376 Kishcha, P., Barnaba, F., Gobbi, G. P., Alpert, P., Shtivelman, A., Krichak, S. O., and Joseph, J. H.:  
1377 Vertical distribution of Saharan dust over Rome (Italy): Comparison between 3-year model predictions  
1378 and lidar soundings, *J. Geophys. Res.*, 110, D06208, doi:10.1029/2004JD005480, 2005.  
1379

1380 Klein, H., Nickovic, S., Haunold, W., Bundke, U., Nillius, B., Ebert, M., Weinbruch, S., Schuetz, L.,  
1381 Levin, Z., Barrie, L. A., and Bingemer, H.: Saharan dust and ice nuclei over Central Europe, *Atmos.*  
1382 *Chem. Phys.*, 10, 10211–10221, doi:10.5194/acp- 10-10211-2010, 2010.  
1383

1384 Kubilay, N., Cokacar, T., and Oguz, T.: Optical properties of mineral dust outbreaks over the  
1385 northeastern Mediterranean, *J. Geophys. Res.*, 108, 4666, doi:10.1029/2003JD003798, 2003.

1386 Lau, K. M., Kim, M. K., and Kim, K. M.: Asian summer monsoon anomalies induced by direct forcing:  
1387 The role of the Tibetan plateau, *Clim. Dynam.*, 26, 855–864, 2006.

1388 Levy, R. C., Remer, L. A., Tanré, D., Kaufman, Y. J., Ichoku, C., Holben, B. N., Livingston, J. M.,  
1389 Russell, P. B., and Maring, H.: Evaluation of the Moderate-Resolution Imaging Spectroradiometer  
1390 (MODIS) retrievals of dust aerosol over the ocean during PRIDE, *J. Geophys. Res.*, 108, 8594,  
1391 doi:10.1029/2002JD002460, 2003.

1392 Levy, R. C., Remer, L. A., Kleidman, R. G., Mattoo, S., Ichoku, C., Kahn, R., and Eck, T. F.: Global  
1393 evaluation of the Collection 5 MODIS dark-target aerosol products over land, *Atmos. Chem. Phys.*, 10,  
1394 10399–10420, doi:10.5194/acp-10-10399-2010, 2010.

1395 Liu, D., Wang, Z., Liu, Z., Winker, D., and Trepte, C.: A height resolved global view of dust aerosols  
1396 from the first year CALIPSO lidar measurements, *J. Geophys. Res.*, 113, D16214,  
1397 doi:10.1029/2007JD009776, 2008.

1398 Liu, Z., Vaughan, M., Winker, D., Kittaka, C., Getzewich, B., Kuehn, R., Omar, A., Powell, K., Trepte,  
1399 C., and Hostetler, C.: The CALIPSO Lidar Cloud and Aerosol Discrimination: Version 2 Algorithm  
1400 and Initial Assessment of Performance, *J. Atmos. Ocean. Tech.*, 26, 1198–1213,  
1401 doi:10.1175/2009jtecha1229.1, 2009.

1402 Luo, T., Wang, Z., Zhang, D., Liu, X., Wang, Y., and Yuan, R.: Global dust distribution from improved  
1403 thin dust layer detection using A-train satellite lidar observations, *Geophys. Res. Lett.*, 42,  
1404 doi:10.1002/2014GL062111, 2015.

1405 Lyamani, H., Olmo, F. J., and Alados-Arboledas, L.: Saharan dust outbreak over southeastern Spain as  
1406 detected by sun photometer, *Atmos. Environ.*, 39, 7276–7284, 2005.

1407 Mallet, M., Tulet, P., Serça, D., Solmon, F., Dubovik, O., Pelon, J., Pont, V., and Thouron, O.: Impact  
1408 of dust aerosols on the radiative budget, surface heat fluxes, heating rate profiles and convective  
1409 activity over West Africa during March 2006, *Atmos. Chem. Phys.*, 9, 7143-7160, doi:10.5194/acp-9-  
1410 7143-2009, 2009.

1411 Mallet, M., Dubovik, O., Nabat, P., Dulac, F., Kahn, R., Sciare, J., Paronis, D., and Léon, J. F.:  
1412 Absorption properties of Mediterranean aerosols obtained from multi-year ground-based remote  
1413 sensing observations, *Atmos. Chem. Phys.*, 13, 9195-9210, doi:10.5194/acp-13-9195-2013, 2013.

1414 Marriotti, A., Struglia, M.V., Zeng, N., Lau, K.-M.: The Hydrological Cycle in the Mediterranean  
1415 Region and Implications for the Water Budget of the Mediterranean Sea, *J. Clim.*, 15, 1674-1690,  
1416 2002.

1417 Matthias, V., Balis, D., Bösenberg, J., Eixmann, R., Iarlori, M., Komguem, L., Mattis, I., Papayannis,  
1418 A., Pappalardo, G., Perrone, M. R., and Wang, X.: Vertical aerosol distribution over Europe: Statistical  
1419 analysis of Raman lidar data from 10 European Aerosol Research Lidar Network (EARLINET)  
1420 stations, 109, D18201, doi:10.1029/2004JD004638, 2004.

1421 McGrath-Spangler, E. L. and Denning, A. S.: Global Seasonal Variations of Midday Planetary  
1422 Boundary Layer Depth from CALIPSO Space-borne LIDAR, *J. Geophys. Res. Atmos.*, 118, 1226–  
1423 1233, 2013.

1424 Mehta, A. V. and Yang, S.: Precipitation climatology over Mediterranean Basin from ten years of  
1425 TRMM measurements, *Adv. Geosci.*, 17, 87-91, doi:10.5194/adgeo-17-87-2008, 2008.

1426 Meloni, D., di Sarra, A., Biavati, G., DeLuisi, J. J., Monteleone, F., Pace, G., Piacentino, S., and  
1427 Sferlazzo, D. M.: Seasonal behavior of Saharan dust events at the Mediterranean island of Lampedusa  
1428 in the period 1999–2005, *Atmos. Environ.*, 41, 3041–3056, doi:10.1016/j.atmosenv.2006.12.001, 2007.  
1429

1430 Meloni, D., di Sarra, A., Monteleone, F., Pace, G., Piacentino, S., and Sferlazzo, D. M.: Seasonal  
1431 transport patterns of intense Saharan dust events at the Mediterranean island of Lampedusa, *Atmos.*  
1432 *Res.*, 88, 134–148, doi:10.1016/j.atmosres.2007.10.007, 2008.

1433 Middleton, N. J. and Goudie, A. S.: Saharan dust: sources and trajectories, *Transactions of the Institute*  
1434 *of British Geographers*, 26, 165–181, 2001.

1435 Mielonen, T., Arola, A., Komppula, M., Kukkonen, J., Koskinen, J., de Leeuw, G., and Lehtinen, K. E.  
1436 J.: Comparison of CALIOP level 2 aerosol subtypes to aerosol types derived from AERONET  
1437 inversion data, *Geophys. Res. Lett.*, 36, L18804, doi:10.1029/2009gl039609, 2009.

1438 Mona, L., Amodeo, A., Pandolfi, M. and Pappalardo, G.: Saharan dust intrusions in the Mediterranean  
1439 area: Three years of Raman lidar measurements, *J. Geophys. Res.*, 111, D16203,  
1440 doi:10.1029/2005JD006569, 2006.

1441 Mona, L., Liu, Z., Müller, D., Omar, A., Papayannis, A., Pappalardo, G., Sugimoto, N., and  
1442 Vaughan, M.: Lidar Measurements for Desert Dust Characterization: An Overview, *Advances in*  
1443 *Meteorology*, 2012, 356265, doi:10.1155/2012/356265, 2012.

1444 Mona, L., Papagiannopoulos, N., Basart, S., Baldasano, J. M., Biniotoglou, I., Cornacchia, C., and  
1445 Pappalardo, G.: EARLINET dust observations vs. BSC-DREAM8b modeled profiles: 12-year-long

1446 systematic comparison at Potenza, Italy, *Atmos. Chem. Phys.*, 14, 8781-8793, doi:10.5194/acp-14-  
1447 8781-2014, 2014.

1448 Moulin, C., Lambert, C. E., Dulac, F., and Dayan, U.: Control of atmospheric export of dust from  
1449 North Africa by the North Atlantic Oscillation, *Nature*, 387, 691–694, 1997.

1450 Moulin, C., Lambert, C., Dayan, U., Masson, V., Ramonet, M., Bousquet, P., Legrand, M., Balkanski,  
1451 Y., Guelle, W., Marticorena, B., Bergametti, G., and Dulac, F.: Satellite climatology of African dust  
1452 transport in the Mediterranean atmosphere, *J. Geophys. Res.*, 103, 13137–13144, 1998.

1453 Nabat, P., Somot, S., Mallet, M., Chiapello, I., Morcrette, J. J., Solmon, F., Szopa, S., Dulac, F.,  
1454 Collins, W., Ghan, S., Horowitz, L. W., Lamarque, J. F., Lee, Y. H., Naik, V., Nagashima, T., Shindell,  
1455 D., and Skeie, R.: A 4-D climatology (1979–2009) of the monthly tropospheric aerosol optical depth  
1456 distribution over the Mediterranean region from a comparative evaluation and blending of remote  
1457 sensing and model products, *Atmos. Meas. Tech.*, 6, 1287–1314, doi:10.5194/amt-6-1287-2013, 2013.

1458 Nowottnick, E. P., Colarco, P. R., Welton, E. J., and da Silva, A.: Use of the CALIOP vertical feature  
1459 mask for evaluating global aerosol models, *Atmos. Meas. Tech.*, 8, 3647-3669, doi:10.5194/amt-8-  
1460 3647-2015, 2015.

1461 Omar, A. H., Winker, D. M., Kittaka, C., Vaughan, M. A., Liu, Z. Y., Hu, Y. X., Treppe, C. R.,  
1462 Rogers, R. R., Ferrare, R. A., Lee, K. P., Kuehn, R. E., and Hostetler, C. A.: The CALIPSO automated  
1463 aerosol classification and lidar ratio selection algorithm, *J. Atmos. Ocean. Tech.*, 26, 1994–2014,  
1464 doi:10.1175/2009jtech1231.1, 2009.

1465 O’Neill, N. T., Eck, T. F., Smirnov, A., Holben, B. N., and Thulasiraman, S.: Spectral discrimination of  
1466 coarse and fine mode optical depth, *J. Geophys. Res.-Atmos.*, 108, 4559, doi:10.1029/2002JD002975,  
1467 2003.

1468 Pace, G., di Sarra, A., Meloni, D., Piacentino, S., and Chamard, P.: Aerosol optical properties at  
1469 Lampedusa (Central Mediterranean). 1. Influence of transport and identification of different aerosol  
1470 types, *Atmos. Chem. Phys.*, 6, 697-713, doi:10.5194/acp-6-697-2006, 2006.

1471 Papadimas, C. D., Hatzianastassiou, N., Mihalopoulos, N., Querol, X., and Vardavas, I.: Spatial and  
1472 temporal variability in aerosol properties over the Mediterranean basin based on 6-year (2000–2006)  
1473 MODIS data, *J. Geophys. Res.*, 113, D11205, doi:10.1029/2007JD009189, 2008.

1474 Papadimas, C. D., Hatzianastassiou, N., Mihalopoulos, N., Kanakidou, M., Katsoulis, B. D., and  
1475 Vardavas, I.: Assessment of the MODIS Collections C005 and C004 aerosol optical depth products  
1476 over the Mediterranean basin, *Atmos. Chem. Phys.*, 9, 2987– 2999, doi:10.5194/acp-9-2987-2009,  
1477 2009.

1478 Papayannis, A., Balis, D., Amiridis, V., Chourdakis, G., Tsaknakis, G., Zerefos, C., Castanho, A.D.A.,  
1479 Nickovic, S., Kazadzis, S., and Grabowski, J.: Measurements of Saharan dust aerosols over the Eastern  
1480 Mediterranean using elastic backscatter-Raman lidar, spectrophotometric and satellite observations in  
1481 the frame of the EARLINET project, *Atmos. Chem. Phys.*, 5, 2065–2079, doi:10.5194/acp-5-2065-  
1482 2005, 2005.

1483 Papayannis, A., Amiridis, V., Mona, L., Tsaknakis, G., Balis, D., Bösenberg, J., Chaikovski, A., De  
1484 Tomasi, F., Grigorov, I., Mattis, I., Mitev, V., Müller, D., Nickovic, S., Pérez, C., Pietruczuk, A.,  
1485 Pisani, G., Ravetta, F., Rizi, V., Sicard, M., Trickl, T., Wiegner, M., Gerding, M., Mamouri, R. E.,  
1486 D’Amico, G., and Pappalardo, G.: Systematic lidar observations of Saharan dust over Europe in the  
1487 frame of EARLINET (2000–2002), *J. Geophys. Res.*, 113, D10204, doi:10.1029/2007JD009028, 2008.

1488 Papayannis, A., Mamouri, R. E., Amiridis, V., Kazadzis, S., Pérez, C., Tsaknakis, G., Kokkalis, P., and  
1489 Baldasano, J. M.: Systematic lidar observations of Saharan dust layers over Athens, Greece in the  
1490 frame of EARLINET project (2004–2006), *Ann. Geophys.*, 27, 3611-3620, doi:10.5194/angeo-27-  
1491 3611-2009, 2009.

1492 Papayannis, A., Nicolaet, D., Kokkalis, P., Biniotoglou, I., Talianu, C., Belegante, L., Tsaknakis, G.,  
1493 Cazacu, M.M., Vetres, I., Ilic, L.: Optical, size and mass properties of mixed type aerosols in Greece  
1494 and Romania as observed by synergy of lidar and sunphotometers in combination with model  
1495 simulations: A case study, *Atmospheric Environment, Volumes: 500-501*, 277-294, 2014.

1496 Pereira, S. N., Wagner, F., and Silva, A. M.: Seven years of measurements of aerosol scattering  
1497 properties, near the surface, in the southwestern Iberia Peninsula, *Atmos. Chem. Phys.*, 11, 17-29,  
1498 doi:10.5194/acp-11-17-2011, 2011.

1499 Pérez, C., Nickovic, S., Pejanovic, G., Baldasano, J.M. and Özsoy, E.: Interactive dust-radiation  
1500 modeling: A step to improve weather forecasts, *J. Geophys. Res.*, 111, D16206,  
1501 doi:10.1029/2005JD006717, 2006.

1502 Pérez García-Pando, C., Stanton, M. C., Diggle, P. J., Trzaska, S., Miller, R. L., Perlwitz, J. P.,  
1503 Baldasano, J. M., Cuevas, E., Ceccato, P., Yaka, P., and Thomson, M. C.: Soil Dust Aerosols and Wind

1504 as Predictors of Seasonal Meningitis Incidence in Niger, *Environ. Health Perspect.*, 122, 679–686,  
1505 doi:10.1289/ehp.1306640, 2014.

1506 Pey, J., Querol, X., Alastuey, A., Forastiere, F., and Stafoggia, M.: African dust outbreaks over the  
1507 Mediterranean Basin during 2001–2011: PM10 concentrations, phenomenology and trends, and its  
1508 relation with synoptic and mesoscale meteorology, *Atmos. Chem. Phys.*, 13, 1395–1410, doi:  
1509 10.5194/acp-13-1395-2013, 2013.

1510 Pisani, G., Boselli, A., Spinelli, N., Wang, X.: Characterization of Saharan dust layers over Naples  
1511 (Italy) during 2000–2003 EARLINET project, *Atmos. Res.* 102, 286 – 299,  
1512 doi:10.1016/j.atmosres.2011.07.012, 2011.

1513 Prospero, M. J., Ginoux, P., Torres, O., Nicholson, S. E., and Gill, T. E.: Environmental  
1514 characterization of global sources of atmospheric soil dust identified with the Nimbus 7 Total Ozone  
1515 Mapping Spectrometer (TOMS) absorbing aerosol product, *Rev. Geophys.*, 40, 1002,  
1516 doi:10.1029/2000RG000095, 2002.

1517 Prospero, J. M. and Lamb, P. J.: African droughts and dust transport to the Caribbean: climate change  
1518 implications, *Science*, 302, 1024–1027, doi:10.1126/science.1089915, 2003.

1519 Querol, X., Alastuey A., Lopez-Soler A., Plana F. Puigercus J.A, Mantilla E., Miro J.V.; Artiñano B.:  
1520 Seasonal evolution of atmospheric suspended particles around a coal-fired power station: Particulate  
1521 levels and sources, *Atmos. Environ.*, 32, 11, 1963–1978, 1998.

1522 Querol, X., Alastuey, A., Pey, J., Cusack, M., Pérez, N., Mihalopoulos, N., Theodosi, C.,  
1523 Gerasopoulos, E., Kubilay, N., and Koçak, M.: Variability in regional background aerosols within the  
1524 Mediterranean, *Atmos. Chem. Phys.*, 9, 4575–4591, doi:10.5194/acp-9-4575-2009, 2009a.

1525 Querol, X., Pey, J., Pandolfi, M., Alastuey, A., Cusack, M., Pérez, N., Moreno, T., Viana, N.,  
1526 Mihalopoulos, N., Kallos, G. and Kleanthous, S.: African dust contributions to mean ambient PM10  
1527 mass-levels across the Mediterranean basin, *Atmos. Environ.*, 43, 4266–4277,  
1528 [doi:10.1016/j.atmosenv.2009.06.013](https://doi.org/10.1016/j.atmosenv.2009.06.013), 2009b.

1529 Redemann, J., Vaughan, M. A., Zhang, Q., Shinozuka, Y., Russell, P. B., Livingston, J. M.,  
1530 Kacenelenbogen, M., and Remer, L. A.: The comparison of MODIS-Aqua (C5) and CALIOP (V2 &  
1531 V3) aerosol optical depth, *Atmos. Chem. Phys.*, 12, 3025–3043, doi:10.5194/acp-12-3025-2012, 2012.

1532 Remer, L. A., Tanré, D., Kaufman, Y. J., Ichoku, C., Mattoo, S., Levy, R., Chu, D. A., Holben, B.,  
1533 Dubovik, O., Smirnov, A., Martins, J. V., Li, R.-R., and Ahman, Z.: Validation of MODIS aerosol  
1534 retrieval over ocean, *Geophys. Res. Lett.*, 29, 8008, doi:10.1029/2001GL013204, 2002.

1535 Remer, L. A., Kaufman, Y. J., Tanré, D., Mattoo, S., Chu, D. A., Martins, J. V., Li, R. R., Ichoku, C.,  
1536 Levy, R. C., Kleidman, R. G., Eck, T. F., Vermote, E., and Holben, B. N.: The MODIS aerosol  
1537 algorithm, products and validation, *J. Atmos. Sci.*, 62, 947–973,  
1538 doi: <http://dx.doi.org/10.1175/JAS3385.1>, 2005.

1539 Remer, L. A., Kleidman, R. G., Levy, R. C., Kaufman, Y. J., Tanré, D., Mattoo, S., Martins, J. V.,  
1540 Ichoku, C., Koren, I., Yu, H., and Holben, B. N.: Global aerosol climatology from the MODIS satellite  
1541 sensors, *J. Geophys. Res.*, 113, D14S07, doi:10.1029/2007JD009661, 2008.

1542 Rodríguez, S., Querol, X., Alastuey, A., Kallos, G., Kakaliagou, O.: Saharan dust contributions to  
1543 PM10 and TSP levels in Southern and Eastern Spain, *Atmos. Environ.*, 35, 2433–2447, 2001.

1544 Salvador, P., Alonso-Pérez, S., Pey, J., Artíñano, B., de Bustos, J. J., Alastuey, A., and Querol, X.:  
1545 African dust outbreaks over the western Mediterranean Basin: 11-year characterization of atmospheric  
1546 circulation patterns and dust source areas, *Atmos. Chem. Phys.*, 14, 6759–6775, doi:10.5194/acp-14-  
1547 6759-2014, 2014.

1548 Schepanski, K., Tegen, I., Todd, M. C., Heinold, B., Bönisch, G., Laurent, B., and Macke, A.:  
1549 Meteorological processes forcing Saharan dust emission inferred from MSG-SEVIRI observations of  
1550 subdaily dust source activation and numerical models, *J. Geophys. Res.*, 114, D10201,  
1551 doi:10.1029/2008jd010325, 2009.

1552 Schuster, G. L., Vaughan, M., MacDonnell, D., Su, W., Winker, D., Dubovik, O., Lapyonok, T., and  
1553 Trepte, C.: Comparison of CALIPSO aerosol optical depth retrievals to AERONET measurements, and  
1554 a climatology for the lidar ratio of dust, *Atmos. Chem. Phys.*, 12, 7431–7452, doi:10.5194/acp-12-  
1555 7431-2012, 2012.

1556 Smirnov, A., Holben, B. N., Eck, T. F., Dubovik, O. and Slutsker, I.: Cloud screening and quality  
1557 control algorithms for the AERONET database, *Remote Sens. Environ.*, 73, 337–349, 2000.

1558 Solmon, F., Mallet, M., Elguindi, N., Giorgi, F., Zakey, A. and Konaré, A.: Dust aerosol impact on  
1559 regional precipitation over western Africa, mechanisms and sensitivity to absorption properties,  
1560 *Geophys. Res. Lett.*, 35, L24705, doi:10.1029/2008GL035900, 2008.

1561 Stephens, G. L., Vane, D. G., Boain, R. J., Mace, G. G., Sassen, K., Wang, Z., Illingworth, A. J.,  
1562 O’Conner, E. J., Rossow, W. G., Durden, S. L., Miller, S. D., Austin, R. T., Benedetti, A., and  
1563 Mitrescu, C.: The CloudSat mission and the A-Train, *Bull. Amer. Meteorol. Soc.*, 83, 1771–1790,  
1564 2002.

1565 Tafuro, A.M., Barnaba, F., De Tomassi, F., Perrone, M.R., Gobbi, G.P.: Saharan dust particle  
1566 properties over the Central Mediterranean, *Atmos. Res.*, 81, 67-93,  
1567 [doi:10.1016/j.atmosres.2005.11.008](https://doi.org/10.1016/j.atmosres.2005.11.008), 2006.

1568 Tanré, D., Kaufman, Y. J., Herman, M., and Mattoo, S.: Remote sensing of aerosol properties over  
1569 oceans using the MODIS/EOS spectral radiances, *J. Geophys. Res.*, 102, 16971–16988, 1997.

1570 Tegen, I.: Modelling the mineral dust aerosol cycle in the climate system, *Quat. Sci. Rev.*, 22, 1821–  
1571 1834, 2003.

1572 Toledano, C., Cachorro, V. E., de Frutos, A. M. Sorribas, M., Prats, N., and de la Morena, B. A.:  
1573 Inventory of African desert dust events over the southwestern Iberian Peninsula in 2000–2005 with an  
1574 AERONET Cimel Sun Photometer, *J. Geophys. Res.*, 112, D21201, doi:10.1029/2006JD008307,  
1575 2007a.

1576

1577 Toledano, C., Cachorro, V.E., Sorribas, M., Berjón, A., de la Morena, B.A., de Frutos, A.M. and  
1578 Gouloub, P.: Aerosol optical depth and Ångström exponent climatology at El Arenosillo AERONET  
1579 site (Huelva, Spain), *Q. J. R. Meteorol. Soc.*, 133, 795–807, doi:10.1002/qj.54, 2007b.

1580

1581 Torres, O., Bhartia, P.K., Herman, J.R., Ahmad, Z. and Gleason, J.: Derivation of aerosol properties  
1582 from a satellite measurements of backscattered ultraviolet radiation: Theoretical basis, *J. Geophys.*  
1583 *Res.*, 103, 17099–17110, 1998.

1584

1585 Torres, O., Bhartia, P. K., Herman, J. R., Sinyuk A., Holben, B.: A long term record of aerosol optical  
1586 thickness from TOMS observations and comparison to AERONET measurements, *J. Atmos. Sci.*,  
1587 59398-413, 2002.

1588

1589 Torres, O., Bhartia, P.K., Sinyuk, A., Welton, E.J., and Holben, D.: Total Ozone Mapping  
1590 Spectrometer measurements of aerosol absorption from space: Comparison to SAFARI 2000 ground-  
1591 based observations, *J. Geophys. Res.*, 110, D10S18, doi:10.1029/2004JD004611, 2005.

1592

1593 Torres, O., A. Tanskanen, B. Veihelman, C. Ahn, R. Braak, P. K. Bhartia, P. Veefkind, and P. Levelt,  
1594 Aerosols and Surface UV Products from OMI Observations: An Overview, *J. Geophys. Res.*, 112,  
1595 D24S47, doi:10.1029/2007JD008809, 2007.

1596

1597 Trigo, I. F., Bigg, G. R., and Davies, T. D.: Climatology of cyclogenesis in the Mediterranean. *Mon.*  
1598 *Weather Rev.*, 130, 549–569, 2002.

1599 Tsamalis, C., Chédin, A., Pelon, J., and Capelle, V.: The seasonal vertical distribution of the Saharan  
1600 Air Layer and its modulation by the wind, *Atmos. Chem. Phys.*, 13, 11235-11257, doi:10.5194/acp-13-  
1601 11235-2013, 2013.

1602 Varga, G., Újvári, G., Kovács, J.: Spatiotemporal patterns of Saharan dust outbreaks in the  
1603 Mediterranean Basin, *Aeolian Res.*, Vol. 15, 151-160, doi:10.1016/j.aeolia.2014.06.005, 2014.

1604 Vaughan, M. A., Powell, K. A., Kuehn, R. E., Young, S. A., Winker, D. M., Hostetler, C. A., Hunt, W.  
1605 H., Liu, Z. Y., McGill, M. J., and Getzewich, B. J.: Fully automated detection of cloud and aerosol  
1606 layers in the CALIPSO lidar measurements, *J. Atmos. Ocean. Tech.*, 26, 2034–2050,  
1607 doi:10.1175/2009jtecha1228.1, 2009.

1608 Winker, D., Vaughan, M., Omar, A., Hu, Y., Powell, K., Liu, Z., Hunt, W., and Young, S.: Overview  
1609 of the CALIPSO mission and CALIOP data processing algorithm, *J. Atmos. Ocean. Tech.*, 26, 2310–  
1610 2323, doi: <http://dx.doi.org/10.1175/2009JTECHA1281.1>, 2009.

1611 Winker, D. M., Tackett, J. L., Getzewich, B. J., Liu, Z., Vaughan, M. A., and Rogers, R. R.: The global  
1612 3-D distribution of tropospheric aerosols as characterized by CALIOP, *Atmos. Chem. Phys.*, 13, 3345-  
1613 3361, doi:10.5194/acp-13-3345-2013, 2013.

1614 Yoon, J., von Hoyningen-Huene, W., Kokhanovsky, A. A., Vountas, M., and Burrows, J. P.: Trend  
1615 analysis of aerosol optical thickness and Ångström exponent derived from the global AERONET  
1616 spectral observations, *Atmos. Meas. Tech.*, 5, 1271-1299, doi:10.5194/amt-5-1271-2012, 2012.

1617 Zhang, J. L., Reid, J. S., and Holben, B. N.: An analysis of potential cloud artifacts in MODIS over  
1618 ocean aerosol optical thickness products, *Geophys. Res. Lett.*, 32, L15803,  
1619 doi:10.1029/2005GL023254, 2005.

1620 Zhang, L., Li, Q. B., Gu, Y., Liou, K. N., and Meland, B.: Dust vertical profile impact on global  
1621 radiative forcing estimation using a coupled chemical-transport–radiative-transfer model, *Atmos.*  
1622 *Chem. Phys.*, 13, 7097-7114, doi:10.5194/acp-13-7097-2013, 2013.

1623

1624

1625

1626

1627

1628

1629

1630

1631

1632

1633

1634

1635

1636

1637

1638

1639

1640

1641

1642

1643 **Table 1:** AERONET stations, depicted with cyan colors in Figure 4, which have been used for the identification of desert  
 1644 dust (DD) episodes based on ground retrievals.

Stations	Latitude	Longitude	Study period
<b>Blida</b>	N 36° 30' 28"	E 02° 52' 51"	7 Nov. 2003 – 18 Feb. 2012
<b>El Arenosillo</b>	N 37° 06' 18"	W 06° 43' 58"	1 Mar. 2000 – 21 Feb. 2010
<b>Evora</b>	N 38° 34' 04"	W 07° 54' 43"	4 Jul. 2003 – 28 Feb. 2013
<b>FORTH CRETE</b>	N 35° 19' 58"	E 25° 16' 55"	23 Jan. 2003 – 6 Aug. 2011
<b>IMC Oristano</b>	N 39° 54' 36"	E 08° 30' 00"	30 May 2000 – 28 Feb. 2003
<b>IMS METU Erdemli</b>	N 36° 33' 54"	E 34° 15' 18"	1 Mar. 2000 – 28 Feb. 2013
<b>Nes Ziona</b>	N 31° 55' 19"	E 34° 47' 20"	1 Feb. 2000 – 28 Feb. 2013

1645

1646 **Table 2:** Percentages of the satellite Ångström exponent, Fine fraction, Effective Radius and Aerosol Index retrievals  
 1647 satisfying the defined thresholds in the satellite algorithm for the identification of desert dust episodes.

Parameter	Valid	Invalid	Number of DD episodes
<b>Ångström exponent</b>	97.8%	2.2%	232
<b>Fine fraction</b>	98.7%	1.3%	232
<b>Effective radius</b>	94.5%	5.5%	117
<b>Aerosol Index</b>	86.9%	13.1%	206

1648

1649

1650

1651

1652

1653

1654

1655

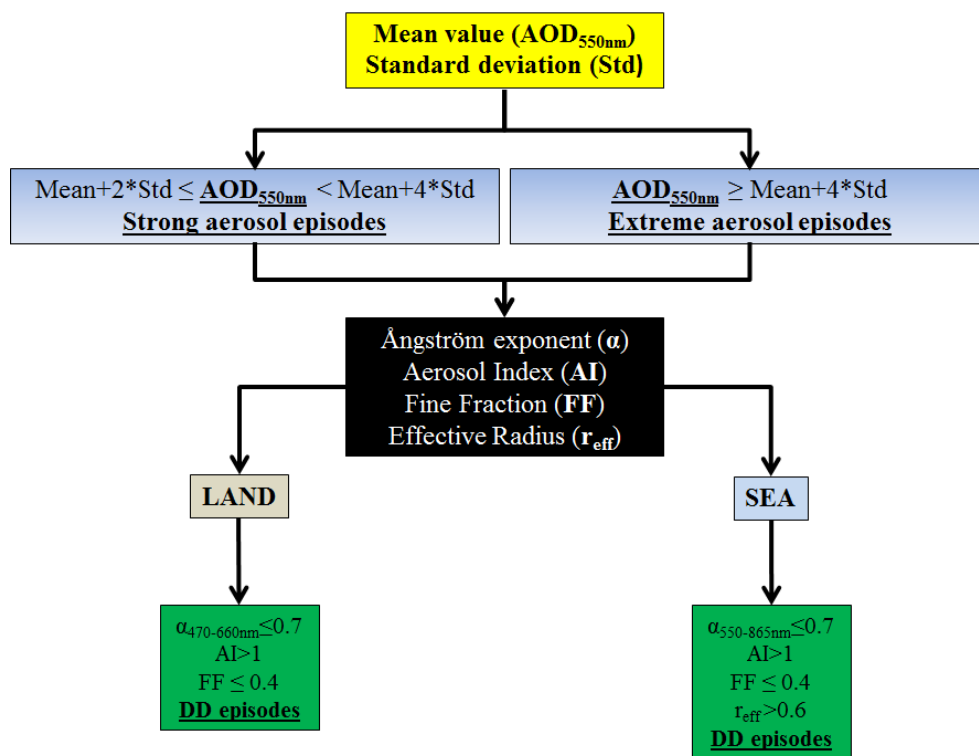
1656

1657

1658

1659

1660



1661

1662 **Figure 1:** Methodology applied to each 1° x 1° grid cell for the identification of the intense Mediterranean desert dust  
 1663 outbreaks.

1664

1665

1666

1667

1668

1669

1670

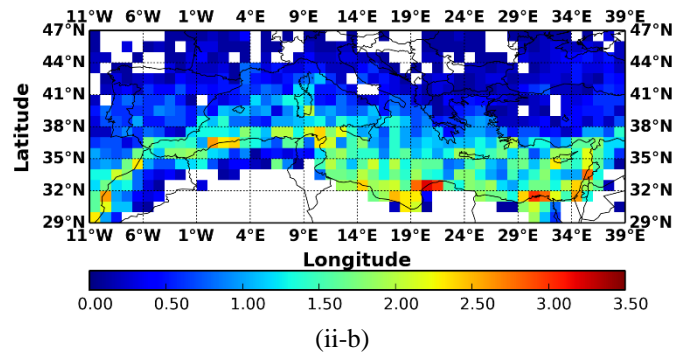
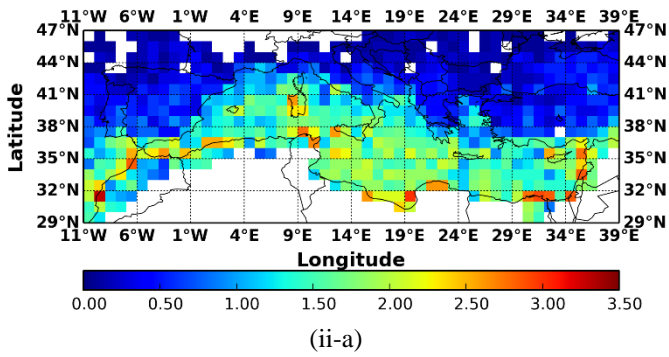
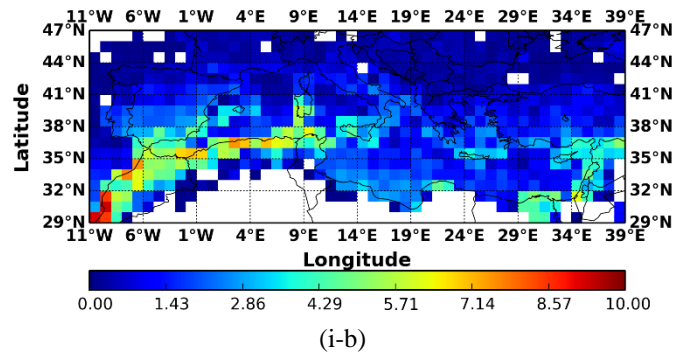
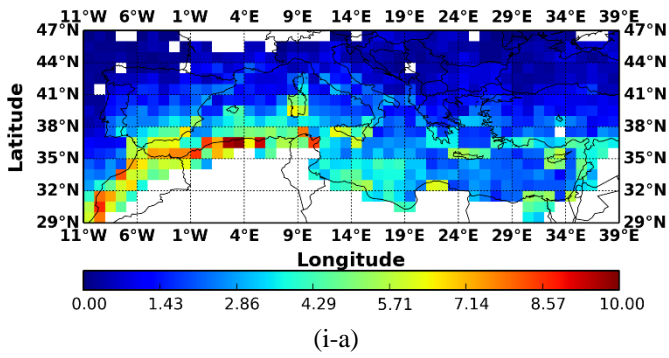
1671

1672

1673

1674

1675



1676 **Figure 2:** Geographical distributions of the occurrence frequency (episodes/year) of: (i) strong and (ii) extreme desert dust  
 1677 episodes, averaged for the periods: (a) Mar. 2000 – Feb. 2013 (MODIS-Terra) and (b) 2003 – 2012 (MODIS-Aqua), over  
 1678 the broader area of the Mediterranean basin.

1679

1680

1681

1682

1683

1684

1685

1686

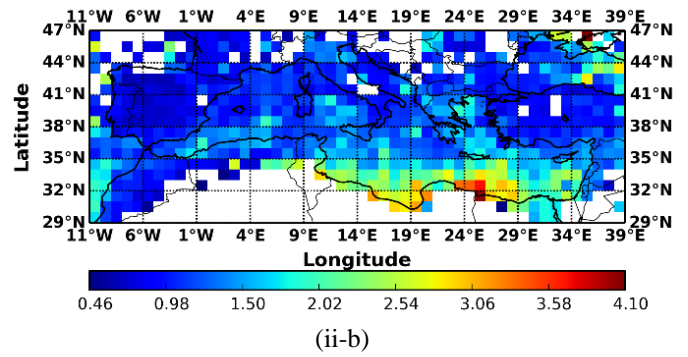
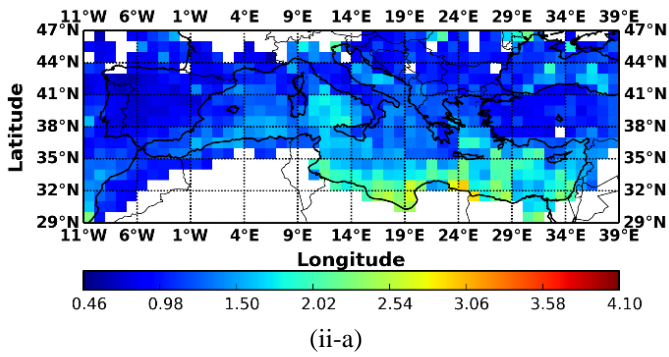
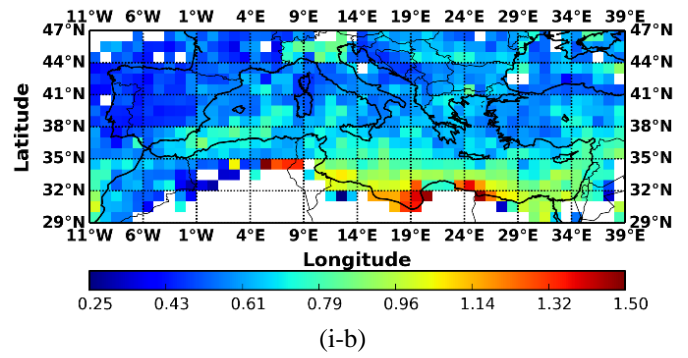
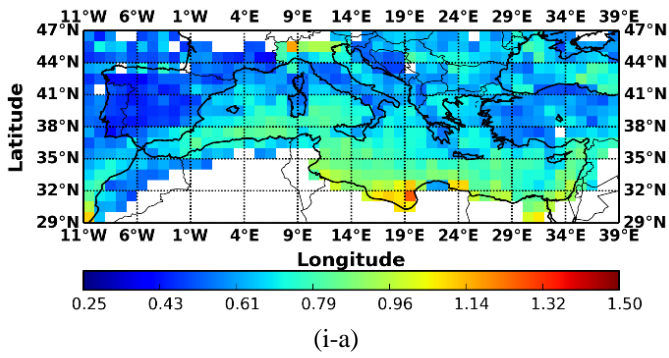
1687

1688

1689

1690

1691



1692 **Figure 3:** Geographical distributions of the intensity (in terms of  $AOD_{550nm}$ ) of: (i) strong and (ii) extreme desert dust  
 1693 episodes, averaged for the periods: (a) 2000 – 2013 and (b) 2003 – 2012, over the broader area of the Mediterranean basin.

1694

1695

1696

1697

1698

1699

1700

1701

1702

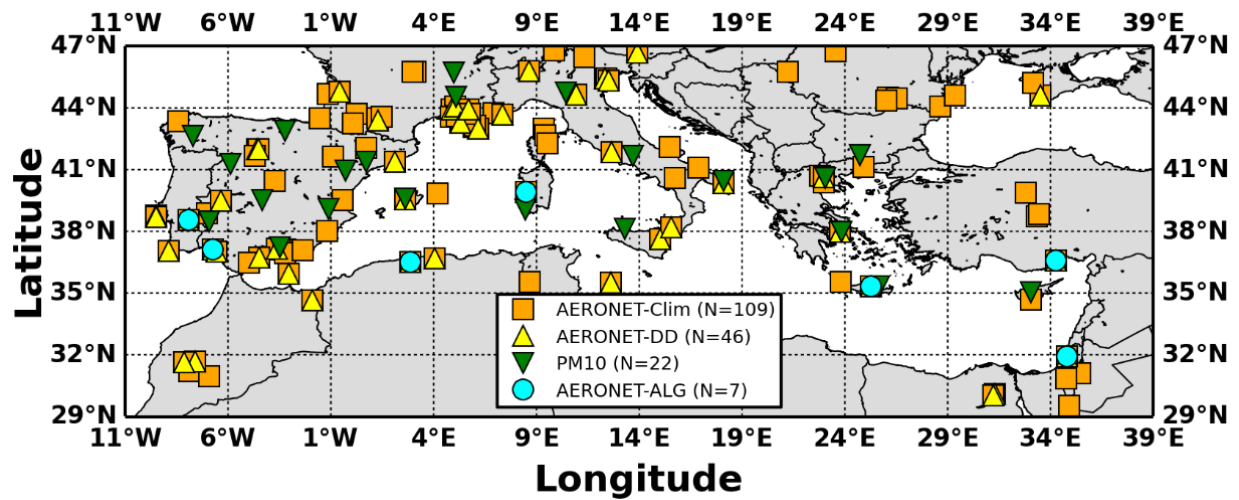
1703

1704

1705

1706

1707



1708

1709 **Figure 4:** Locations of the AERONET and PM<sub>10</sub> stations which have been used for the evaluation of the algorithm's  
 1710 outputs. More specifically, with orange squares are denoted the AERONET stations located into the study region, with the  
 1711 yellow triangles the AERONET stations with coincident satellite and ground retrievals under dust episodes conditions, with  
 1712 the cyan circles the AERONET stations which have been used for the evaluation of the defined algorithm thresholds and  
 1713 with the green triangles are depicted the PM<sub>10</sub> stations.

1714

1715

1716

1717

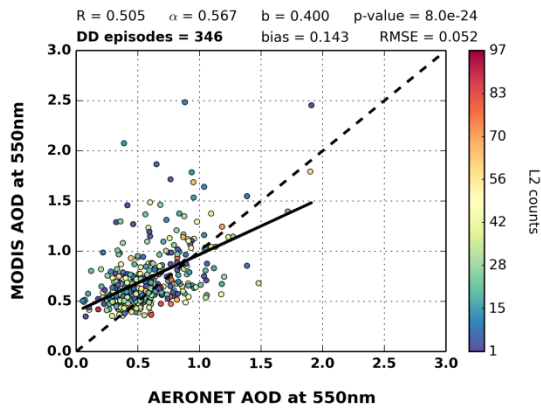
1718

1719

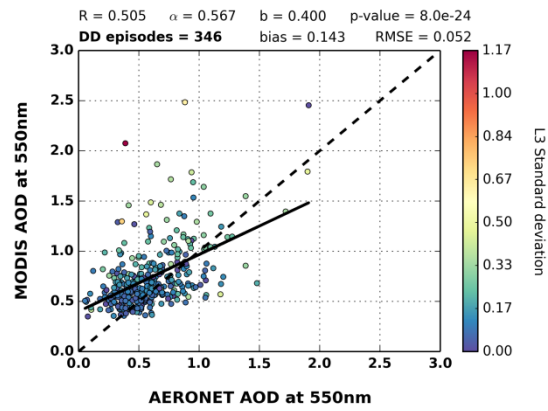
1720

1721

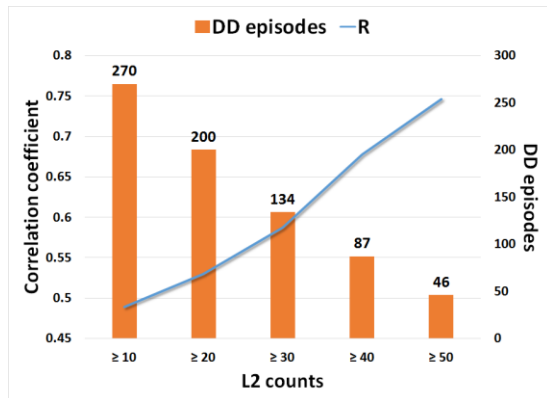
1722



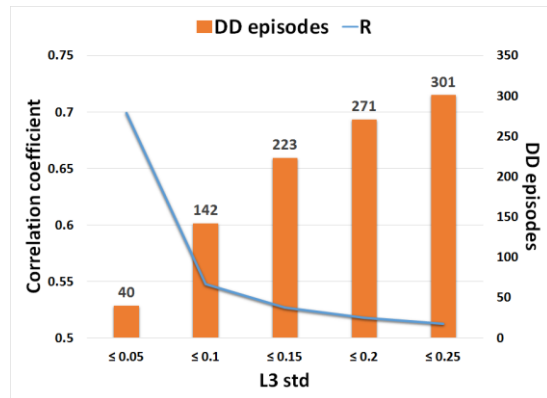
(i-a)



(i-b)



(ii-a)



(ii-b)

1723 **Figure 5:** (i) Scatterplots between MODIS-Terra and AERONET aerosol optical depths at 550 nm under intense desert dust  
 1724 episodes conditions related to the: (a) number of level 2 counts which are used for the calculation of the level 3 retrievals  
 1725 and (b) spatial standard deviation inside the 1° x 1° grid cells (level 3 retrievals). (ii) Sensitivity analysis for the calculated  
 1726 correlation coefficients between satellite and ground AODs, depending on the: (a) number of level 2 retrievals and (b) sub-  
 1727 grid standard deviation of level 3 retrievals.

1728

1729

1730

1731

1732

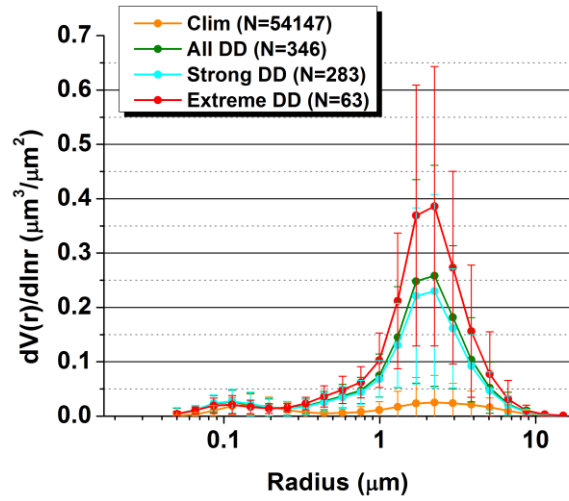
1733

1734

1735

1736

1737



1738

1739 **Figure 6:** AERONET size distributions averaged for all available retrievals (orange curve) as well as for the total (green  
 1740 curve), strong (cyan curve) and extreme (red curve) desert dust episodes, occurred over the broader area of the  
 1741 Mediterranean basin, during the period Mar. 2000 – Feb. 2013. The error bars represent the calculated standard deviation.

1742

1743

1744

1745

1746

1747

1748

1749

1750

1751

1752

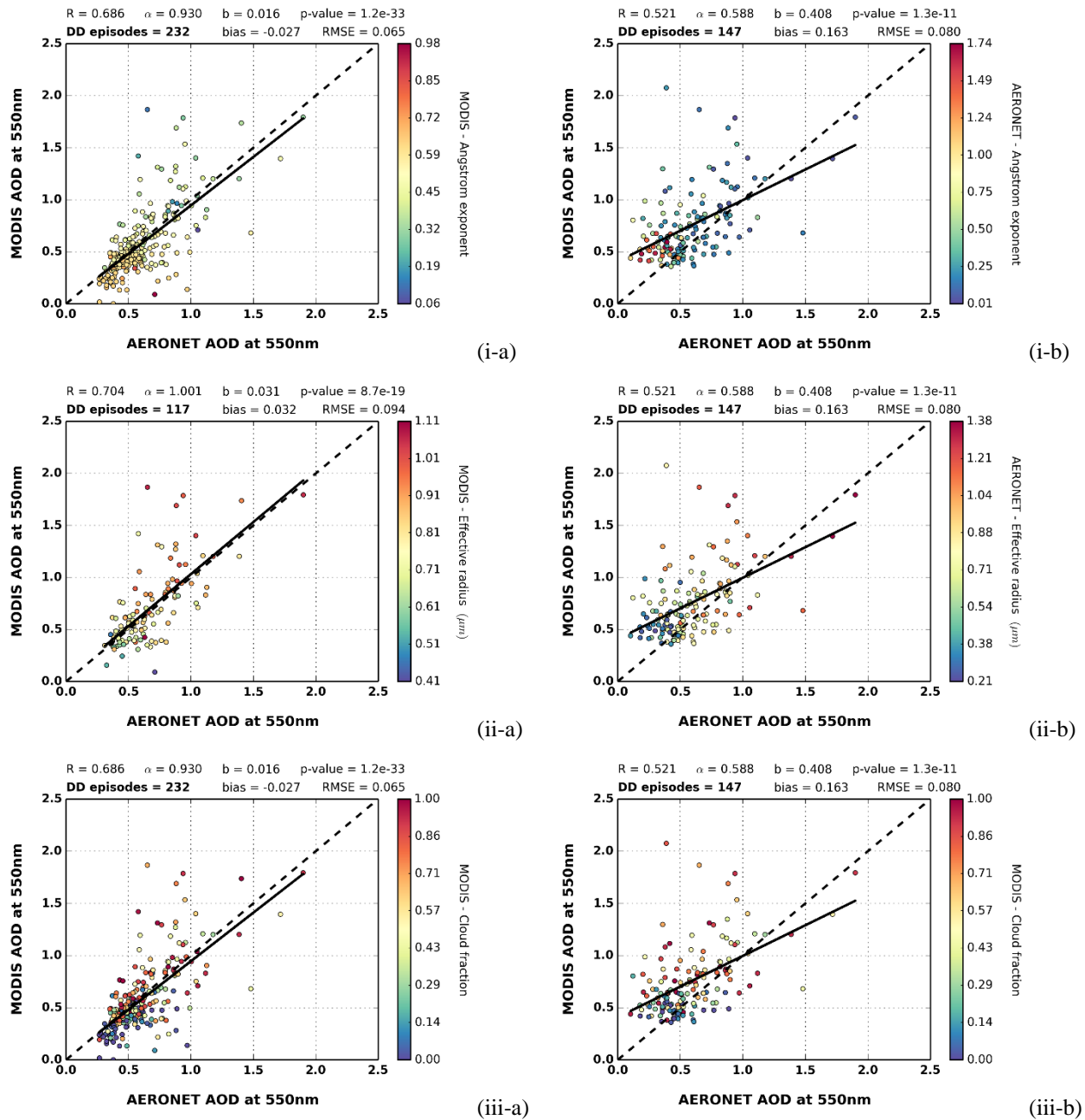
1753

1754

1755

1756

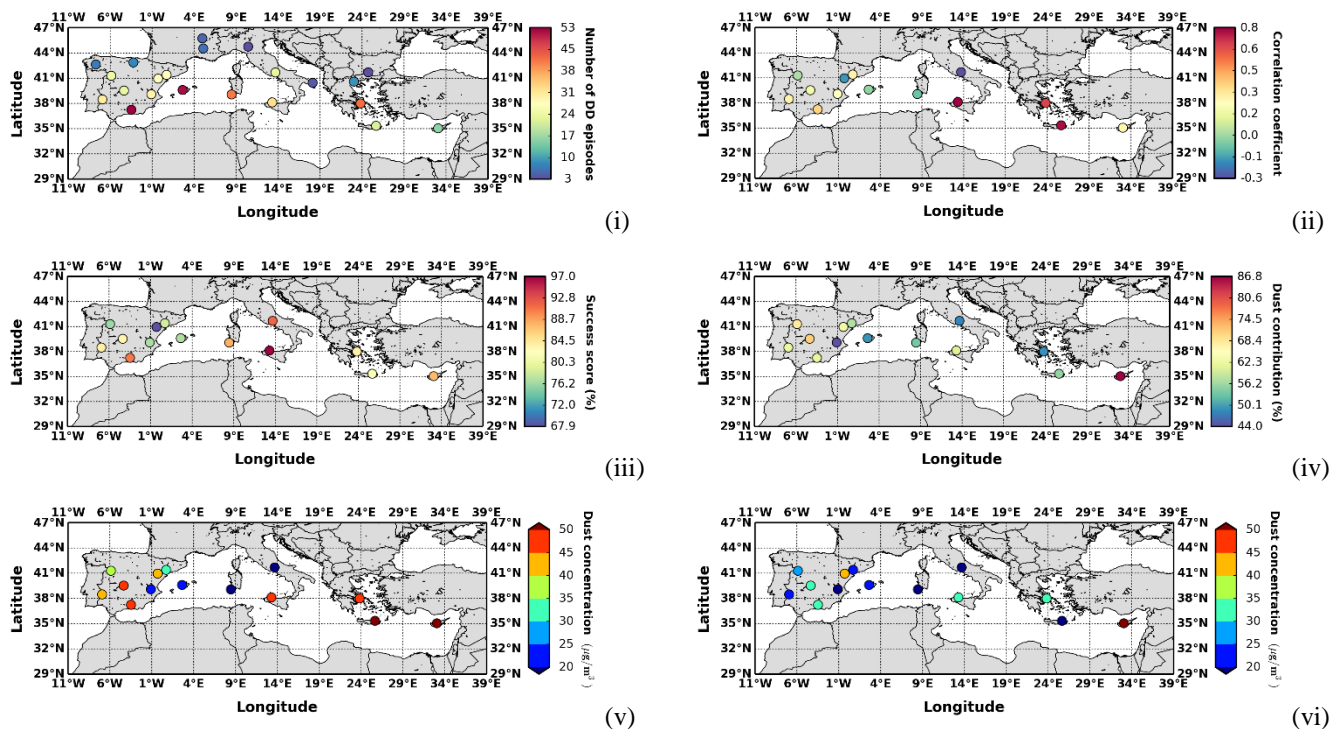
1757



1758 **Figure 7:** Scatterplots of MODIS-Terra and AERONET aerosol optical depths at 550 nm when intense dust episodes have  
 1759 been identified based on: (a) AERONET retrievals and (b) satellite algorithm, respectively. In the left column, colormaps  
 1760 indicate the corresponding values of: (i) Ångström exponent, (ii) Effective radius and (iii) Day cloud fraction derived by  
 1761 MODIS-Terra retrievals. In the right column, colormaps indicate the corresponding values of: (i) AERONET Ångström  
 1762 exponent, (ii) AERONET Effective radius and (iii) MODIS day cloud fraction retrievals. For each scatterplot, are provided  
 1763 the correlation coefficient ( $R$ ), slope ( $\alpha$ ), intercept ( $b$ ), p-value, number of DD episodes, bias and root mean square error  
 1764 ( $RMSE$ ).

1765

1766



1767 **Figure 8:** (i) Number of concurrent intense DD episodes where total PM<sub>10</sub> concentrations and MODIS-Terra AOD retrievals  
 1768 are available, (ii) Computed correlation coefficient values between total PM<sub>10</sub> concentrations and MODIS-Terra AOD  
 1769 retrievals in stations where at least 10 DD episodes have been recorded, (iii) Percentage of intense DD episodes where dust  
 1770 particles have been identified by the ground stations, (iv) Dust contribution percentages (%) to the total PM<sub>10</sub>  
 1771 concentrations, (v) Calculated mean and (vi) median dust concentrations (µg m<sup>-3</sup>), based on ground measurements for the  
 1772 identified intense DD episodes by the satellite algorithm.

1773

1774

1775

1776

1777

1778

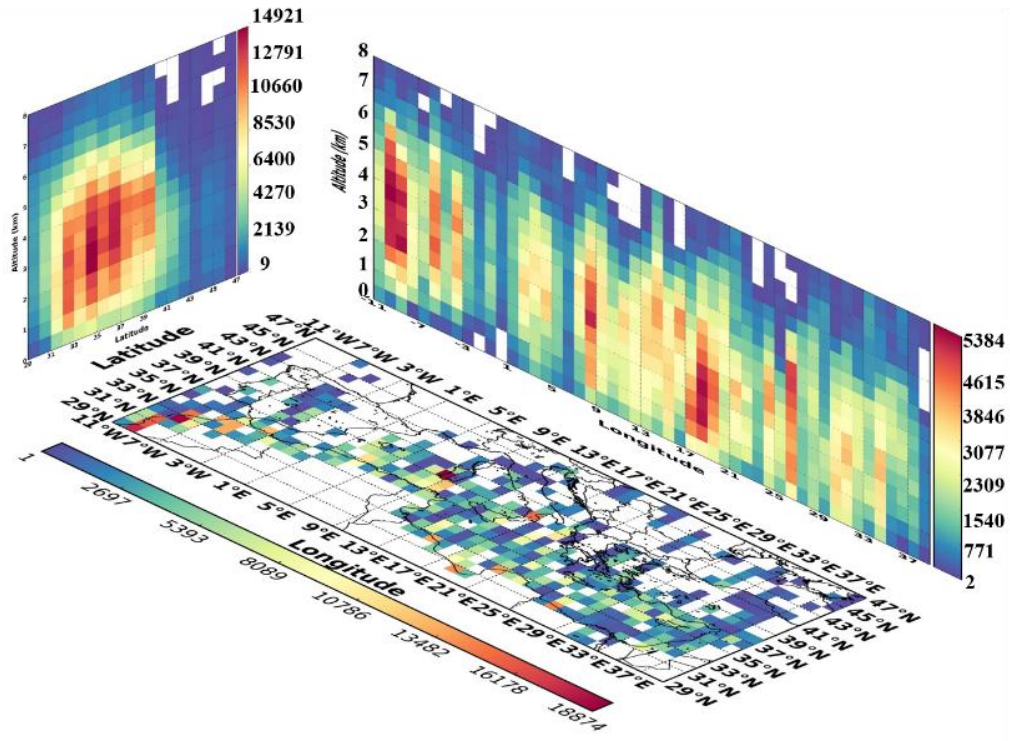
1779

1780

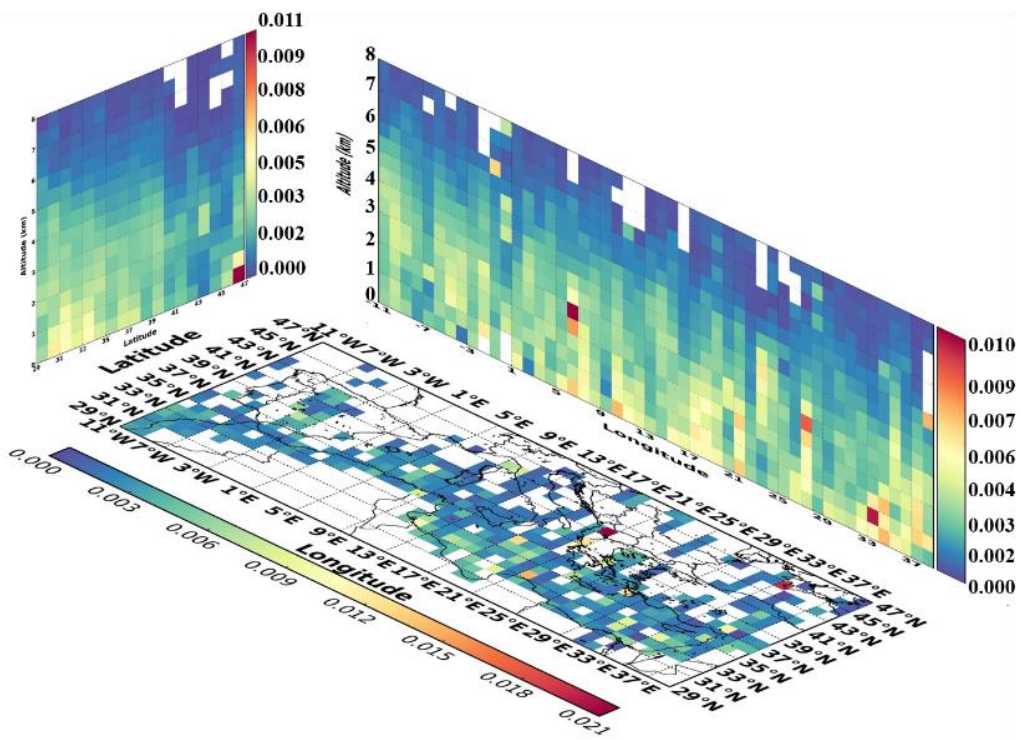
1781

1782

1783

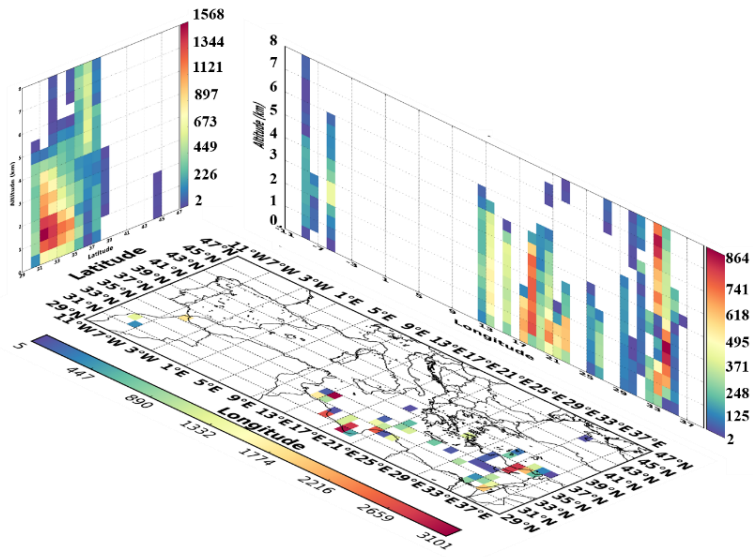


(i)

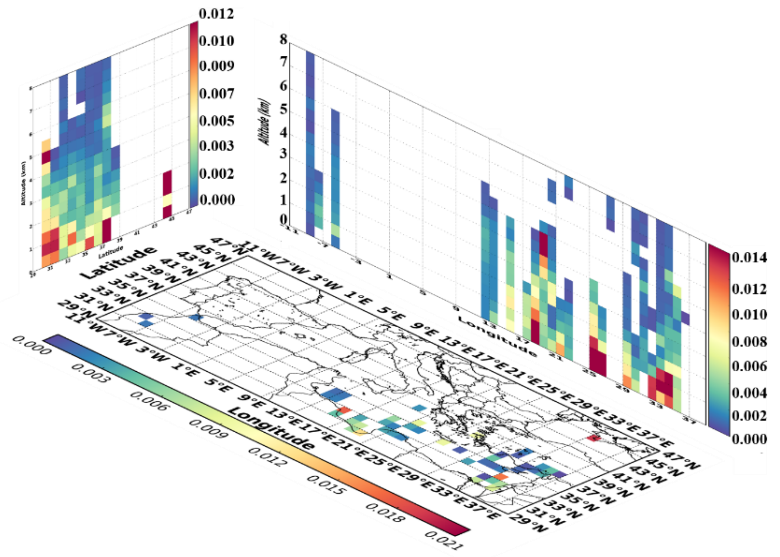


(ii)

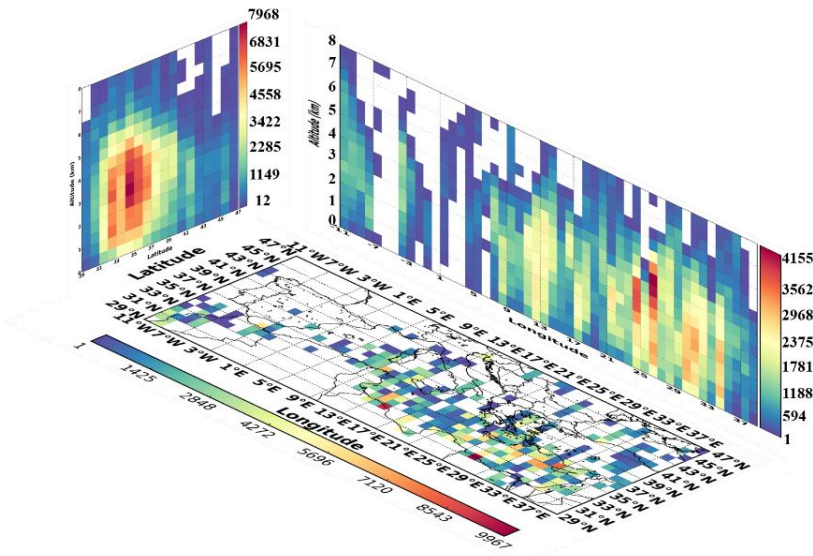
1784 **Figure 9:** Three dimensional structure of the: (i) overall number of dust and polluted dust observations and (ii) total  
 1785 backscatter coefficient at 532 nm (in  $\text{km}^{-1} \text{sr}^{-1}$ ), over the broader Mediterranean basin under DD episodes conditions, based  
 1786 on CALIOP-CALIPSO vertical resolved retrievals for the period Jun. 2006 – Feb. 2013.



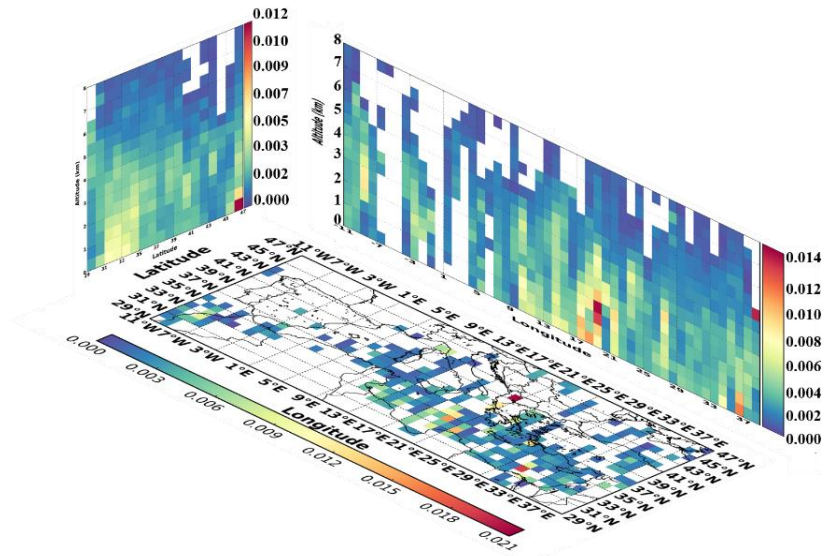
(i-a)



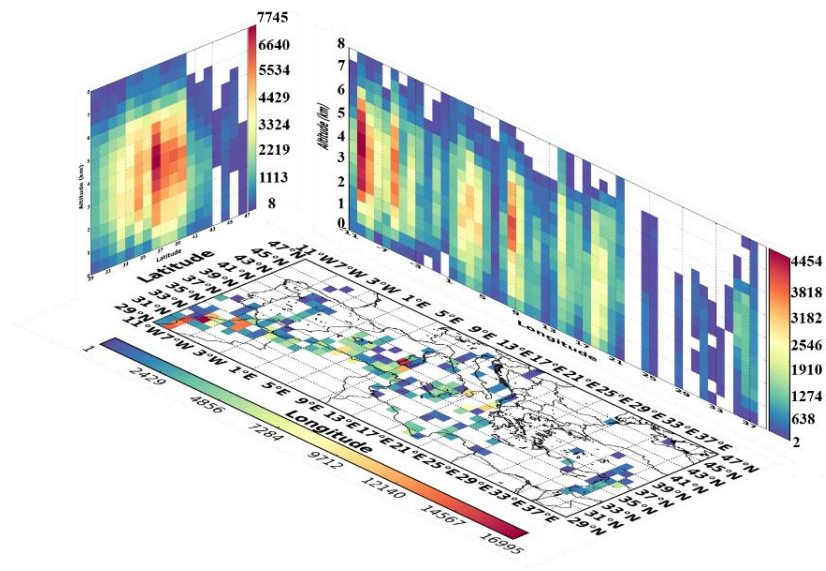
(i-b)



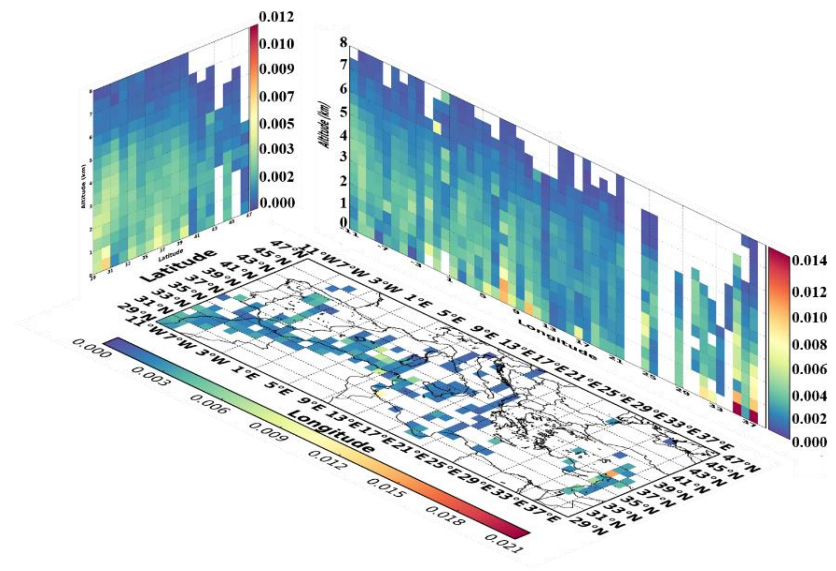
(ii-a)



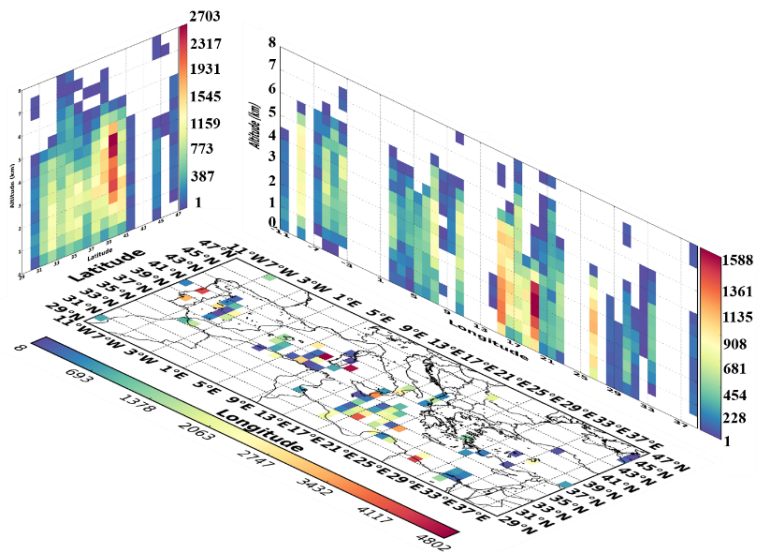
(ii-b)



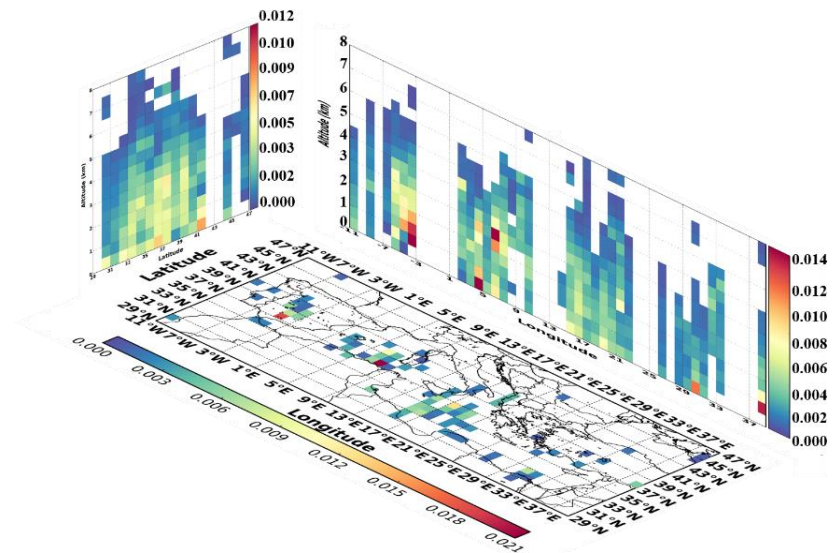
(iii-a)



(iii-b)

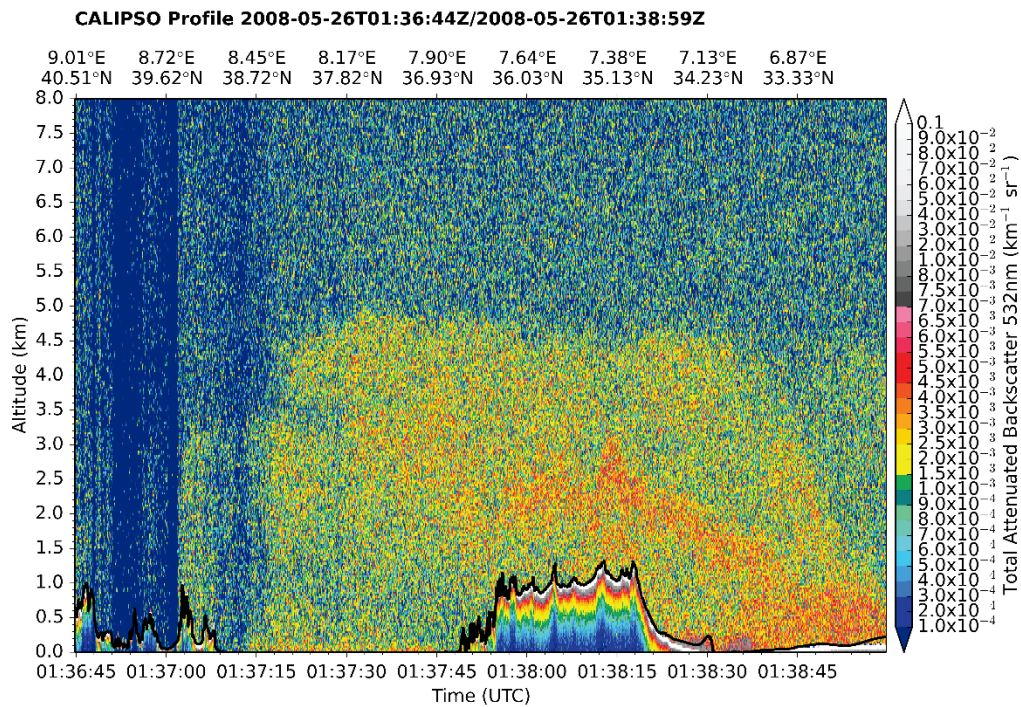


(iv-a)



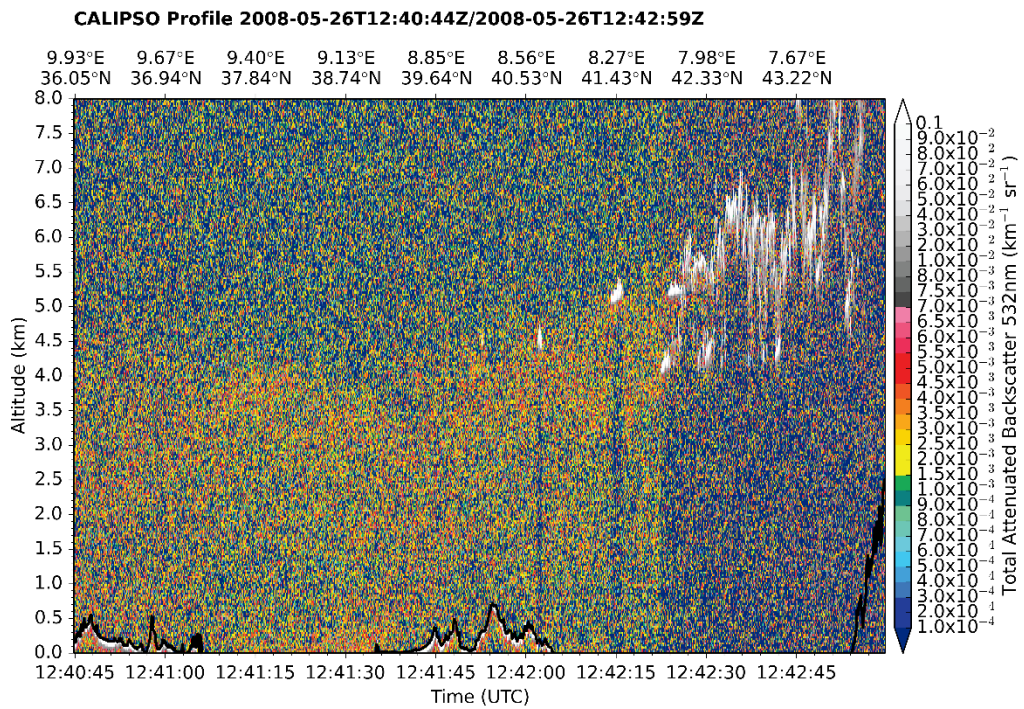
(iv-b)

**Figure 10:** Three dimensional representation of the: (a) overall number of dust and polluted dust observations and (b) total backscatter coefficient at 532 nm (in  $\text{km}^{-1} \text{sr}^{-1}$ ), over the broader Mediterranean basin, under DD episodes conditions, for: (i) winter, (ii) spring, (iii) summer and (iv) autumn based on CALIOP-CALIPSO vertical resolved retrievals, over the period Jun. 2006 – Feb. 2013.



1790

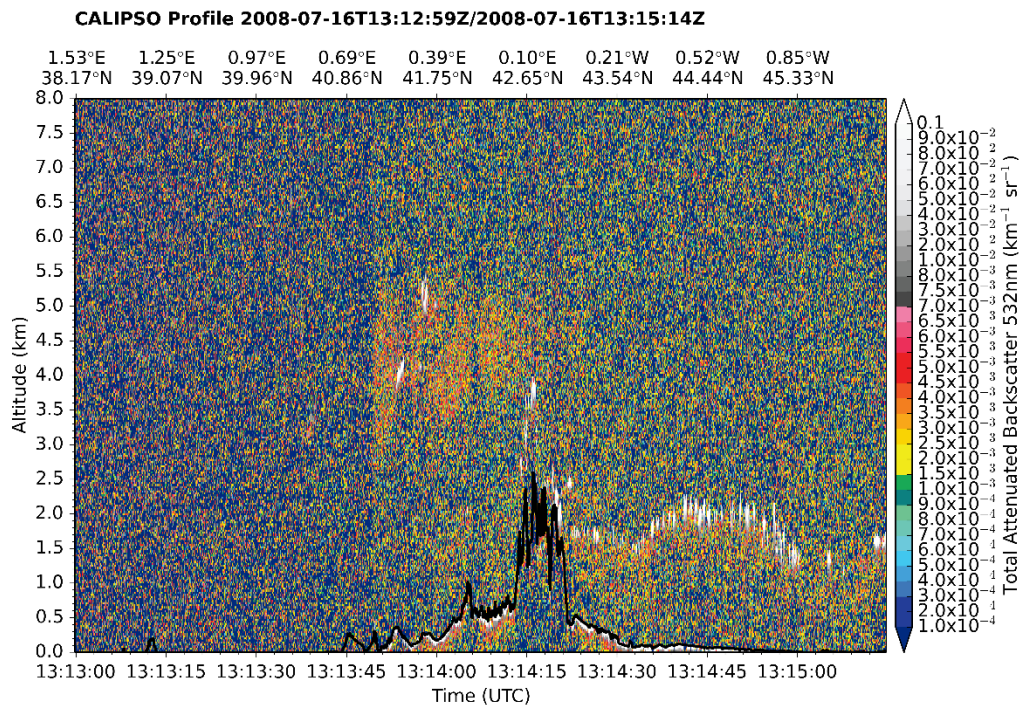
(i)



1791

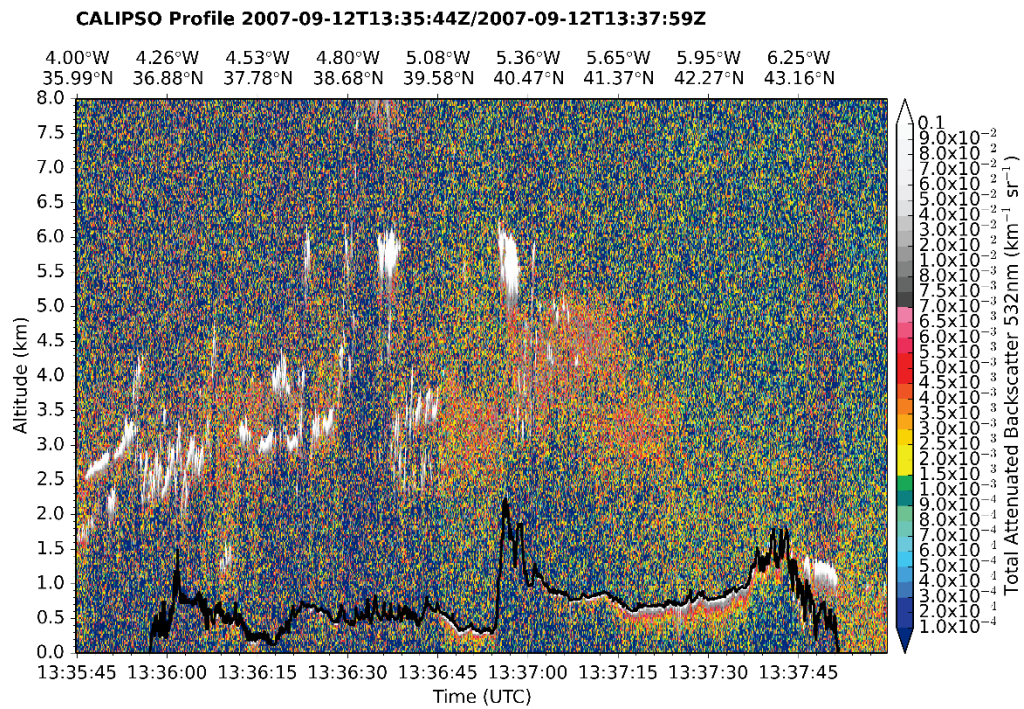
(ii)

1792 **Figure 11:** Cross sections of the total backscatter coefficient at 532 nm (in  $\text{km}^{-1} \text{sr}^{-1}$ ) vertical profiles along the CALIOP-  
 1793 CALIPSO track during: (i) nighttime and (ii) daytime, on 26<sup>th</sup> May 2008, over the station Censt (Lat: 39.064, Lon: 8.457).  
 1794 The black thick solid line represents the surface elevation.



1795

(i)



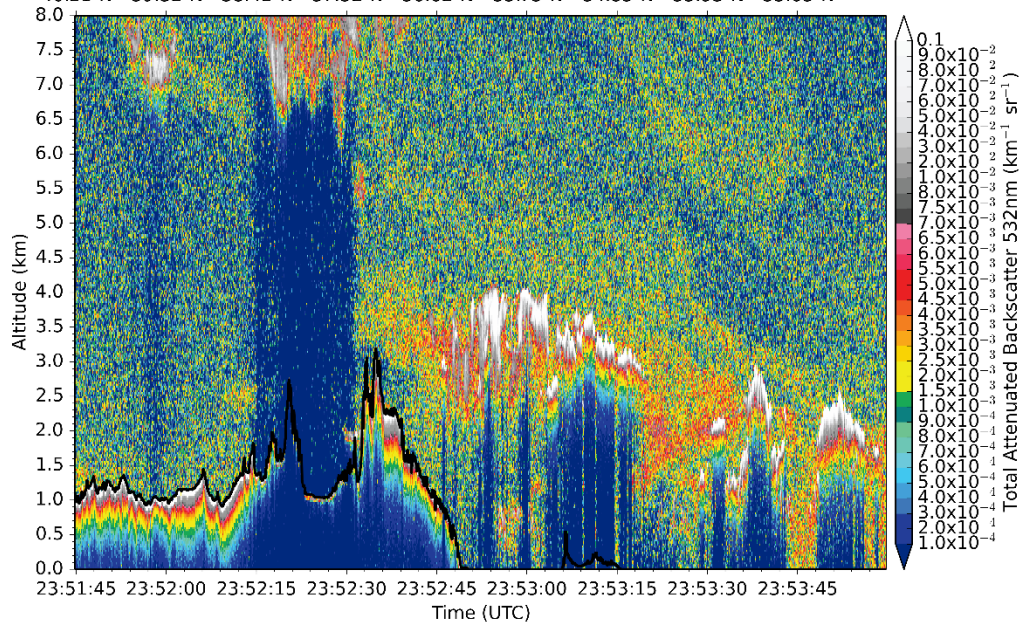
1796

(ii)

1797 **Figure 12:** Cross sections of the total backscatter coefficient at 532 nm (in  $\text{km}^{-1} \text{sr}^{-1}$ ) vertical profiles along the CALIOP-  
 1798 CALIPSO track during daytime over the stations: (i) Els Torms (Lat: 41.395, Lon: 0.721) on 16<sup>th</sup> July 2008 and (ii) San  
 1799 Pablo (Lat: 39.525, Lon: -4.353) on 12<sup>th</sup> September 2007. The black thick solid line represents the surface elevation.

**CALIPSO Profile 2007-02-25T23:51:44Z/2007-02-25T23:53:59Z**

35.14°E 34.86°E 34.58°E 34.31°E 34.04°E 33.78°E 33.52°E 33.27°E 33.02°E  
40.21°N 39.32°N 38.42°N 37.52°N 36.62°N 35.73°N 34.83°N 33.93°N 33.03°N



1800

1801 **Figure 13:** Cross section of the total backscatter coefficient at 532 nm (in  $\text{km}^{-1} \text{sr}^{-1}$ ) vertical profiles along the CALIOP-  
1802 CALIPSO track during daytime over the station Agia Marina (Lat: 35.039, Lon: 33.058) on 25<sup>th</sup> February 2007. The black  
1803 thick solid line represents the surface elevation.

1804

1805

1806

1807

1808

1809

1810

1811